EFFECT OF LOADING RATE ON FRACTURE OF NITI

by

Fatma Mutlu

B.S., Mechanical Engineering, Fırat University, 2009

Submitted to the Institute for Graduate Studies in
Science and Engineering in partial fulfillment of
the requirements for the degree of
Master of Science

Graduate Program in Mechanical Engineering
Boğaziçi University

2016

EFFECT OF LOADING RATE ON FRACTURE OF NITI

APPROVED BY:

Prof. Günay Anlaş (Thesis Supervisor)	.....
Assoc. Prof. C. Can Aydıner	.....
Assist. Prof. Alpay Oral	.....

DATE OF APPROVAL: 18.08.2016

ACKNOWLEDGEMENTS

I would like to express my sincere gratitude to my thesis supervisor, Professor Günay Anlaş for his support, guidance, advice and encouragement during this study. It has been an honor and a pleasure to work with him. I would like to thank Assoc. Prof. C. Can Aydıner for his helpful comments and discussions and Assist. Prof. Alpay Oral for his interest and review of the thesis.

I would like to thank my friends Buse, Gülcan, Onur, Fatih, Nima, Selçuk, Behrouz and Beyza for their assistance and helpful discussions on my thesis.

Finally, I want to thank my family for their love, support and encouragement throughout my study life.

ABSTRACT

EFFECT OF LOADING RATE ON FRACTURE OF NITI

This thesis studies the effect of loading rate on fracture behavior of Shape Memory Alloy (SMA) NiTi. First, Differential Scanning Calorimetry (DSC) are used to obtain the phase transformation temperatures of NiTi. Then series of tensile tests are performed for determining the mechanical properties under different loading rates. Next, fracture tests under increasing loading rates are conducted using pre-cracked, Mode-I Compact Tension (CT) specimens and critical stress intensity factors are calculated using the empirical equations proposed by ASTM E399 assuming that Linear Elastic Fracture Mechanics (LEFM) is applicable. Then, displacement field obtained with the Digital Image Correlation (DIC) technique is used for stress intensity factor (SIF) calculations. Phase transformation region extension along the crack is estimated with DIC measurements and is compared to the analytical calculations. Analytical calculations for phase transformation region size are carried out using SIFs obtained from DIC and from the empirical equations of ASTM E399. Finally, using material properties obtained from tensile tests and the results of fracture tests, Finite Elements (FE) models are built to calculate the phase transformation regions. Using the J contour integrals, stress intensity factors are estimated using LEFM relations. Using the displacement field obtained from the FE models, SIF values are calculated and the Crack Mouth Opening Displacement (CMOD) values are obtained from the FE models.

ÖZET

NiTi ŞEKİL HAFIZALI ALAŞIMIN KIRILMA DAVRANIŞI ÜZERİNE YÜKLEME HIZININ ETKİSİ

Bu tezde NiTi şekil hafızalı alaşımın kırılma davranışı üzerine yükleme hızının etkisi çalışılır. İlk olarak, faz değişim sıcaklıklarının elde edilmesi için diferansiyel taramalı kalorimetri (DSC) deneyleri yapılmıştır. Sonra, NiTi şekil hafızalı alaşımın malzeme özelliklerinin belirlenmesi için farklı yükleme hızlarında çekme testleri yapılmıştır. Daha sonra, ön-çatlak açılmış mod I yükleme altındaki kompakt gerilim numuneleri kullanılarak farklı hızlarda kırılma deneyleri yapılmış ve lineer elastik kırılma mekaniği (LEFM) şartları kabulü ile ASTM E399 standartında önerilen deneysel elde edilmiş denklemler kullanılarak kritik gerilme şiddeti faktörleri (SIF) hesaplanmıştır. Dijital görüntü korelasyonu (DIC) ile elde edilen yerdeğişim verisi gerilme şiddeti faktörleri (SIF) hesaplanmasında kullanılmıştır. Çatlak düzlemindeki faz dönüşüm bölgesi büyüklüğü dijital görüntü korelasyonu verileri kullanılarak ölçülmüş ve analitik hesaplama sonuçları ile karşılaştırılmıştır. Faz dönüşüm bölgesi büyüklüğü analitik hesaplamaları, dijital görüntü korelasyonu (DIC) ve ASTM E399 deneysel denklemleri ile hesaplanan gerilme şiddeti faktörleri kullanılarak her ikisi için de yapılmıştır. Son olarak, çekme deneylerinden elde edilen malzeme özellikleri ve kırılma deneyi sonuçları kullanılarak sonlu elemanlar (FE) modelleri faz dönüşüm bölgesi büyüklüğü hesaplamasında kullanılmış ve lineer elastik kırılma mekaniği (LEFM) şartları kabulü yapılarak sonlu elemanlar (FE) modelinden elde edilen J-integrali değerleri ile gerilme şiddeti faktörleri hesaplanmıştır. Sonlu elemanlar modellerinden elde edilen yerdeğişim verisi kullanılarak gerilme şiddeti faktörleri hesaplanmış ve sonlu elemanlar modellerinden çatlak ağzı açılım kayması (CMOD) değerleri elde edilmiştir.

TABLE OF CONTENTS

ACKNOWLEDGEMENTS . . . iii
ABSTRACT . . . iv
ÖZET . . . v
LIST OF FIGURES . . . viii
LIST OF TABLES . . . xiii
LIST OF SYMBOLS . . . xvi
LIST OF ACRONYMS/ABBREVIATIONS . . . xviii
1. INTRODUCTION . . . 1
1.1. Shape Memory Alloys . . . 1
1.1.1. Superelasticity and Shape Memory Effect . . . 1
1.2. Works on Fracture of SMAs . . . 3
1.3. Effect of Loading Rate . . . 7
1.4. Objectives . . . 16
2. MATERIAL CHARACTERIZATION . . . 18
2.1. Differential Scanning Calorimetry (DSC) . . . 19
2.2. Tensile Tests . . . 22
2.2.1. Tensile Test Set-up . . . 24
2.2.2. Tensile Test Results at Room Temperature . . . 25
2.2.2.1. Transformation Stresses . . . 27
2.2.3. Tensile Tests at Ambient Temperature Lower Than A_f . . . 28
2.3. Temperature Effect on Transformation Stresses . . . 32
3. EVALUATION OF FRACTURE PARAMETERS . . . 38
3.1. Introduction . . . 38
3.2. The Effect of Loading Rate on Fracture Parameters . . . 41
3.3. Implementation of DIC Method to Fracture Experiments . . . 41
3.4. Fracture Experiments . . . 42
3.4.1. Fracture Test Setup . . . 42
3.4.2. Fracture Test Procedure . . . 43
3.4.3. Digital Image Correlation (DIC) . . . 47

3.4.4. DIC Results 49
3.5. Calculation of Critical Stress Intensity Factor (K_Q) Using ASTM E399 57
4. EVALUATION OF TRANSFORMATION REGION AROUND CRACK TIP 59
4.1. Introduction 59
4.2. Evaluation of Transformation Region 61
4.2.1. Transformation Strains 61
4.2.2. Estimation of Transformation Zone Using DIC 62
4.3. Analytical Calculation of Transformation Zone 63
5. COMPUTATIONAL EVALUATION OF TRANSFORMATION REGION AND FRACTURE PARAMETERS 69
5.1. Problem Statement 69
5.2. Computational Tensile Tests 71
5.3. Computational Fracture Tests 73
5.4. Computational Evaluation of Fracture Parameters 77
6. SUMMARY AND CONCLUSIONS 84
REFERENCES 88

LIST OF FIGURES

Figure 1.1. (a) Superelastic Stress - Strain Diagram (b) Superelastic Loading Path on Stress - Temperature Diagram [1]. 2

Figure 1.2. Stress - Strain - Temperature Diagram Illustrating the Shape Memory Effect [1]. 3

Figure 2.1. Dimensions of NiTi Tensile Test Specimen in mm. 18

Figure 2.2. DSC Curve of NiTi [2]. 19

Figure 2.3. Differential Scanning Calorimeter. 20

Figure 2.4. Differential Scanning Calorimetry of the Material. 21

Figure 2.5. Stress-Strain Curve of NiTi Alloy Illustrating the Transformation Stresses, Young's Moduli of Austenite, E_A, and Martensite, E_M [3]. 23

Figure 2.6. Tensile Test Set-up. 24

Figure 2.7. Stress-Strain Diagrams Obtained From Tensile Tests Conducted at Room Temperature of 26 °C For Loading Rates of (a) 0.1 mm/min, (b) 0.5 mm/min, (c) 1 mm/min, (d) 1.5 mm/min, (e) 2 mm/min. 25

Figure 2.8. Stress-Strain Diagrams For Different Loading Rates Obtained From Tensile Tests Conducted at Room Temperature (26 °C). 26

Figure 2.9. Stress-Strain Diagrams Obtained From Tensile Tests Conducted at Ambient Temperature of 20 °C For Loading Rates of (a) 0.1 mm/min, (b) 0.5 mm/min, (c) 1 mm/min, (d) 1.5 mm/min, (e) 2 mm/min. 29

Figure 2.10. Stress-Strain Diagrams For Different Loading Rates Obtained From Tensile Tests Conducted at Ambient Temperature of 20 °C. 30

Figure 2.11. Stress - Strain Curves Obtained From Tensile Tests Conducted at Different Testing Temperatures. 32

Figure 2.12. Stress - Temperature Phase Diagram of NiTi Obtained From Tensile Tests Conducted at Different Testing Temperatures. 34

Figure 2.13. Stress - Temperature Phase Diagram Plotted Using Equations Proposed by Falvo *et al.* [4] and Data of Present Study. 35

Figure 2.14. Stress - Temperature Phase Diagram Plotted Using the Equations Proposed by Tanaka *et al.* [5]. 37

Figure 3.1. The Basic Modes of Loading. [6]. 39

Figure 3.2. Illustration of the Coordinate System at the Crack Tip [6]. 40

Figure 3.3. Fracture Test Set-up. 43

Figure 3.4. Dimensions of NiTi Fracture Test Specimen in mm. 44

Figure 3.5. Compact Tension Specimen Grips With Brass Bushes. 45

Figure 3.6. An Example DIC Pattern. 46

Figure 3.7. Tracking Procedure of a Particular Point Between the Undeformed Image and the Deformed Images [7]. 47

Figure 3.8. An Example Grid Set on Undeformed Image and It's Reflection on The Deformed Image at WinDIC Menu 1.3 Software. 49

Figure 3.9. Principal Types of Force-Displacement (CMOD) Records [8]. . . . 50

Figure 3.10. Load Displacement Graphs From Fracture Tests at Room Temperature of 26 °C For Loading Rates of (a) 0.1 mm/min, (b) 0.5 mm/min, (c) 1.5 mm/min, (d) 2 mm/min. 51

Figure 3.11. Load Displacement Graphs for NiTi From Fracture Tests at Room Temperature of 26 °C For Different Loading Rates. 52

Figure 3.12. Displacement Contour Plot of the data From DIC Technique and Those Calculated Theoretically Using Equation 3.8 With Replacing the Obtained Constants For 0.1 mm/min Loading Rate. 54

Figure 3.13. Displacement Contour Plot of the data From DIC Technique and Those Calculated Theoretically Using Equation 3.8 With Replacing the Obtained Constants For 0.5 mm/min Loading Rate. 55

Figure 3.14. Displacement Contour Plot of the data From DIC Technique and Those Calculated Theoretically Using Equation 3.8 With Replacing the Obtained Constants For 1.5 mm/min Loading Rate. 55

Figure 3.15. Displacement Contour Plot of the data From DIC Technique and Those Calculated Theoretically Using Equation 3.8 With Replacing the Obtained Constants For 2 mm/min Loading Rate. 56

Figure 4.1. Representation of First Order (r_y) and Second Order (r_p) Estimates of Plastic Zone Sizes Proposed by Irwin [6]. 60

Figure 5.1. Geometry of the 2D Finite Element Model. 69

Figure 5.2. Mesh of the 2D Finite Element Model. 70

Figure 5.3. Stress - Strain and Stress - Temperature Graph of NiTiNOL of the Built-in Model [9]. 71

Figure 5.4. Stress-Strain Diagrams Obtained From FEA Using the Material Properties From Tensile Tests Conducted at Room Temperature of 26 °C For Loading Rates of (a) 0.1 mm/min, (b) 0.5 mm/min, (c) 1.5 mm/min, (d) 2 mm/min. 72

Figure 5.5. Stress-Strain Diagrams at Different Loading Rates. 73

Figure 5.6. Martensite Volume Fraction Contours From FE For Loading Rate of 0.1 mm/min. 74

Figure 5.7. Martensite Volume Fraction Contours From FE For Loading Rate of 0.5 mm/min. 74

Figure 5.8. Martensite Volume Fraction Contours From FE For Loading Rate of 1.5 mm/min. 75

Figure 5.9. Martensite Volume Fraction Contours From FE For Loading Rate of 2 mm/min. 75

Figure 5.10. Displacement Contour Plots From ABAQUS and From Equation 3.8 For 0.1 mm/min Loading Rate. 80

Figure 5.11. Displacement Contour Plots From ABAQUS and From Equation 3.8 For 0.5 mm/min Loading Rate. 81

Figure 5.12. Displacement Contour Plots From ABAQUS and From Equation 3.8 For 1.5 mm/min Loading Rate. 81

Figure 5.13. Displacement Contour Plots From ABAQUS and From Equation 3.8 For 2 mm/min Loading Rate. 82

LIST OF TABLES

Table 2.1. Transformation temperatures obtained from DSC curve. 22

Table 2.2. Mechanical properties of NiTi obtained from tensile tests conducted at room temperature of 26 °C for different loading rates 27

Table 2.3. Transformation stresses of NiTi obtained from tensile tests conducted at room temperature of 26 °C for different loading rates . . 28

Table 2.4. Mechanical properties of NiTi obtained from tensile tests conducted at ambient temperature of 20 °C for different loading rates 31

Table 2.5. Transformation stresses of NiTi obtained from tensile tests conducted at ambient temperature of 20 °C for different loading rates 31

Table 2.6. Transformation stresses of NiTi, from tensile tests conducted at different testing temperatures. 33

Table 3.1. Maximum load and extension values obtained from fracture experiments at room temperature of 26 °C. 50

Table 3.2. Fracture parameters calculated with curve fitting of the displacement field obtained from DIC to Equation 3.8 for the tests conducted at room temperature of 26 °C at different loading rates with $r_{min} = 0.06$ and $r_{max} = 0.8$. 53

Table 3.3. Fracture parameters calculated with least squares fitting of the displacement field obtained from DIC to Equation 3.8 for the tests conducted at room temperature of 26 °C at different loading rates after omitting the K_{II} term with $r_{min} = 0.06$ and $r_{max} = 0.8$. . . . 54

Table 3.4. Calculated K_Q results with the dimensions of the specimens conducted at room temperature of 26 °C at different loading rates using Equation 3.9. 58

Table 4.1. Martensite transformation start and finish strains used for transformation zone estimation using the equivalent strain contours obtained from DIC displacement data for loading rates of 0.1 mm/min, 0.5 mm/min, 1.5 mm/min and 2 mm/min. 62

Table 4.2. Measured phase transformation region (PTR) (r_T) using the equivalent strain contours obtained from DIC displacement data for loading rates of 0.1 mm/min, 0.5 mm/min, 1.5 mm/min, 2 mm/min and the K_I values obtained from DIC least-squares fitting to Equation 3.8. 63

Table 4.3. Calculated martensitic region (r_M) for the case $\zeta = 1$ and the phase transformation region (r_T) for the case $\zeta = 0$ using Equation 4.14 for loading rates of 0.1 mm/min, 0.5 mm/min, 1.5 mm/min, 2 mm/min with K_I calculated from ASTM E399 Equation 3.9, when $\theta = 0$. . 67

Table 4.4. Calculated martensitic region (r_M) for the case $\zeta = 1$ and the phase transformation region (r_T) for the case $\zeta = 0$ using Equation 4.14 for loading rates of 0.1 mm/min, 0.5 mm/min, 1.5 mm/min, 2 mm/min, with K_I calculated from DIC data least-squares fitted to Equation 3.8, when $\theta = 0$. 67

Table 5.1. Material properties implemented to the FE ABAQUS models for loading rates of 0.1 mm/min, 0.5 mm/min, 1.5 mm/min, 2 mm/min at room temperature of 26 °C. 71

Table 5.2. Martensitic region r_M and the phase transformation region, r_T for loading rates of 0.1 mm/min, 0.5 mm/min, 1.5 mm/min, 2 mm/min. 76

Table 5.3. J-Integral values obtained from FEA and the calculated K_I using the LEFM relation at Equation 5.1. 77

Table 5.4. Fracture parameters calculated using the displacement field obtained from ABAQUS at different loading rates with $r_{min} = 0.05$ and $r_{max} = 0.295$. 78

Table 5.5. Fracture parameters calculated from displacement data obtained from ABAQUS omitting the K_{II} with $r_{min} = 0.05$ and $r_{max} = 0.295$. 79

Table 5.6. Comparison of K_Is. 80

Table 5.7. Crack Mouth Opening Displacement (CMOD) obtained from the FE models of different loading rates. 82

LIST OF SYMBOLS

a	Crack Length
A	Austenite
A_1, u_{0y}	Rigid Body Parameters
A_f	Austenite Finish Temperature
A_s	Austenite Start Temperature
B	Specimen Thickness
C_A	Clausius - Clapeyron Constant for Austenite
C_M	Clausius - Clapeyron Constant for Martensite
E	Young's Modulus
E_A	Young's Modulus of Austenite
E_M	Young's Modulus of Martensite
G	Energy Release Rate
J	$J-$Integral
K	Stress Intensity Factor
K_c	Fracture Toughness
K_I	Mode-I Stress Intensity Factor
K_{Ic}	Mode-I Critical Stress Intensity Factor
K_{II}	Mode-II Stress Intensity Factor
K_Q	Mode-I Critical Stress Intensity Factor for Plane Strain
M	Martensite
M_f	Martensite Finish Temperature
M_s	Martensite Start Temperature
P_{max}	Maximum Applied Load
P_Q	Critical Load
r	Radial Polar Coordinate
R_f	R-Phase Finish Temperature
R_s	R-Phase Start Temperature
r_M	Full Martensite Region
r_p	Plastic Zone Size

r_T	Phase Transformation Region
T	Temperature
u_y	Displacement Component in y Direction
$T-$stress	Stress Component Parallel to Crack Plane
W	Specimen Width
ϵ_{eq}	Equivalent Strain
ϵ_{MF}	Martensite Transformation Finish Strain
ϵ_{MS}	Martensite Transformation Start Strain
$\epsilon_{xx}, \epsilon_{yy}, \epsilon_{xy}$	Strain Field Components
μ_{tip}	Shear Modulus of Crack Tip
ν	Poisson's Ratio
σ_{AF}	Austenite Transformation Finish Stress
σ_{AS}	Austenite Transformation Start Stress
σ_{MF}	Martensite Transformation Finish Stress
σ_{MS}	Martensite Transformation Start Stress
σ_f	Orientation Finish Stress
σ_s	Orientation Start Stress
σ_{UTS}	Ultimate Tensile Strength
σ_{YS}	Yield Stress
$\sigma_{xx}, \sigma_{yy}, \sigma_{zz}$	Stress Field Components
$\sigma_{xy}, \tau_{xz}, \tau_{yz}$	Shear Stresses
θ	Angular Polar Coordinate
ζ	Martensite Volume Fraction

LIST OF ACRONYMS/ABBREVIATIONS

1D	One Dimensional
2D	Two Dimensional
3D	Three Dimensional
ASTM	American Society for Testing and Material
CCD	Charge Coupled Device
CT	Compact Tension
CMOD	Crack Mouth Opening Displacement
CTOD	Crack Tip Opening Displacement
DIC	Digital Image Correlation
DSC	Differential Scanning Calorimetry
EDM	Electrical Discharge Machining
FE	Finite Elements
FEA	Finite Element Analysis
FEM	Finite Element Method
LEFM	Linear Elastic Fracture Mechanics
LPS	Lower Plateau Strength
NiTi	Nickel Titanium
NOL	Naval Ordinance Laboratory
RD	Rolling Direction
SE	Super Elasticity
SIF	Stress Intensity Factor
SIM	Stress Induced Martensite
SMA	Shape Memory Alloy
SME	Shape Memory Effect
UMAT	User Defined Material Subroutine
UPS	Upper Plateau Strength

1. INTRODUCTION

1.1. Shape Memory Alloys

Shape Memory Alloys (SMAs) are smart materials, well known with their shape recovery capabilities that allow them to turn back to their initial shapes after large inelastic deformations upon an increase in their temperatures. Early discoveries on the memory effect were made by Ölander in 1932 [10] in AuCd, and in 1938, Greninger and Mooradian [11] observed the shape memory effect in CuZn alloys. But the works of William J. Buehler and co-workers were the breakthrough in the SMAs. They discovered the shape memory effect of Nickel Titanium (NiTi) alloy in 1963 which they named NiTi-NOL as a reference to the Naval Ordnance Laboratory. They applyed for the very first patent on SMAs which leaded to it's acknowledgement by other researchers [12].

NiTi undergoes solid to solid diffusionless phase transformation between two phases: austenite and martensite. This phase change is the effect of two mechanisms. The first one is known as the superelasticity which is the phase transformation from the parent phase austenite to martensite as a result of loading. The second is the shape memory effect which is the effect of the temperature change. Decreasing the temperature causes the austenite phase to transform into martensite.

1.1.1. Superelasticity and Shape Memory Effect

Superelasticity also known as the pseudoelasticity is the phase transformation mechanism of SMAs which occurs at a constant temperature higher than the characteristic austenite finish (A_f) temperature. At that temperature, NiTi is at full austenitic phase. Transformation from autenite to martensite (A $\rightarrow$ M) occurs upon applying load to the material and the transformation continues until all the austenite changes into martensite due to stress increase and returns back to the austenitic phase upon unloading to zero stress state. This behavior is illustrated schematically in Figure 1.1.

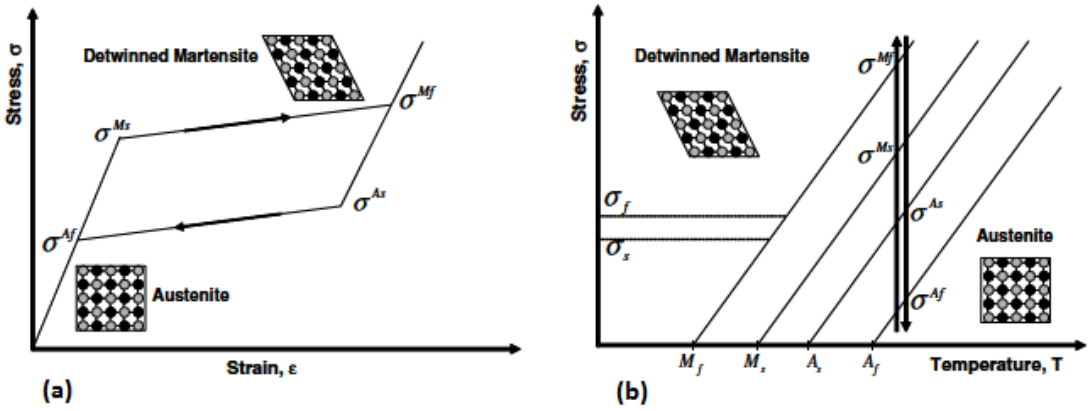


Figure 1.1. (a) Superelastic Stress - Strain Diagram (b) Superelastic Loading Path on Stress - Temperature Diagram [1].

σ_{MS}, σ_{MF}, σ_{AS} and σ_{AF} at Figure 1.1 denote the forward transformation start, finish and reverse transformation start, finish stresses, respectively. M_f, M_s, A_f and A_s are the phase transformation temperatures at zero stress and are measured using Differential Scanning Calorimetry (DSC).

During the phase transformation, a high amount of macroscopic strain of about 8% to 11% occurs, which is not a common property for most metals that can only have an elastic strain of less than 1 %. The start of the martensitic transformation is indicated by a change in the slope of the stress - strain curve. When the transformation starts, strain increases under a rather constant stress to large inelastic strains and the slope of the stress - strain curve increases with elastic transformation of the martensite phase following the completion of the phase transformation to full martensite. Upon unloading martensite phase starts to turn back to austenite since martensite phase is not stable at high temperatures. Unloading follows a different path, and a hysteresis that is unique for SMAs, is obtained. Figure 1.1 illustrates a schematic of a stress - strain diagram of superelastic SMAs.

Shape memory effect corresponds to the phase transformation mechanism of SMAs deformed at the temperatures below the characteristic austenite start (A_s) temperature. When the temperature of the material is decreased to a temperature below

the characteristic martensite finish temperature (M_f), in the absence of an applied load, the austenite phase transforms into twinned martensite phase.

If the material that is in the state of twinned martensite is loaded to a stress level higher than the orientation start stress σ_s, the material starts to transform to detwinned martensite. This process continues until the stress value reaches σ_f which is the reorientation finish stress. Upon unloading, there remains a large residual strain and only the elastic strain is recovered, the material stays in the detwinned martensite phase. Heating the material initiates the reverse phase transformation and the material returns to austenite phase. With the completion of the reverse transformation, the residual plastic strain is recovered and the initial shape is regained. Figure 1.2 illustrates the shape memory effect.

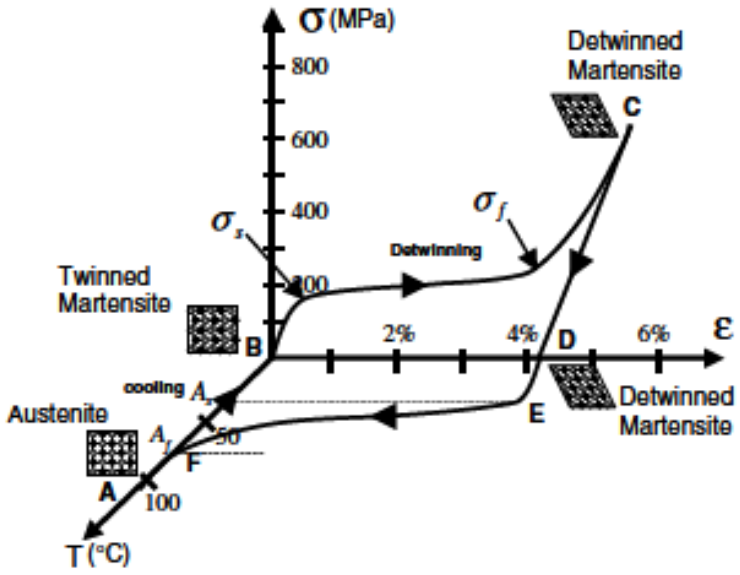


Figure 1.2. Stress - Strain - Temperature Diagram Illustrating the Shape Memory Effect [1].

1.2. Works on Fracture of SMAs

Works on material properties and fracture behavior of SMAs have been done by a considerable number of researchers. In this section, summaries of the studies performed

on fracture mechanics and fracture toughness of SMAs by previous researchers are presented.

In 1995, Stam and van der Giessen [13], studied the effect of partial or full reversibility of stress induced phase transformation on the size and shape of the transformation zone around the crack tip, and on toughness during crack growth in zirconium ceramics and SMAs using finite elements analyses. They used the constitutive equations proposed by Sun and Hwang [14], and found that toghness of the material increases due to irreversible phase transformations.

Birman [15], in 1998, investigated the fracture behavior of an SMA plate under Mode-I loading to calculate the size of the stress-induced phase transformation region in front of the crack and the effect of the phase transformation on the stress intensity factor using the constitutive model proposed by Tanaka and Sato [16]. He concluded that, phase transformation effect is rather small thus the stress intensity factor may be calculated using the material properties of austenite.

The effect of the phase transformation of SMAs under Mode I loading on fracture toughness was also investigated by Yi and Gao [17] in 2000 using the inclusion and the weight function method of Eshelby [18] with Sun and Hwang's [19] constitutive model. They analyzed the shape and the size of the transformation region for stationary and steady advanced cracks. They concluded that the stress intensity factor decreases and the toughness increases with martensite transformation. Also, they found that the temperature increase causes the crack tip SIF to decrease. They showed that, larger ratio of elastic moduli between the martensite and the austenite phases causes the crack tip stress intensity factor to decrease.

Mc Kelvey and Ritchie [20] studied the fatigue-crack propagation behavior in the superelastic NiTiNOL, in 1999. They compared NiTiNOL with the other biomedical implant alloys and found that the fatigue crack growth resistance of Nitinol was the lowest.

In 2002, Yan *et al.* [21] investigated the effect of volume contracting transformation on the toughness of superelastic SMAs. They analyzed transformation induced SIF for a quasi-static advancing crack using finite element method. Also they calculated the crack tip SIF using the equations proposed by Mc Meeking and Evans [22] and Hutchinson [23]. They concluded that, even if the transformation volume contraction strain is small, it increases the effective stress intensity near an advancing crack, hence the toughness of SMAs is reduced. Also, they stated that reverse transformation effect is negligible on transformation induced SIF because reverse transformation occurs only partially in the wake of an advancing crack tip, and volume-expanding transformation may increase the toughness, but reverse transformation might reduce the toughness greatly in the wake of the crack tip.

Wang [24] studied the effect of different notch geometries on fracture behavior of NiTi SMA by calculating the stress - strain distributions and phase transformation region sizes around the crack tip using finite element method (FEM). He found that, changing the notch geometry from blunt to sharp increases the stresses around the crack tip. His results on the phase transformation showed that the transformation zone shape is not affected by the notch geometry but the size of the transformation zone around the crack tip is smaller for the sharp cracks. Also plastic zone around the crack tip of a sharp crack forms at lower loads compared to the blunt notches.

Experimental determination of fracture toughness were done by Wang *et al.* [25] in 2008 using fatigue precracked compact tension (CT) specimens. They calculated the stress intensity factor. They observed that during fatigue precracking a small area around the crack tip transforms partially to martensite. They presented that if the crack growth is fast, there always occurs a small area that transformed fully to martensite around the tip of the crack.

Daly *et al.* [26] in 2007, investigated the fracture properties of thin NiTi sheets under Mode I loading using digital image correlation (DIC) technique and calculated the strain fields of the specimen surface. They also calculated SIF using linear elastic fracture mechanics (LEFM) and obtained an empirical relation between the phase

transformation region size and the SIF. They concluded, the phase transformation results in toughening around the crack tip.

In 2007, Robertson *et al.* [27] measured the strain field around the tip of an edge cracked NiTi specimen using the X-Ray diffraction method. They observed that stresses around the crack tip reduce due to phase transformation and this results in an increase in the fracture toughness.

Gollerthan *et al.* [28] in 2008, conducted experiments using NiTi CT specimens and calculated the critical stress intensity factor K_Q using the emprical relations given by the ASTM E399 [8]. They used K_Q and the Irwin's plasticity corrected equation to estimate the length of the phase transformation zone along the crack tip and observed that they agree well with each other.

In 2007, Freed and Banks-Sills [29] investigated computationally the transformation toughening behavior of a slowly propagating crack in an SMA plate under plane strain conditions and Mode I loading. Assuming a small scale transformation zone and using the transformation surface equation proposed by Panoskaltsis *et al.* [30] and the asymptotic stress equations, they calculated the phase transformation region. They found the transformation zone shapes around the crack tip to be similar to the plastic zone shape in the plastically deformed materials. They stated that phase transformation and the difference between the elastic moduli of the initial and the deformed phases causes the critical steady state SIF to increase. Their results support the idea that reversible phase transformation reduces the toughening.

Lexcellent and Tiebaud [31] presented a analytical method for determining the phase transformation region around a Mode I crack tip using the model proposed by Raniecki and Lexcellent [32] with asymptotic crack tip stress equations. They also calculated a stress intensity factor similar to Freed and Banks-Sills [29] approach. They compared their analytical results to Robertson *et al.*'s experimental results and reported a significant difference.

In 2009, Falvo *et al.* [4] calculated the fully martensitic region size using the asymptotic crack tip equations for the case $\theta = 0$ and Irwin's plasticity corrected formula for the plastic zone size. They also performed finite element analyses and compared the analytical results with the computational results. Their conclusion showed that Irwin's formula gives close results to finite element results.

Maletta and Young [33] in 2011, extended the formulation for plane strain conditions using the analytical method proposed by Maletta and Furgiuele [34] to computationally calculate the phase transformation region size using the Irwin's formula and the stress intensity factor calculated with the far field stress values for a Mode I center cracked infinite NiTi plate. They compared their analytical results to Gollerthan *et al.*'s [35] experimental results and concluded that Gollerthan *et al.*'s results are between their calculations for plane stress and stain conditions. They also presented that the phase transformation strain and the plateau stress affects the phase transformation size that, with increasing transformation strain and decreasing plateau stress the size of the phase transformation region increases.

In 2012 Baxevanis and Lagoudas [36] investigated the fracture behavior of a center-cracked superelastic SMA infinite plate under plane stress condition and Mode I loading using the Dugdale [37] assumption, presented an expression for calculating the J-integral, crack opening displacement and the phase transformation size using the far field stresses. Their results showed that in the case the stress level is above the yield stress, size of the phase transformation region increases with increasing transformation strain. Also they concluded that the phase transformation at the crack tip decreases the plastic zone size.

1.3. Effect of Loading Rate

Generally, temperature variance affects the elastic properties of metals and a temperature rise occurs in the material due to high strain rate loading conditions [38]. For SMAs, stress induced phase change causes local self heating in the material during loading and self cooling during the unloading process and this temperature change

affects the material behavior and the phase transformation mechanisms [39]. This phenomenon is the result of thermo-mechanical coupling of SMAs [40]. In literature there are various investigations of the effects of strain (loading) rate on SMAs. In this section, summaries of previous studies on strain (loading) rate effect and the thermomechanical effect of SMAs are presented.

In 2003, Prahlad and Chopra [40] presented a constitutive model that is derived from the model proposed by Brinson [41] to estimate the strain rate effect on the mechanical behavior of SMA models under uniaxial loading at constant temperature.They conducted uniaxial tensile tests using wire specimens at different loading rates to determine the parameters required for the constitutive model and validation was made by comparing to the experimental results. Their results showed that the strain rates, empirically determined to be below 0.0005 1/s, do not have any significant effect on the material characteristics. But the transformation stresses and the temperature of the material increased at a strain rate of 0.01 1/s. In addition, the constitutive model that was proposed showed good agreement with the experimental results under different loading rates.

In 1998, Tobushi *et al.* [42] investigated the influence of strain rate on superelastic properties of TiNi SMAs by performing tensile tests on TiNi SMA wires. They concluded that for the strain rates higher than 10 % /min, the martensite transformation stresses and the temperature of the specimen increases in the loading process but in the unloading process the reverse transformation stresses and the temperature decreases with increasing strain rates. But for the strain rates lower than 2 % /min superelastic material properties did not show dependence on the strain rate and the temperature variance was negligible.

Kim and Cho [43] conducted one dimensional tensile experiments and proposed a simple constitutive model based on their experimental results and the first law of thermodynamics for NiTi SMAs. They carried out tension experiments at low strain rates between 0.01/min and 0.1/min at different environmental temperatures of about 30, 35, 40, 45 and 50 °C and found that under the quasi-static strain rate of 0.01/min,

the temperature variation was so small that no physical change is observed from these tests. But over this strain rate with increasing strain rates the M_s and M_f transformation stresses increase monotonically as the A_s and A_f transformation stresses decrease. Also they observed that exothermic response during forward transformation and endothermic response during reverse transformation occurs. So the absolute temperature variation increases during transformation as the strain rate increases from 0.01/min to 0.1/min. They concluded that, increasing strain rates affect an SMA's temperature during both forward and reverse transformation and this variation in the temperature affects the forward and reverse transformation stresses. Also they stated that, the thermal reactions result in higher forward transformation stress and the reverse transformation stress lowers with increasing strain rates.

Pieczyska *et al.* [44] in 2006, performed strain and stress controlled tensile tests on superelastic NiTi SMAs using a belt type specimen with different strain and stress rates. They observed that the effect of the strain rate is higher for the strain controlled tests. They measured the specimen surface temperature using a infrared camera. They observed that the stress - strain curves are dependent on the strain rate and the stress values increase during phase transformation with increasing loading rate. The stress - strain curve at a very low strain rate was found to be almost flat during phase transformation and for higher strain rates the curve showed a steeper slope. They also observed that the temperature of the specimen increases during phase transformation and the temperature change was between 26 to 40 K, depending to the strain rate case.

Kadkhodaei *et al.* [45] presented a 1D continuum thermodynamic constitutive model using a Helmholtz free-energy function which consists of strain energy, thermal energy and the phase transformation energy for investigating the SMA wires' behavior subjected to non quasi-static loadings. They used Brinson's [41] model for the evaluation of martensite fraction and their model can be used to predict both the shape memory and superelastic effects. They used FEM to calculate the material response. They compared their results for stress, strain and temperature to the experimental results of Vitiello *et al.* [46] and Prahlad and Chopra [40] for determination of the coefficients. They observed from the stress - strain curves stress increases with in-

creasing strain rate and the energy dissipations showed significant dependence to the applied strain rate. For the shape memory case they did not observe any dependency to the strain rate because for during transformation latent heat generation does not occur hence the temperature changes become negligible and the transformation stresses becomes independent of the temperature for this temperature range.

In 2010, Zhang *et al.* [47] conducted uniaxial tensile tests using NiTi strips and measured the stress - strain curves and the temperature fields at various stretching rates. Their results showed strong dependence to the strain rate. They reported that the temperature dependence is almost negligible and the stress - strain curve has a flat plateau during transformation. For the high loading rates a high temperature change was observed and the stress - strain curve changed to a hardening type and the stress hysteresis increased monotonically with increasing strain rate. They stated that because of the self-heating/cooling characteristics and the heat exchange with the environment, temperature and the phase transformation stresses changes with strain rate variance that leads to a change in the hysteresis loop.

Churchill *et al.* in 2010 [48] investigated the thermomechanical coupling effects on the superelastic SMA wires. They reported that stress induced phase transformations are rate dependent and the reason behind this is the temperature change. The rate dependence comes from the strong thermo-mechanical coupling inherent to SMAs, that is caused by latent heat variance and temperature dependence of the transformation stresses.

Roh [49], in 2014 investigated the thermomechanical behavior of SMAs experimentally and numerically. He stated that phase transformation stresses, the slope of the transformation plateau and the temperature are affected by the strain rate. He also proposed a strain rate dependent 1D incremental formulation of SMAs and stated that this model predicts well the thermomechanical characterisitcs, stress - strain curves and the temperature variation for different loading rates.

In 2010, Saletti *et al.* [50] studied the evolution of the stress induced martensitic transformation under different strain rates in a single NiTi plate-shape specimen using DIC and IR thermography measurement techniques. They conducted quasi-static and dynamic tensile tests at different strain rates ranging from 10^{-4} $1/s$ to 15 $1/s$ at room temperature and concluded that strain rate does not have any effect on the growth rate of the transformation zone for in this rate interval.

Huang *et al.* in 2013 [51], investigated the loading rate effect on the martensitic transformation of NiTi SMAs. They conducted quasi static tensile and impact loading tests and used DIC for strain field measurements. Their results showed a significant increase of the stress level at impact loading case.

In 2008, Imanol *et al.* [52] presented a constitutive model based on the model of Liang and Rogers taking strain rate dependence into account, that represents the uniaxial loading behavior of an SMA wire superelastic stress – strain under low velocity impact loading. They stated that, at high strain rate tests, because of the heat generation during the phase transformation increases the material's temperature and this leads to an increase in the transformation stresses. They found good agreement with the experimental and the computational stress - strain curves. Also they stated that the elastic moduli of austenite and martensite are rate independent.

In 2008, Auricchio *et al.* [53] proposed a uniaxial thermo-mechanical constitutive model to create the superelastic rate dependent effect of SMAs. Their model also considers the elastic properties of austenite and martensite. They compared the numerical data with experimental results and the quasi-static tests showed good agreement. But different rate dependency of different experimental data sets, strongly affected the comparisons of dynamic tests with the simulations. Their numerical and experimental results showed dependence to the changing test frequencies that, for higher loading frequencies the stress - strain curves moved upwards.

Zhu and Zhang [54], also presented a thermomechanical model to predict the uniaxial superelastic cyclic behavior of SMA wires at different loading rates using the

model of Tanaka [55]. To validate the model they proposed, they conducted uniaxial tensile tests at different loading rate at room temperature. They stated that both the numerical and the experimental results showed that the loading rate affects the thermomechanical behavior of NiTi and the thermal effect caused by loading rate is not negligible. The constitutive model they proposed was in good agreement with the experimental results. Their results showed that the loading plateau moves upwards while the unloading plateau moves downwards with increasing loading rate. At the quasi static loading rate the plateaus were found to be rather flat.

He and Sun [56] studied the temperature variation of NiTi SMAs subjected to different loading frequencies, in 2010. They proposed a simple analytical model to calculate the temperature evaluation of a NiTi bar. They stated during the loading - unloading processes temperature of the specimen changes due to latent heat generation and the dissipative work and the temperature affects the transformation stresses since transformation stresses depend on the temperature through the Clausius-Clapeyron equation. This temperature variation is effected by the different loading frequencies and with increasing loading frequency, mean temperature of the specimen increases. Comparisons of the analytical calculations of the mean temperatures showed good agreement with the experimental results. In a subsequent study by Yin *et al.* [57] in 2014, they found similar results.

Dolce and Cardone (2001) [58] carried out cyclic tensile tests on Ni-Ti wires for the strain rates in the range of 8.10^{-4} to $0,32.10^{-1}\,1/s$ to investigate the temperature, loading frequency and number of cycles effects on the mechanical properties of NiTi wires. They observed a significant decrease of energy loss and equivalent damping due to the temperature increase which occurs because of the latent heat of the phase transformation that can not be dissipated to the surroundings for high strain rates. They stated that the increase in the temperature results in an increase in the critical transformation stresses.

DesRoches *et al.* [59] in 2004 performed cyclic tensile tests on wires and bars and found an increase in both forward and reverse transformation stresses and the plateau

stresses and a reduction in the hysteresis area with increasing strain rates.

Qiana *et al.* in 2010 [60] conducted cyclic tensile tests experimentally and numerically based on the Liang and Roger's constitutive model. They investigated the influence of strain rate on the mechanical properties of SMA wires under different loading rates both experimentally and numerically and they found that the stress-strain curves move upwards with increasing rates. They also indicated that the increase in the loading rate causes hardening owing to the increase of the stiffness of the elastic field.

Qian *et al.* (2013) [61] proposed a uniaxial constitutive model based on the Graesser and Cozzarelli's model to investigate the strain rate effect on the mechanical properties of SMAs experimentally and numerically. They carried out cyclic tensile tests on supereastic NiTi wires for different strain rates. Their results showed that the stress change $\Delta\sigma$ increases with increasing strain rate both at the forward martensitic transformation and the reverse martensitic transformation.

In 2012, Araki *et al.* [62] conducted tensile cyclic tests on superelastic Cu–Al–Mn alloy rods to investigate the loading rate effect on the constitutive relations. Their results showed that the forward transformation stress increase due to increasing loading rate was less than 5 %. They stated that this increase is much smaller than the NiTi alloys reported in literature that superelastic Cu–Al–Mn alloy's forward transformation stress increase is 1/4 of NiTi alloys. They concluded that superelastic Cu–Al–Mn alloys are insensitive to loading frequencies.

Morin *et al.* [63], in 2011 extended the Zaki–Moumni model for SMAs to take the thermomechanical coupling into account. They performed tensile tests and finite element simulations for different strain rates. Their results showed that during forward phase change the slope of the transformation region on the stress - strain curve increases while during the reverse phase change the transformation plateau shifts downwards with increasing loading rates due to the temperature change at the phase transformation. They stated following this discussion, that the hysteresis area expands. Comparison

between the simulations and the experiments showed good agreement for the quasi static loading case but only a qualitative agreement for the high loading case. In another study Morin *et al.* [64] performed cyclic tensile tests under different loading rates and found that phase transformation yield stresses and slopes of the phase transformation region on the stress - strain curves as well as the hysteresis area change with strain rate variance.

Adharapurapu *et al.* [65] performed tension and compression tests at high (1200/s) and low (0.001/s) strain rates at different temperatures. They reported that in case of dynamic loading the slope of the stress induced martensite region is higher than the low strain rate case. They observed the critical stress value which was determined by 0.2% strain offset, was higher for the dynamic tension test about 100 - 200 MPa; for the compression tests this difference was about twice the low strain rate tests.

In 2005, Nemat-Nasser and Choi [66] performed compression tests to investigate the deformation mechanism of a Ni-Ti-Cr SMA at different initial temperatures and strain rates. Their results showed that the deformation of the alloy is strongly dependent to the strain rate. They stated both temperature and the strain rate affects the superelastic and yielding behavior. In the case of stress induced martensite formation, yield stress of the martensite and the parent austenite phases are dependent to strain rate and the yield stresses increase with increasing strain rate.

Nemat-Nasser *et al.* studied the effect of high strain rates on compressive response of NiTi SMAs [67, 68] and found that the forward transformation stress (A $\rightarrow$ M) increases abruptly, hence proves to be strain rate dependent in the ranges considered in their study.

Nemat-Nasser and Guo [38], in 2006, performed series of uniaxial compression tests under different strain rates in the range of $10^{-3}/s$ to $4200/s$ and at various initial temperatures up to 400 K to see the effect of thermomechanical response on NiTi SMA wires. They conducted the compression test using the Hopkinson technique, but since controlling the unloading rate is not easy, they only focused on loading rates.

They observed that the transformation stresses increase with increasing strain rate and the plateau range disappears as the strain rate increases up to 4200/s. They stated that stress - strain curves for loading rates between 0.1 to 2100/s loading portions of the curves look similar but the stress levels are higher for the high strain rates and for very high strain rates the stress - strain response is similar to ordinary austenite metals. They also conducted new set of experiments at different initial temperatures and concluded that the transformation stresses increase with increasing temperature.

As summarized above, SMAs' rate dependent behavior was studied by many researchers. Tensile, cyclic, compressive experiments as well as computational simulations were performed under different loading rate conditions. But there is only a few study on the effect on fracture. They are presented below:

Ardakani *et al.* [69] in 2015, investigated the fracture behavior of SMAs using XFEM considering the thermo-mechanical coupling effects. They performed several simulations by changing the thermodynamic characterisitcs of the material (transformation stress and maximum transformation strain) to see the phase transformation region changes for a stationary central crack under mode I loading. They stated that, loading rate strongly affects the stress field, temperature and the phase transformation region size around the crack tip. They found with high loading rates the A $\rightarrow$ M transformation stress and hardness of the SMA material increases. They have also seen that the extent of the austenite and the martensite diameters have significant difference between the high and slow loading rates. In the case of the slow loading rate martensite and transformation zones are larger than the higher loading rate case.

In 2007, Jiang and Vecchio [70] conducted four point bending fracture tests under dynamic and quasi-static loading conditions and observed different fracture mechanisms for each case. They reported that the fracture toughness of NiTi SMA increases with increasing loading rate and stated this difference may have two possible explanations. One is that under dynamic loading condition the phase of the material at the time of the fracture is different than the quasi-static loading case. Second suggestion was that the austenite mechanical behavior is affected by the loading rate that it becomes more

ductile and stronger at the dynamic loading condition so that the fracture toughness of the material increase with respect to the quasi-static loading case.

1.4. Objectives

There has been an increasing interest in effect of loading rate on mechanical behavior of SMAs. Changing the loading rate has an effect on temperature of the specimen, and this causes the phase transformation stresses to shift. There are works on the effect of loading rate on transformation stresses, superelastic behavior and mechanical properties of SMAs. Most studies have found a change in the stress-strain curve with increasing loading rate. They reported that during martensitic phase transformation the stress ratio increases as the loading rate increases.

On the other hand there are fewer works done to study the effect of loading rate on stress induced martensitic phase transformation and fracture behavior of SMAs. A few analytical, experimental and computational analyses were done to characterize the fracture behavior of SMAs under changing loading rate. They investigated martensitic transformation toughening behavior, and calculated the stress intensity factors (SIF) and martensitic transformation zones. Ardakani *et al.* [69] calculated computationally the martensitic transformation region of an edge cracked SMA specimen under Mode I loading by implementing the thermodynamic characteristics of the material that change under different loading rates. They found that the phase transformation region size decreases with increasing loading rate. Jiang and Vecchio [70] measured the stress intensity factors of bending specimens under quasi static and dynamic loadings. They found that the stress intensity factor increases significantly with increasing loading rate. Studies on the effect of loading rate on fracture behavior of NiTi are still not sufficient in number and there is a need for additional experimental, analytical and computational works on SMAs at various loading rates.

The main objective of this thesis is to study the effect of loading rate on phase transformation region and fracture parameters of NiTi. The phase transformation size around the crack tip is evaluated experimentally using the results of DIC. It is

also calculated analytically and then computationally using finite elements. Stress intensity factors are calculated experimentally using DIC and ASTM E399. Use of the full displacement from DIC conducted at different loading rates is a dependable approach for the evaluation of the stress intensity factor and the phase transformation region.

The outline of this thesis is as follows: In Chapter 2, series of tests conducted for the characterization of the material are presented. Differential Scanning Calorimetry (DSC) is used to determine the transformation temperatures, and tensile test are done to determine the mechanical properties of NiTi at different loading rates. Next, using the results of the tensile tests performed at different testing temperatures, the Clausius-Clapeyron constants are obtained, and the results are compared to those of Falvo *et al.* [4] and Tanaka *et al.*'s [5]. Chapter 3 is devoted to the evaluation of fracture parameters. Critical Stress Intensity Factors are calculated using the empirical equations of ASTM E399, and using the results of DIC performed on pre-cracked, Mode I Compact Tension (CT) specimens at different loading rates. In Chapter 4, the phase transformation region around the crack tip is evaluated experimentally using DIC, and is calculated analytically with the equations proposed by Hazar *et al.* [71] using the SIF values obtained from both DIC and ASTM E399. In Chapter 5, using the material properties obtained from tensile tests at different loading rates and results of the fracture tests Finite Elements (FE) models are built to calculate the phase transformation regions J contour integral values are evaluated and SIF values are calculated. Next, SIFs are also calculated using the full displacement field obtained from finite elements. Also, the Crack Mouth Opening Displacement (CMOD) values are calculated.

2. MATERIAL CHARACTERIZATION

The material has the composition of 55.99% Nickel, less than 0.05% C and 0.05% O, with total of 0.2% Co, Cr, Cu, Fe, Mn, Mo, Nb, Si, W elements and a balanced amount of Titanium. The additional data provided by the manufacturer includes the tempering method (flat annealed), surface treatment method (pickled), ultimate tensile strength of the material ($\sigma_{UTS} = 1517$ MPa), an elongation of 12% and austenite finish temperature of 16.1 °C, which also indicates that the material is superelastic at room temperature.

Experiments for material characterization were done using one mm thick NiTi sheets, produced in accordance with ASTM F2063-12 standard. The samples were cut along the rolling direction (RD) with electrical discharge machining (EDM) to minimize the effect of cutting, because NiTi is a material that is easily affected by machining processes. The sample's dimensions were adapted from the standard for the tension testing ASTM E8/E8M - 15a. The dimensions of the sample used for the tests were chosen to fit the capacity of the test machine used, which has a loading capacity of 10 kN. At Figure 2.1 the drawing and the photo of the test specimen is presented. Dimensions are in millimetres.

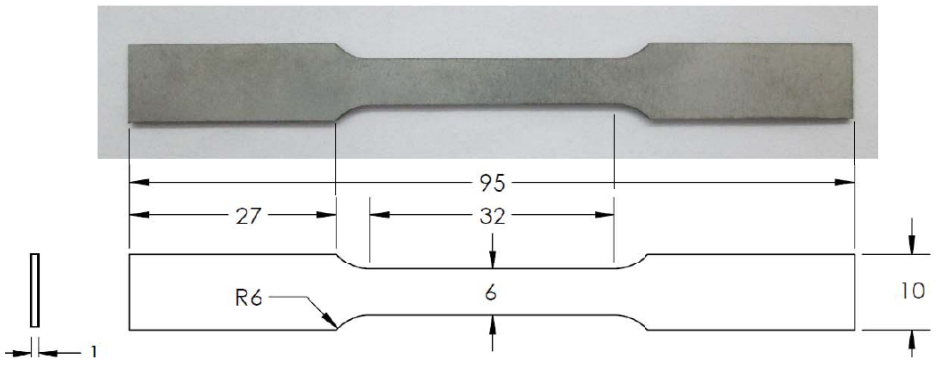


Figure 2.1. Dimensions of NiTi Tensile Test Specimen in mm.

Although the manufacturer provided some of the mechanical and physical properties of the material, there is need for independent characterization completely. For this

purpose tensile tests were done according to both ASTM E8/E8M - 15a and ASTM F2516 - 14. The first of these is the standard tension testing of metallic materials and the subsequent one is for tension testing of superelastic NiTi materials.

2.1. Differential Scanning Calorimetry (DSC)

Differential scanning calorimetry is a thermal analysis technique conducted to determine the phase transformation temperatures of the materials. NiTi is a material which is present in two different phases, martensite and austenite, due to it's shape memory effect (SME) under different ambient temperature conditions. Since it is an important parameter for the experiments to know the material's parent phase at the room temperature, the first step to do experiments was determining the phase transformation temperatures of NiTi. DSC test method is basically consist of cooling and then heating processes of a test sample at a pre-defined temperature rate in a controlled medium. During the test, the heat flow difference based on the energy variance is recorded. Energy absorption by the material causes an endothermic reaction and the release of energy causes an exothermic reaction due to phase transformations. These reactions occur at the peaks of the heat flow - temperature curves as illustrated at Figure 2.2.

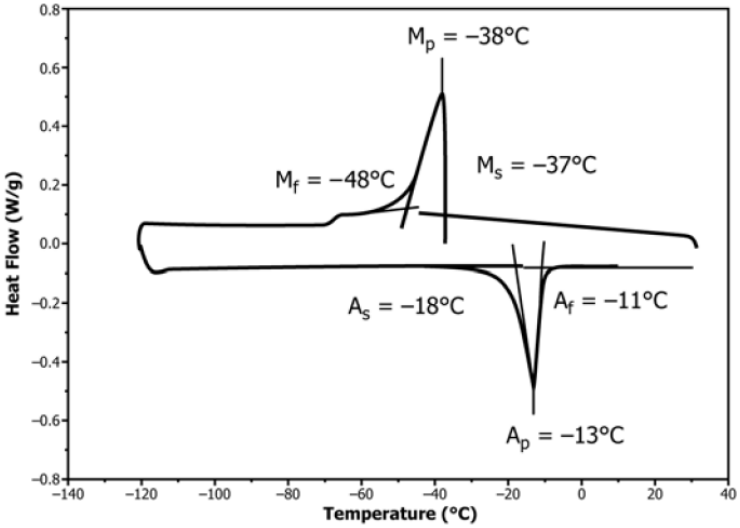


Figure 2.2. DSC Curve of NiTi [2].

A sample weighing 4.9 mg was used in the DSC test. The sample was placed into an aluminum pan and the pan was pressed using a hand presser to obtain the maximum surface contact of the NiTi specimen with the pan. The heating and cooling rates were set to 10 °C/min and the sample was first cooled to -100 °C from the room temperature. Next the sample was heated to 100 °C and then cooled back to -100 °C. The purge gas was liquid nitrogen and the differential scanning calorimeter used for the test was Exstar DSC 7020, presented at Figure 2.3.

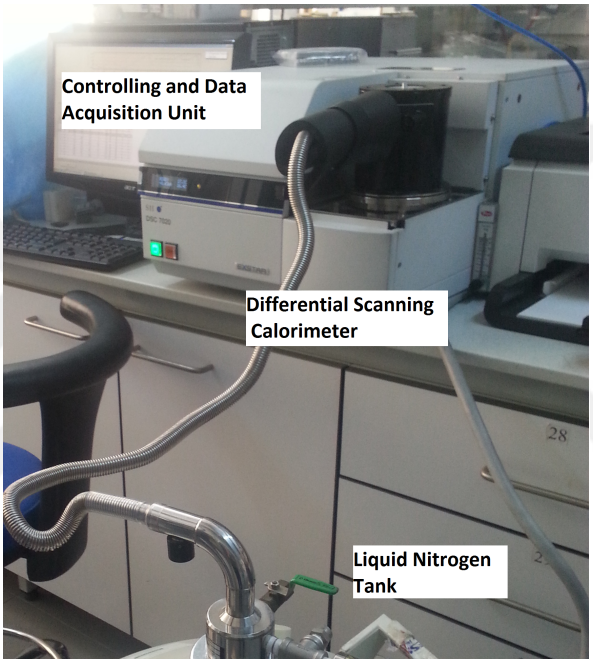


Figure 2.3. Differential Scanning Calorimeter.

Phase transformation temperatures (martensite start (M_s), martensite finish (M_f), austenite start (A_s) and austenite finish (A_f)) were obtained from the heat flow - temperature diagram shown in Figure 2.4, as explained at the ASTM F2004 – 05 [2]. The cooling and heating directions are as illustrated on the figure. The transformation temperatures are the intersection points of the straight portion of the curve with the peaks' related inclinations which are shown at Figure 2.2. Generally the peak on the heating curve gives the transformation temperatures of the austenite phase and the one on the cooling curve gives the transformation temperatures of the martensite phase.

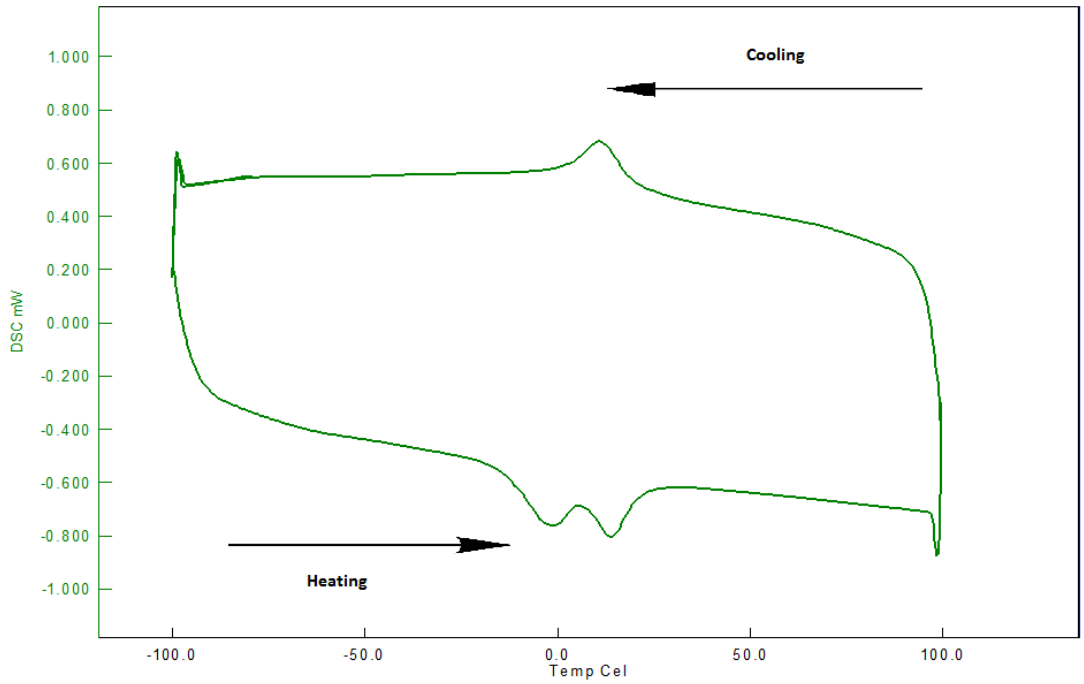


Figure 2.4. Differential Scanning Calorimetry of the Material.

The first peak occurred during heating indicates the R-phase which is actually a rhombohedrally distorted martensite. Usually R-phase occurs only during cooling but in some other cases R-phase is seen during both cooling and heating which is called symmetric R-phase transformation [72]. At Figure 2.4 only the R-phase during heating can be seen. Because austenite to R-phase transformation has lower hysteresis, the R-phase - austenite peaks are close to each other. Since this DSC test was done in the temperature interval of -100 °C to 100 °C, the R-phase transformation temperatures (R-phase start temperature R_s and R-phase finish temperature R_f) can not be seen on cooling because the martensite to R-phase transformation has higher hysteresis and the transformation temperatures of the R-phase during cooling are lower than -100 °C.

The transformation temperatures obtained from the DSC curve following the procedure explained at the ASTM F2004 − 05 standard [2] are presented at Table 2.1.

The austenite finish transformation temperature obtained from DSC was not found to be in agreement with the one provided by the manufacturer which was 16.1

Table 2.1. Transformation temperatures obtained from DSC curve.

M_s (°C)	M_f (°C)	R_s (°C)	R_f (°C)	A_s (°C)	A_f (°C)
23.6	-3.4	-12.8	4.7	6.9	24.8

°C. This may be a result of the cutting process of the sample that can cause cold work, which affects the transformation temperatures. Also, it was stated at the ASTM F2004 − 05 [2], that, the transformation temperatures obtained from other test methods may be different due to the effects of strain and load on the transformation.

2.2. Tensile Tests

For uniaxial tensile testing of the material, ASTM F2516 - 14 standard was followed. The standard requires the specimen to be loaded up to 6% strain to avoid the plastic effects and unloaded back to 7 MPa stress for obtaining the hysteresis loop, then loaded until failure. Since the material used in the present study did not show any distinct transformation to full martensite at the strain value of 6%, all specimens were loaded up to 8% strain.

The tests were conducted under displacement control for the chosen loading rates, that are 0.1 mm/min, 0.5 mm/min, 1 mm/min, 1.5 mm/min and 2 mm/min, respectively. The loading rates for the tensile tests were chosen to be in the quasi-static range, so that the material shows the effect of loading rate and still does not have too much difference on the material properties due to the thermo-mechanical coupling. Material's temperature changes distinctively at very high loading rates during transformation. These changes in the temperature of the material during the forward transformation effect the material's phase transformation mechanism and as a result the material may go to failure before full transformation from austenite to martensite. This is an undesirable effect for the purpose of this study.

From the tensile tests, Upper Plateau Strength (UPS) and Lower Plateau Strength (LPS), were obtained as stated in the standard for tension testing of superelastic NiTi, which are the corresponding stresses of 3% strain at loading and 2.5% strain at unloading, respectively.

Young's Modulus of austenite and martensite, for each loading rate within the scope of this study, were obtained from the linear portion of the stress - strain diagram: the linear portion of the loading path for austenite and the linear portion of unloading path for martensite. Finally the characteristic transformation stresses were obtained from the stress-strain diagrams following the method shown in the Figure 2.5 as defined by Maletta and Furgiuele [3].

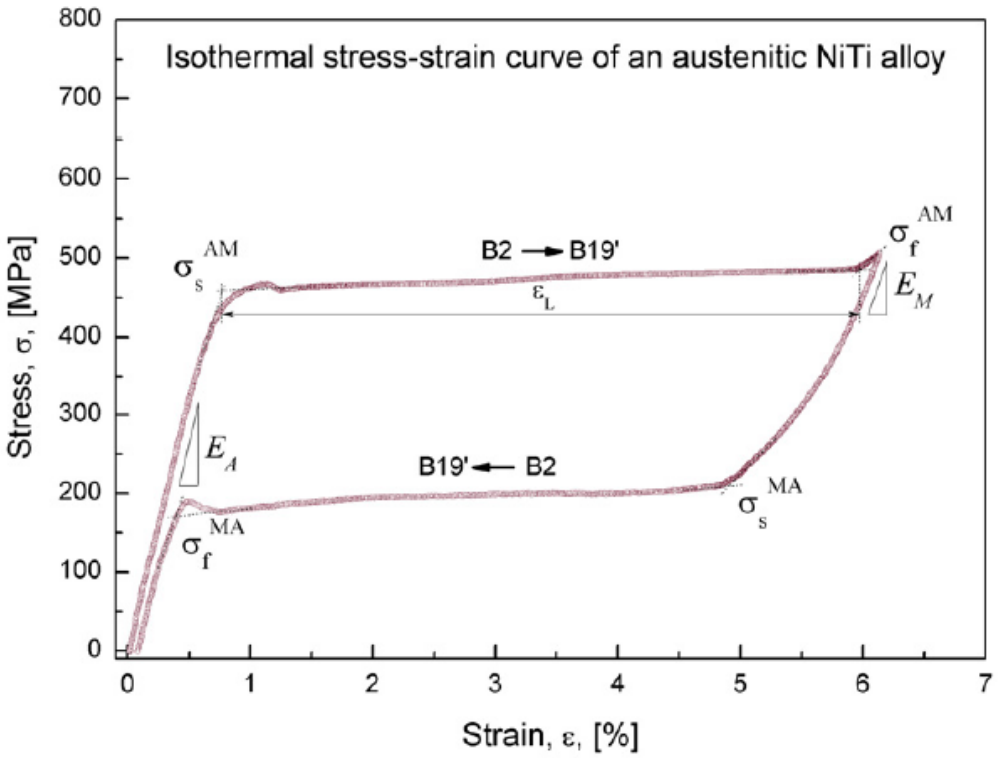


Figure 2.5. Stress-Strain Curve of NiTi Alloy Illustrating the Transformation Stresses, Young's Moduli of Austenite, E_A, and Martensite, E_M [3].

2.2.1. Tensile Test Set-up

Tensile tests were done using INSTRON-8801 hydraulic machine with a 10 kN load cell. The machine works with a controller connected to a computer which is used to control the test procedure with Bluehill software. The strain data were collected with video extensiometer and the stress was obtained from the movement of the testing machine's cross-head. A thermal camera (Optris PI450 with a measurement speed of 80 Hz) was added to the test set-up to acquire the stress induced temperature change of the specimen. For tensile tests at different temperatures, the test specimens were heated using a hot air gun. In addition, to obtain the strain maps of the tension specimens, photos for digital image correlation (DIC) method were taken simultaneously during the tests using a high speed camera. The test set-up is displayed at the Figure 2.6.

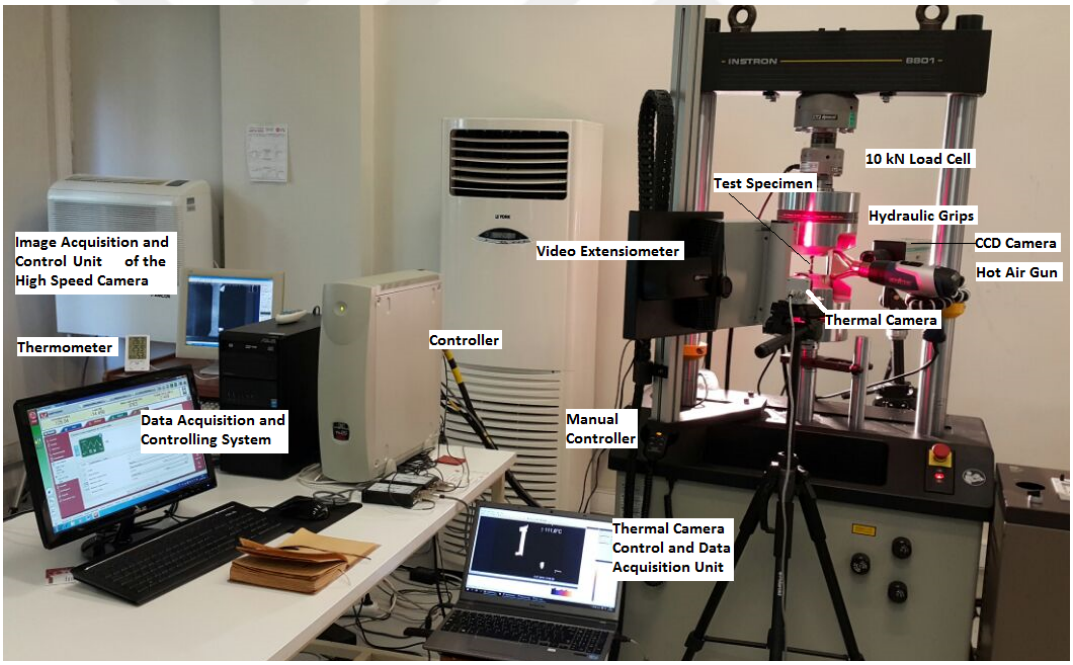


Figure 2.6. Tensile Test Set-up.

Test procedure following the ASTM F2516 - 14 standard as the basis, was defined to the Bluehill software and the stress, strain, displacement and load data with time increment were obtained as well as the temperature-time data and the DIC images. Before the tests, time synchronization of the high speed camera controlling units with the thermal camera and the test controlling unit was done. Temperature of the lab-

oratory was measured as 26 ±0.5 °C, which is higher than the austenite finish (A_f) temperature and indicates that the material is at fully austenitic phase at the beginning of the test.

2.2.2. Tensile Test Results at Room Temperature

Tensile tests were conducted at the room temperature of 26 °C, which is higher than the austenite finish temperature (A_f = 24.8° C), under displacement control at five different loading rates and repeated twice for each loading rate for repeatability purpose. The specimens were loaded to 8% strain and then unloaded to 7 MPa stress value to obtain the hysteresis loop. Using this hysteresis loop which is basically the stress-strain diagram of the material, Young's modulus of austenite and martensite and upper and lower plateau strengths were obtained. Below, Figure 2.7 shows the stress-strain diagrams of the NiTi SMA material for the loading rates used in this study.

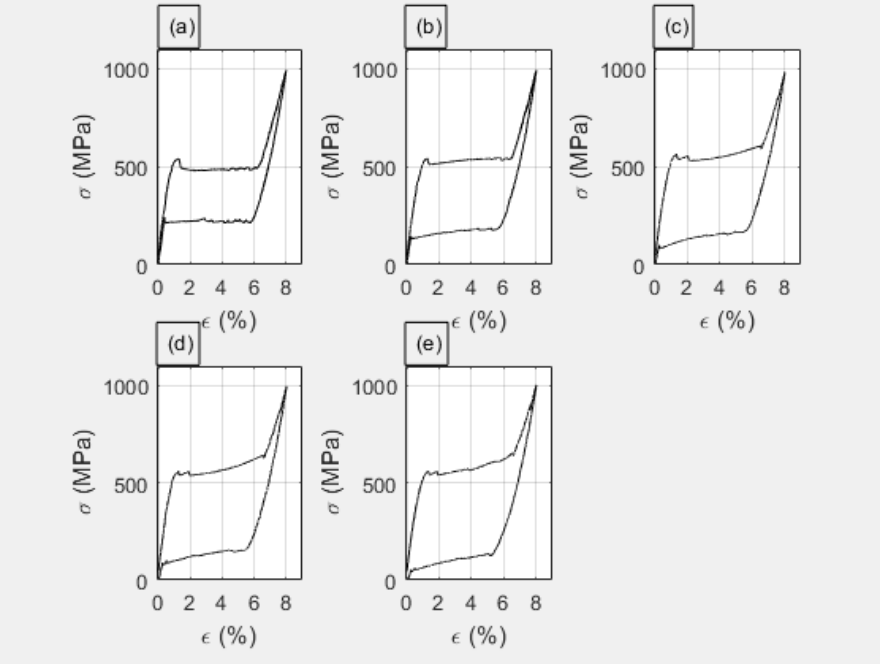


Figure 2.7. Stress-Strain Diagrams Obtained From Tensile Tests Conducted at Room Temperature of 26 °C For Loading Rates of (a) 0.1 mm/min, (b) 0.5 mm/min, (c) 1 mm/min, (d) 1.5 mm/min, (e) 2 mm/min.

As it can be seen from the stress-strain diagrams, the loading rate affects the hysteresis loop. The hysteresis area expands due to increasing loading rate, which is consistent with previous studies [42,43]. To clearly see this change, stress-strain curves at different loading rates were plotted on the same graph in Figure 2.8.

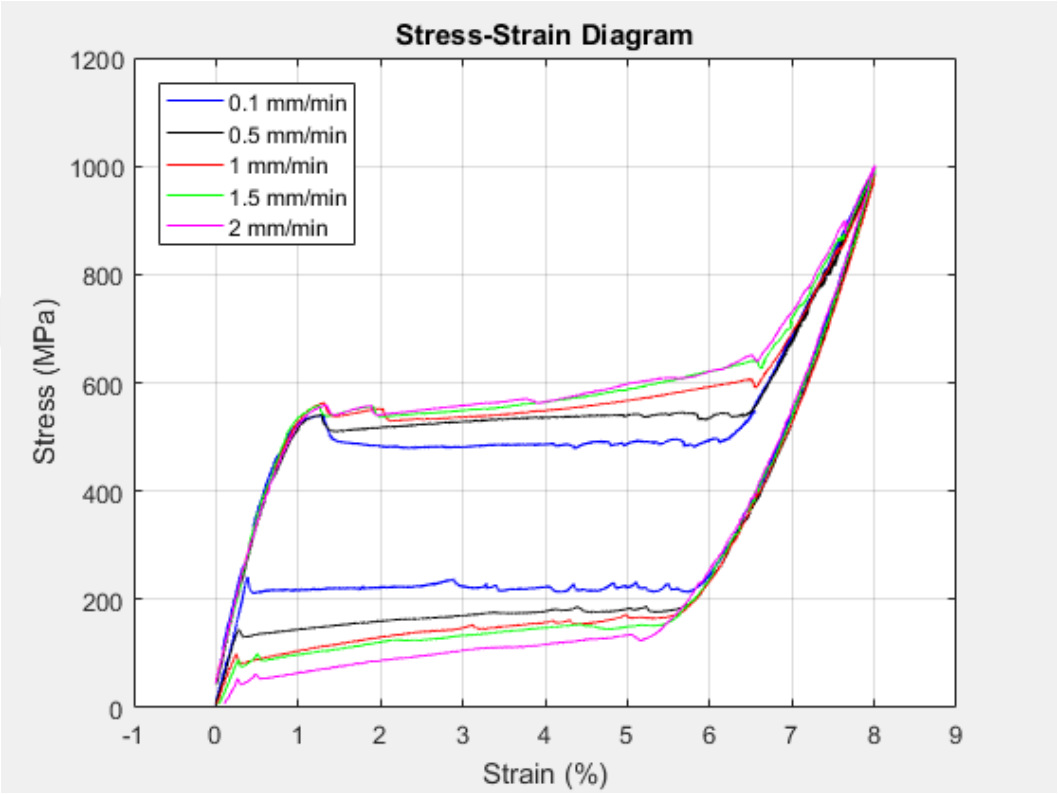


Figure 2.8. Stress-Strain Diagrams For Different Loading Rates Obtained From Tensile Tests Conducted at Room Temperature (26 °C).

The stress-strain curves were used to calculate the mechanical properties of NiTi. UPS (upper plateau strength) is the stress value that corresponds to 3% strain during forward transformation (A $\rightarrow$ M), and LPS (lower plateau strength) corresponds to 2.5% strain during reverse transformation (M $\rightarrow$ A). Young's modulus of austenite (E_A) was found from the linear portion of the loading path and that of martensite (E_M), from the linear portion of the unloading path. The units of Young's moduli are in GPa while the UPS and LPS values are MPa. The values obtained from the tensile tests are tabulated at Table 2.2.

Table 2.2. Mechanical properties of NiTi obtained from tensile tests conducted at room temperature of 26 °C for different loading rates.

Loading Rate		E_A(GPa)	E_M (GPa)	UPS(MPa)	LPS(MPa)
$5 \times 10^{-5}\, 1/s$	0.1 mm/min	62 ± 1	45 ± 1	481	225
$2.6 \times 10^{-4}\, 1/s$	0.5 mm/min	62 ± 1	45 ± 1	528	165
$5.2 \times 10^{-4}\, 1/s$	1 mm/min	62 ± 1	45 ± 1	537	141
$7.8 \times 10^{-4}\, 1/s$	1.5 mm/min	62 ± 1	45 ± 1	549	125
$1 \times 10^{-3}\, 1/s$	2 mm/min	62 ± 1	45 ± 1	559	96

From the data in Figure 2.2, it can be seen that the Young's modulus of austenite is higher than the Young's modulus of martensite . There are prior studies representing this difference in the elastic moduli of austenite and martensite [17, 29].

What is interesting in this data is that due to increasing loading rate, there is a distinct increase in the upper plateau strength (UPS), and a decrease in the lower plateau strength (LPS) of the material. These results are consistent with those of other studies who found similar results [33, 54]. Due to the thermomechanical capabilities of NiTi, there occurs a temperature increase during the forward transformation and a decrease during the reverse transformation and these temperature changes affect the materials transformation stresses since they are linear functions of each other as proposed by Tanaka *et al.* [5].

2.2.2.1. Transformation Stresses. As noted before, transformation stresses are obtained from the stress - strain curves for each experiment conducted at different loading rates following the method proposed by Maletta and Furgiuele [3]. Transformation stresses are found from the intersection points of the linear portions of the curve with the loading [unloading] plateau as illustrated at Figure 2.5. Table 2.3 provides the phase transformation stresses obtained using this method.

Table 2.3. Transformation stresses of NiTi obtained from tensile tests conducted at room temperature of 26 °C for different loading rates.

Loading Rate		σ_{MS} (MPa)	σ_{MF} (MPa)	σ_{AS} (MPa)	σ_{AF} (MPa)
$5 \times 10^{-5}\, 1/s$	0.1mm/min	470	495	220	216
$2.6 \times 10^{-4}\, 1/s$	0.5 mm/min	501	549	184	139
$5.2 \times 10^{-4}\, 1/s$	1 mm/min	511	608	167	80
$7.8 \times 10^{-4}\, 1/s$	1.5 mm/min	514	646	160	78
$1 \times 10^{-3}\, 1/s$	2 mm/min	523	684	156	43

The present findings seem to be consistent with other research which found that martensite start (σ_{MS}) and finish (σ_{MF}) stresses increase, while austenite start (σ_{AS}) and finish (σ_{AF}) stresses decrease with increasing loading rates [38, 43]. These findings can be explained with thermomechanical coupling. Due to stress induced transformation, there occurs latent heat generation since forward transformation (M $\rightarrow$ A) is an exothermic reaction. When the loading rate is high the specimen does not have enough time to release this heat to the environment. This heat increase of the specimen causes the forward transformation plateau to shift upwards, hence the transformation stresses increase. At the same time, during reverse transformation which is an endothermic reaction, the specimen temperature decreases below the room temperature and does not have enough time for increasing it's temperature by absorbing heat from the environment. This decrease of the specimen temperature results in the shift of the reverse transformation plateau downwards. As a consequence, the reverse transformation stresses decrease.

2.2.3. Tensile Tests at Ambient Temperature Lower Than A_f

To show the effect of the ambient temperature on the mechanical properties of NiTi SMA during experiments, series of tensile tests were conducted at 20 °C ambient temperature which is lower than the austenite finish temperature of $A_f = 24.8$°C.

Since the environment temperature is below A_f, it is apparently not at fully austenitic phase and contains some martensite in itself. All the experiments were done using the same method explained previously at ASTM F2516 - 14. But the specimen is loaded up to 8% strain to ensure the stress induced transformation to full martensite and the ambient temperature is different from the previous experiments. Using the stress - strain curves, E_A, E_M and UPS, LPS were obtained with the method mentioned before. Below, Figure 2.9 presents the stress - strain curves at the ambient temperature of 20 °C for the same loading rates.

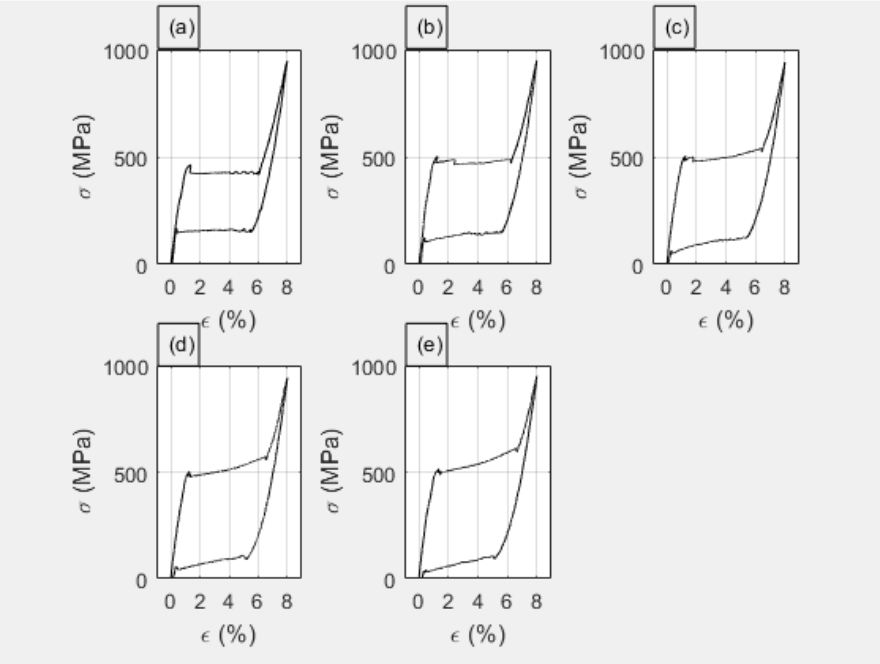


Figure 2.9. Stress-Strain Diagrams Obtained From Tensile Tests Conducted at Ambient Temperature of 20 °C For Loading Rates of (a) 0.1 mm/min, (b) 0.5 mm/min, (c) 1 mm/min, (d) 1.5 mm/min, (e) 2 mm/min.

Apparently, even if the specimen is at an ambient temperature which is lower than A_f and not fully austenitic at the beginning of the experiment, still, the hysteresis area expands with increasing loading rate. To see this expansion clearly, stress - strain curves were plotted on the same graph as before, which is illustrated at Figure 2.10.

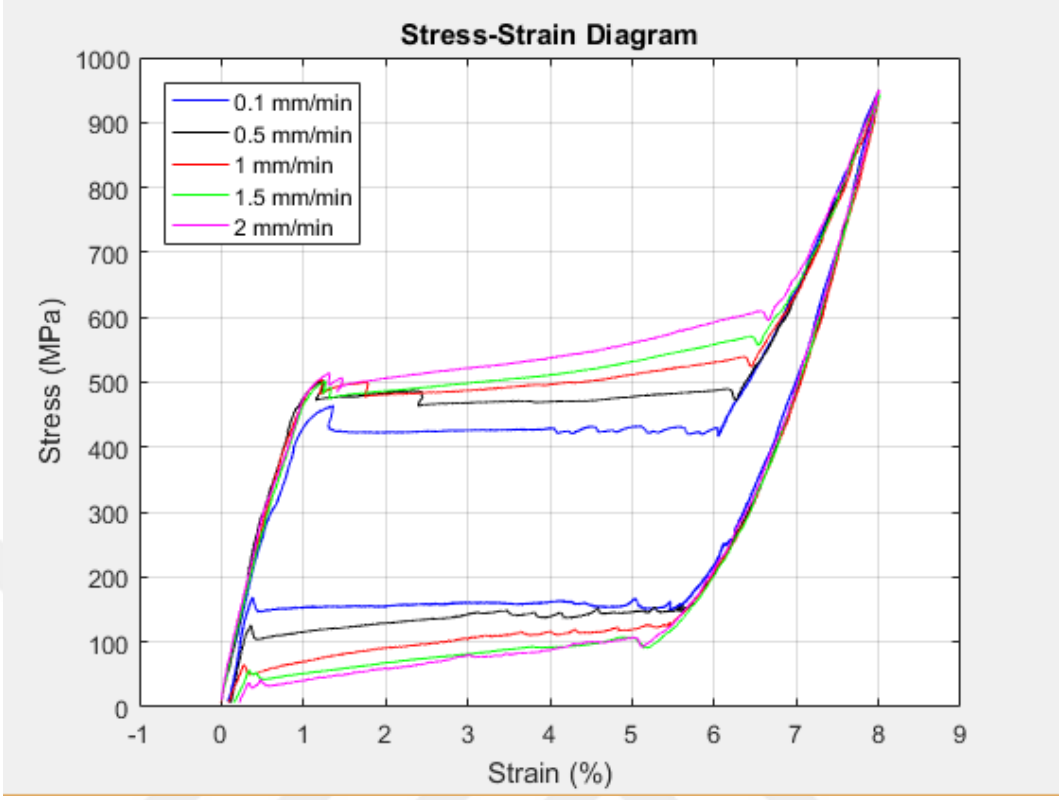


Figure 2.10. Stress-Strain Diagrams For Different Loading Rates Obtained From Tensile Tests Conducted at Ambient Temperature of 20 °C.

It is clear that the upper plateau strengths (UPS) increase while the lower plateau strengths (LPS) decrease with the increase at the loading rate. The same trend for the Young's moduli of austenite and martensite is seen. E_A is higher than that of the E_M value. But the obtained E_A results are considerably lower than the values of the ones obtained from the tests conducted at the room temperature of 26 °C, while E_M values are slightly higher than the previous tests conducted at room temperature of 26 °C. The results measured from the stress - strain curves are presented in Table 2.4.

Transformation stresses for the experiments conducted at the ambient temperature of 20 °C were obtained using the same method as before. Again, increasing transformation stress values for the forward transformation and decreasing transformation stress values for the reverse transformation were obtained. But the values are considerably lower than that of the experiments conducted at 26 °C ambient temper-

Table 2.4. Mechanical properties of NiTi obtained from tensile tests conducted at ambient temperature of 20 °C for different loading rates.

Loading Rate		E_A(GPa)	E_M (GPa)	UPS (MPa)	LPS (MPa)
$5 \times 10^{-5}\, 1/s$	0.1 mm/min	55 ± 3	46 ± 1	426	158
$2.6 \times 10^{-4}\, 1/s$	0.5mm/min	55 ± 3	46 ± 1	469	135
$5.2 \times 10^{-4}\, 1/s$	1mm/min	55 ± 3	46 ± 1	488	98
$7.8 \times 10^{-4}\, 1/s$	1.5 mm/min	55 ± 3	46 ± 1	499	75
$1 \times 10^{-3}\, 1/s$	2mm/min	55 ± 3	46 ± 1	521	68

ature. The measured transformation stresses are shown in Table 2.5.

Table 2.5. Transformation stresses of NiTi obtained from tensile tests conducted at ambient temperature of 20 °C for different loading rates.

Loading Rate		σ_{MS} (MPa)	σ_{MF} (MPa)	σ_{AS} (MPa)	σ_{AF} (MPa)
$5 \times 10^{-5}\, 1/s$	0.1 mm/min	420	430	155	149
$2.6 \times 10^{-4}\, 1/s$	0.5mm/min	470	492	147	107
$5.2 \times 10^{-4}\, 1/s$	1 mm/min	489	547	136	58
$7.8 \times 10^{-4}\, 1/s$	1.5mm/min	494	578	127	41
$1 \times 10^{-3}\, 1/s$	2mm/min	500	617	125	29

These findings are in compliance with the previous tests. Forward transformation stresses increase and the reverse transformation stresses decrease with increasing loading rates, as well. It seems that ambient temperature change only effects the amplitudes of the mechanical properties, not their thermomechanical coupling mechanisms.

2.3. Temperature Effect on Transformation Stresses

Tensile tests were conducted over a temperature range of 30 °C to 100 °C with an increment of 10 °C to see the effect of temperature. For each test a new sample was used to avoid the effect of training on the specimen. In this temperature range, all samples were loaded up to an 8% strain and then unloaded back to 7 MPa; all showed superelastic (SE) behavior. In the last experiment however, which was performed at 100 °C, the sample fractured before reaching 8 % strain. Resulting stress - strain curves are illustrated in Figure 2.11.

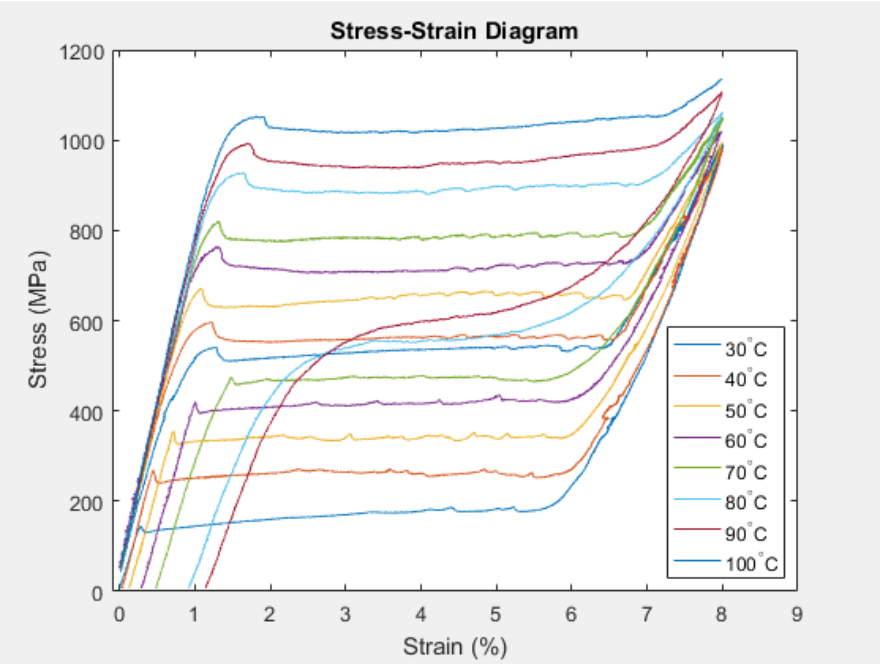


Figure 2.11. Stress - Strain Curves Obtained From Tensile Tests Conducted at Different Testing Temperatures.

Increasing testing temperature affects the transformation stress and the plateau strength. Increasing testing temperatures cause both forward and reverse transformation stresses of the material to increase. Forward transformation (A $\rightarrow$ M) starts later and reverse transformation starts earlier when compared to lower temperatures; because austenite is more stable at higher temperatures. This phenomenon was reported by previous studies [73]. Table 2.6 shows the measured transformation stresses in this study from the stress - strain curves of tensile tests conducted at different testing

temperatures.

Table 2.6. Transformation stresses of NiTi, from tensile tests conducted at different testing temperatures.

Testing Temperature	σ_{MS} **(MPa)**	σ_{MF} **(MPa)**	σ_{AS} **(MPa)**	σ_{AF} **(MPa)**
30 °C	500	549	183	137
40 °C	545	565	254	241
50 °C	636	657	349	327
60 °C	699	729	426	399
70 °C	774	793	465	459
80 °C	880	905	575	541
90 °C	931	984	649	554
100 °C	1005	1051	-	-

These data are used to obtain Clausius - Clapeyron constants C_A and C_M, in Clausius - Clapeyron equation, which gives the relation between temperature and transformation stresses. The forward and reverse transformation stresses of NiTi can be approximately found as a linear function of temperature for uniaxial loading [74]. The relation of the transformation stress of the specimen to temperature is important. Because the increase in the forward transformation stress is actually caused by the trapped heat inside the material that does not have time for heat loss with increasing loading rate. For this reason, once the temperature of the specimen is known, transformation stresses can be calculated using the relation between stress and temperature with Clausius - Clapeyron constant. Clausius - Clapeyron constants are different for forward and reverse transformations. C_M is the constant that corresponds to the forward transformation stress and C_A is the constant that corresponds to the reverse transformation stress [4, 54].

Clausius - Clapeyron constants which are the slopes of the A $\rightarrow$ M transformation stress - temperature and M $\rightarrow$ A transformation stress - temperature lines were

obtained from the stress - temperature diagram illustrated below at Figure 2.12. They were approximately calculated as C_M=9.6 MPa / °C and C_A=7.9 MPa / °C.

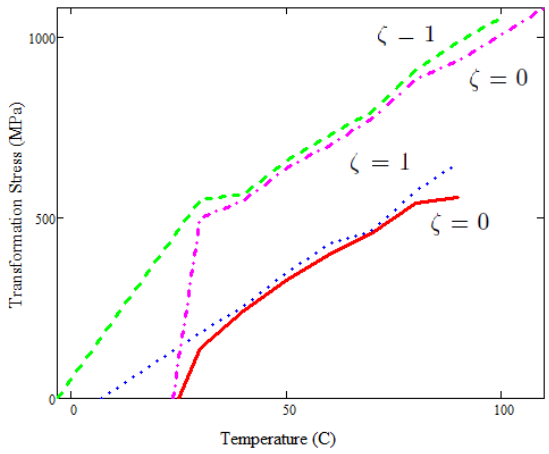


Figure 2.12. Stress - Temperature Phase Diagram of NiTi Obtained From Tensile Tests Conducted at Different Testing Temperatures.

Falvo *et al.* [4] conducted tensile tests in a temperature range of 25 K between 303 K and 328 K in which $A_f < 303K$. They used the results of their experiments to measure Clausius - Clapeyron constants, C^{AM} and C^{MA}, respectively and defined as:

$$\frac{d\sigma}{dT} = C. \tag{2.1}$$

Then, they proposed the following equations to calculate the critical stress values:

$$\sigma_s^{AM} = \sigma_{s0}^{AM} + C^{AM}(T - T_0), \tag{2.2}$$

$$\sigma_f^{AM} = \sigma_{f0}^{AM} + C^{AM}(T - T_0), \tag{2.3}$$

$$\sigma_s^{MA} = \sigma_{s0}^{MA} + C^{MA}(T - T_0), \tag{2.4}$$

$$\sigma_f^{MA} = \sigma_{f0}^{MA} + C^{MA}(T - T_0) \tag{2.5}$$

where σ_s^{AM} is the martensite transformation start stress, σ_f^{AM} is the martensite transformation finish stress, σ_s^{MA} is the austenite transformation start stress and σ^{MA} is the austenite transformation finish stress. The quantities with the subscript 0 state the

parameters measured at 303 K.

If Equations 2.2, 2.3, 2.4 and 2.5 are implemented to the results of the present study obtained from the tensile tests conducted at different testing temperatures, C_A and C_M can be calculated and the resulting stress - temperature diagram can be plotted. Clausius - Clapeyron constants in a temperature range of 60 °C between 30 °C and 90 °C, $C_A = 6.95$ and $C_M = 7.3$ were found for $\zeta = 0$ and $\zeta = 1$ lines as shown in Figure 2.12. Resulting stress - temperature graph plotted using equations proposed by Falvo *et al.* [4] is given in Figure 2.13.

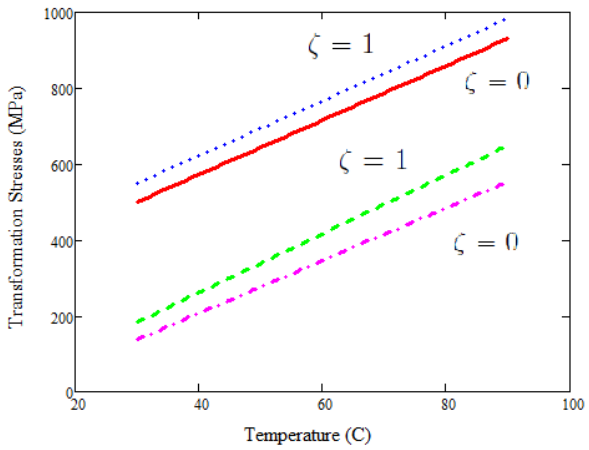


Figure 2.13. Stress - Temperature Phase Diagram Plotted Using Equations Proposed by Falvo *et al.* [4] and Data of Present Study.

C_A and C_M calculated using equations proposed by Falvo *et al.* [4] are not in good agreement with the results obtained in the current study. This is thought to be due to neglecting the transformation temperatures obtained with DSC which gives transformation temperatures at 0 stress. If the temperatures obtained from DSC are omitted from the stress - temperature diagram presented in Figure 2.12, then relatively close values can be obtained which are $C_A = 7.1$ and $C_M = 7.6$.

Tanaka *et al.* [5], used the transformation kinetics represented by Koistinen and Marburger [75] and Wang and Inoue [76] and obtained the transformation equation as follows:

$$\xi = 1 - exp[{}_{M}a(M_s - \theta) +_{M} \tilde{b}K] \tag{2.6}$$

where ξ is the martensite volume fraction, K is the uniaxial stress and

$${}_{M}a = -2ln10/(M_s - M_f) \tag{2.7}$$

and obtained the following equations for forward transformation start and finish lines as functions of temperature:

$$K \geq ({}_{M}a/{}_{M}\tilde{b})(\theta - M_s), \tag{2.8}$$

$$K = -2ln10/{}_{M}\tilde{b} + ({}_{M}a/{}_{A}\tilde{b})(\theta - M_s). \tag{2.9}$$

The same approach for the reverse transformation was used and the following equations were obtained:

$$1 - \xi = 1 - exp[{}_{A}a(A_s - \theta) +_{M} \tilde{b}K], \tag{2.10}$$

$$K \leq -({}_{A}a/{}_{A}\tilde{b})(\theta - A_s), \tag{2.11}$$

$$K = -2ln10/{}_{A}\tilde{b} + ({}_{A}a/{}_{A}\tilde{b})(\theta - A_s) \tag{2.12}$$

where ${}_{A}a$ is defined as:

$${}_{A}a = 2ln10/(A_f - A_s). \tag{2.13}$$

Next, a new set of calculations were done using Equations 2.8, 2.9, 2.11 and 2.12 and the $C_A = 9.6$ and $C_M = 7.9$ (the experimentally obtained stress temperature lines' slopes from the present study), the transformation lines were plotted with MATHCAD as shown in Figure 2.14:

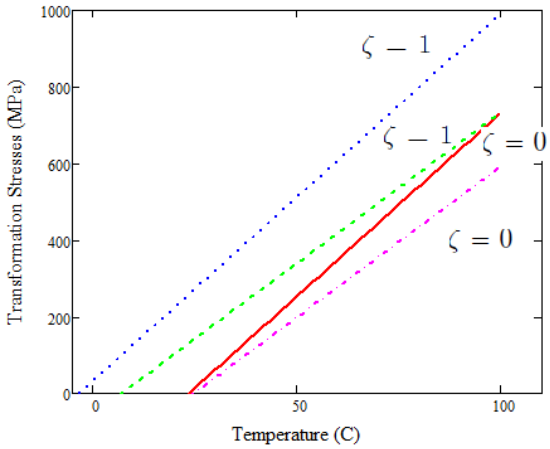


Figure 2.14. Stress - Temperature Phase Diagram Plotted Using the Equations Proposed by Tanaka *et al.* [5].

The regions in Figure 2.14 between the forward and the reverse transformation lines were called the transformation strips by Tanaka *et al.* [5]. These transformation strip widths were found to be constant (lines are parallel) for all three cases. But the equations proposed by Tanaka *et al.* [5] give a larger width for the forward transformation in comparison to the other two (reverse transformation). The lower forward transformation start stresses are not in good agreement with the experimental results as a result of this. Comparing the two method proposed by Tanaka *et al.* [5] and Falvo *et al.* [4] with the experimental results, it was observed that the experimental results performed in this study are in a better agreement with the method of Falvo *et al.* [4] However, the equations from Falvo *et al.* [4] do not take the transformation stresses at zero stress into account, which may result in a misevaluation of the material phases at a known temperature. It can be concluded that, the Tanaka *et al.*'s [5] method is better for determining the material phase at lower temperatures, and the method proposed by Falvo *et al.* [4] is better for determining the transformation stresses at higher temperatures.

3. EVALUATION OF FRACTURE PARAMETERS

3.1. Introduction

Fracture behavior of engineering materials is an important issue to be considered for design. If the load applied to a material is high, even if the average stress value on the material is lower than the critical value for failure, in presence of sharp cracks, stresses at the crack tip will increase and finally will cause the material to fracture. Since almost every material has crack like defects, it is important to make the design including fracture mechanics criterion.

A widely used method to calculate the strain energy release rate for linear elastic materials is the use of so called J contour integral. J-integral is a contour independent parameter for linearly elastic homogeneous materials in the case of a uniformly distributed temperature, and is equal to the energy release rate G [77]. Strain energy release rate, is used for calculating the stress field of linearly elastic homogeneous materials. In the case of non linear materials it was proposed by Rice and Rosengren [77] that J-integral can be used to determine the stress field inside a small region around the crack tip [78].

Crack Tip Opening Displacement (CTOD) is another parameter that can be used as a fracture criterion. CTOD describes the crack tip conditions in elastic plastic materials. Nearly size independent fracture toughness of a cracked material can be measured using CTOD's critical values even in the case of large crack-tip plasticity cases [6].

Based on the linear elastic fracture mechanics theory, a quantity known as stress intensity factor, denoted by K is defined. A material's resistance capacity to fracture is measured by it's critical stress intensity factor, K_C, which is called the fracture toughness. K is a function of the applied remote stress and the crack length, and has the unit of MPa$\sqrt{m}$, as seen below:

$$K = Y\sigma\sqrt{\pi a} \tag{3.1}$$

Here, σ is the remotely applied stress, a is the crack length and Y is a dimensionless constant that changes with geometry and the mode of loading.

Stress intensity factor is usually shown with a subscript that corresponds to the mode of the loading. There are three loading modes of a crack which are K_I, K_{II} and K_{III} and described as Mode I the opening mode, Mode II the sliding mode and Mode III the tearing mode, respectively. In the present study, only Mode I loading is studied since it is the most encountered fracture failure. Below, Figure 3.1 illustrates these loading modes.

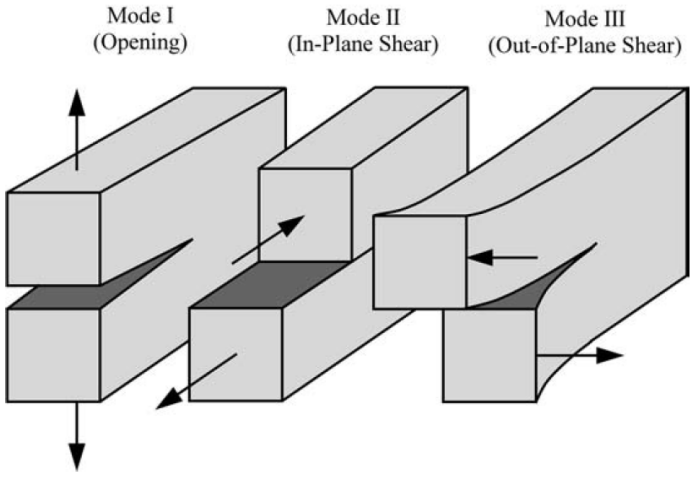


Figure 3.1. The Basic Modes of Loading. [6].

Stress intensity factor is the parameter that defines the magnitude of the stresses around a crack tip that are singular as the crack tip is reached. If a polar coordinate system as seen in Figure 3.2 is defined at the tip of a crack under Mode I loading, the stresses for a linear elastic, isotropic material can be calculated as follows:

$$\sigma_{xx} = \frac{K_I}{\sqrt{2\pi r}} cos\frac{\theta}{2}\left[1 - sin\frac{\theta}{2}sin\frac{3\theta}{2}\right] + \underbrace{.....}_{\text{H.O.T}} \tag{3.2}$$

$$\sigma_{yy} = \frac{K_I}{\sqrt{2\pi r}} cos\frac{\theta}{2}\left[1 + sin\frac{\theta}{2}sin\frac{3\theta}{2}\right] + ... \tag{3.3}$$

$$\sigma_{xy} = \frac{K_I}{\sqrt{2\pi r}} cos\frac{\theta}{2}sin\frac{\theta}{2}cos\frac{3\theta}{2} + ... \tag{3.4}$$

$$\sigma_{zz} = 0 \qquad \text{(Plane Stress)} \tag{3.5}$$

$$\sigma_{zz} = \nu(\sigma_{xx} + \sigma_{yy}) \qquad \text{(Plane Strain)} \tag{3.6}$$

$$\tau_{xz} = \tau_{yz} = 0 \tag{3.7}$$

Higher order terms in these equations are ignored due to an decrease in stress amplitudes as r $\rightarrow$ 0. As r approaches zero, stresses all tend to infinity, with a mathematical singularity which is known as the $\frac{1}{\sqrt{r}}$ singularity [79]. Thus stress components at the crack tip can not be calculated exactly in the case of a real material.

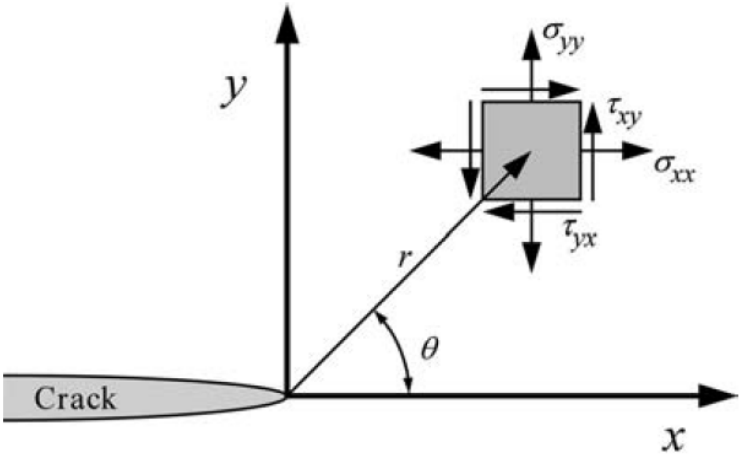


Figure 3.2. Illustration of the Coordinate System at the Crack Tip [6].

Implementing the critical stress intensity factor K_{IC} to the stress equations gives the maximum stress before fracture. K_{IC}, the fracture toughness, is an important material parameter for material design.

NiTi undergoes phase change upon loading, therefore the material parameters change. Due to phase change, calculation of K_{IC} is not easy at the crack tip and the LEFM method can not be implemented to get exact results the way it is used for

conventional materials. The effect of phase transformation and therefore the transformation region on evaluation of fracture parameters should be studied. For this reason, in this chapter obtaining fracture parameters using the ASTM E399 and DIC technique is studied in detail.

3.2. The Effect of Loading Rate on Fracture Parameters

NiTi SMA goes under immediate phase change from austenite to martensite even with small loadings, around a sharp crack tip [71]. It was reported before that this transformation to martensite through stress induced martensitic (SIM) transformation increases the fracture toughness of NiTi for loading conditions of Mode I and mixed mode (Mode I/II) [13, 17, 26, 80].

In a previous work of Jiang and Vecchio [70] it is reported that the fracture toughness of NiTi SMA increases with increasing loading rate. This findings shows that on the case of a dynamic loading rate, NiTi SMA shows a higher fracture toughness, but there is still a need to see the effect of the loading rate on quasi-static loading conditions since loading rates may not always change in high amplitudes. For this reason, in this work, for better understanding of the fracture behavior of NiTi SMA, fracture toughness tests were conducted under different quasi-static loading conditions.

3.3. Implementation of DIC Method to Fracture Experiments

For implementation of the DIC method to fracture tests, images of the specimen surface were taken using a high speed camera during the K_{Ic} fracture experiments conducted on a compact tension specimen. Using this images displacement measurements were obtained by correlating the pattern of the undeformed specimen surface image to the image that was taken just before the time of fracture.

Obtained displacement field data on y-direction were used to curve fit to the Equation 3.8 below which was proposed by Oral *et al.* [81] using a Matlab code for numerical implementation and the fracture parameters were calculated.

$$u_y = \underbrace{\frac{K_I}{2\mu_{tip}}\left(\frac{r}{2\pi}\right)^{\frac{1}{2}} sin\frac{\theta}{2}\left(\frac{3-\nu_{tip}}{1+\nu_{tip}} - cos\theta\right) - \frac{T\nu_{tip}}{2\mu_{tip}(1+\nu_{tip})} r sin\theta}_{\text{Mode I loading}}$$
$$+ \underbrace{\frac{K_{II}}{4\mu_{tip}}\left(\frac{r}{2\pi}\right)^{\frac{1}{2}}\left(\frac{5\nu_{tip}-3}{1+\nu_{tip}} cos\frac{\theta}{2} - cos\frac{3\theta}{2}\right)}_{\text{Mode II loading}} + \underbrace{A_1 r cos\theta + u_{0y}}_{R.B.} \tag{3.8}$$

In this equation, T denotes the stress component parallel to the crack plane, A_1 is rigid body rotation and u_{0y} denotes the rigid body displacement. Also ν_{tip} is Poisson's ratio and μ_{tip} is the shear modulus at the crack tip. From this equation K_I, K_{II}, T, A_1 and u_{0y} can be calculated. For the first round of the calculations done using Matlab for numerical implementation, all five parameters were calculated. But since the specimen used for experiments only has an edge crack which is under Mode I loading condition, K_{II} values were calculated as very small values, as already expected. So for the second round of the calculations the K_{II} term was removed from Equation 3.8 and new calculations were made only for the remaining parameters. The new calculations did not show any significant difference for K_I, T, A_1 and u_{0y} values.

3.4. Fracture Experiments

3.4.1. Fracture Test Setup

Fracture tests were also done using INSTRON-8801 hydraulic machine with a 10 kN load cell using proper grips for the compact tension (CT) specimen. Test procedure was controlled with KIC Fracture Toughness software. The room temperature was measured as 26 ±0.5°C. Since the surface temperature of the specimen during the test is important as well as the room temperature, a thermal camera (Optris PI450 with a measurement speed of 80 Hz) was used. Acquisition of the DIC images were done using a CCD camera connected to a computer. The camera is Dantec Dynamics Nanosense MKIII Q450 IDT 1000 Hz Nikon 50 mm which has a resolution of 5 mega-pixels, with Edmund Optics 63729 0.5×110 mm lens. Also a COD gage was used to measure the crack tip opening displacement since the experiments were conducted

under displacement control. The test setup is presented at Figure 3.3.

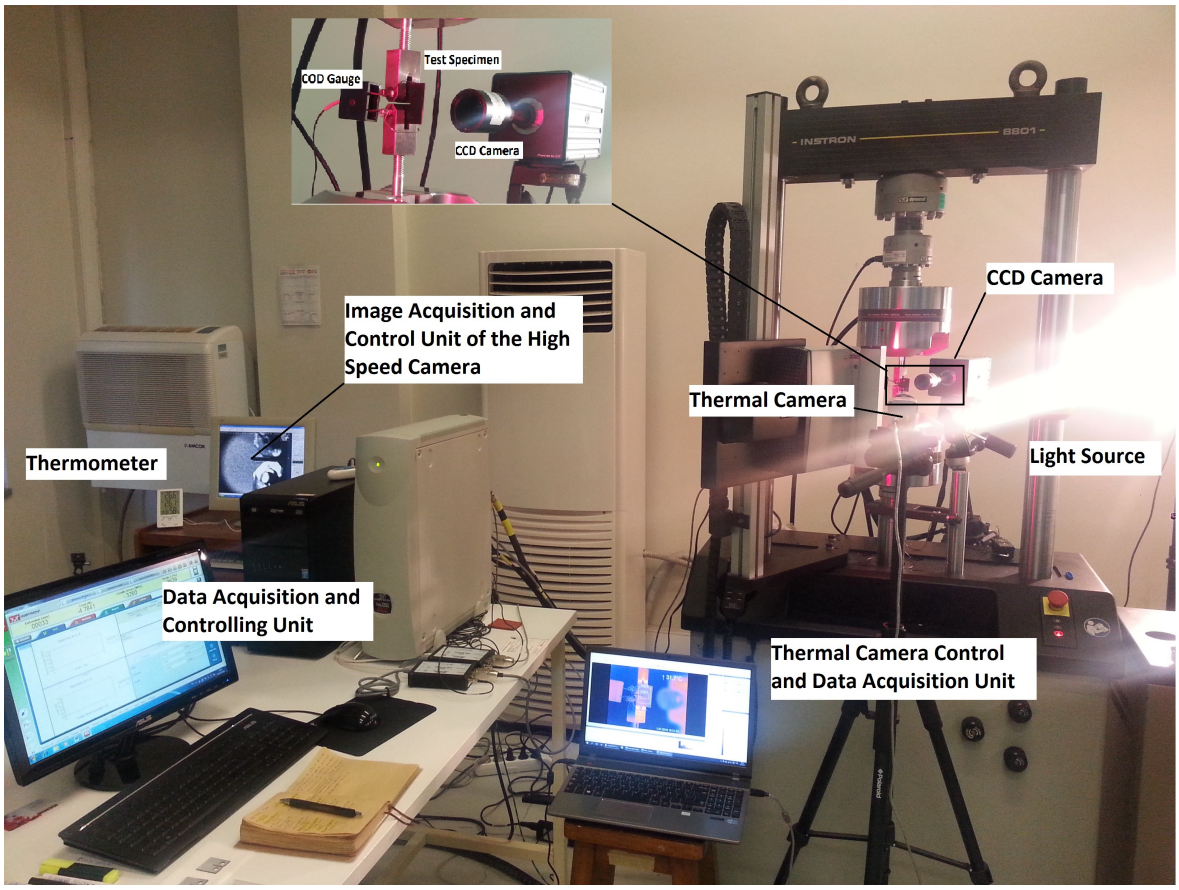


Figure 3.3. Fracture Test Set-up.

The samples for the fracture tests were cut along the rolling direction (RD) using electrical discharge machining (EDM). Dimensions were adapted from the standard ASTM E399-12 (Standard Test Method for Linear-Elastic Plane-Strain Fracture Toughness K_{Ic} of Metallic Materials) [8]. Figure 3.4 presents the drawing and the photo of the test specimen.

3.4.2. Fracture Test Procedure

The test procedure the computer software follows is ASTM E399 standard. ASTM E399 is actually for plane-strain but our specimen was under plane-stress condition. For this reason, even if the guideline for the tests were taken from this standard, only the load-displacement data from the test are used to find the maximum load and dis-

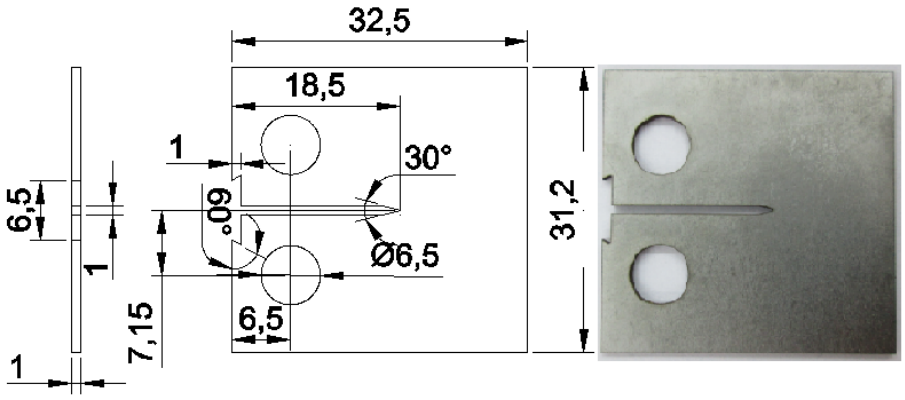


Figure 3.4. Dimensions of NiTi Fracture Test Specimen in mm.

placement values for fracture toughness calculations.

For the fracture toughness testing of CT specimens, a fatigue precrack is needed as suggested at the standard. The specified crack size at the standard is defined to be in the range of 0.45 W to 0.55 W and crack size a is the total size of the machined notch and the fatigue crack. Here W is the specimen width. a and W both are measured from the centerline of the loading holes [8].

To obtain the appropriate precrack, fatigue tests were conducted using Instron - 8801 hydraulic testing machine with a 10 kN load cell and the Wavematrix computer software. Before starting the fatigue tests, the specimens were grinded and then polished. This procedure has two purpose. First one is that the propagation of the precrack is easier to be observed from the high speed camera on a polished surface and the second one is that since the fatigue precrack is very small, it can not be measured macroscopically and the precrack length on a polished surface can be measured more accurately with a microscope.

Fatigue precrack tests were done under force control. Fatigue cycling was done with a sinusoidal waveform in the load range of 0 N to 250 N. A frequency of 1 Hz with a total of 5000 cycles were used for the tests. Then the specimen was located to the grips. But the grips for compact tension specimens of the testing machine are wider

than the thickness of the sample, thus brass bushes were used for avoiding any out of plane movement so that a Mode I precrack can be obtained. Figure 3.5 presents the fracture specimen grips with brass bushes.

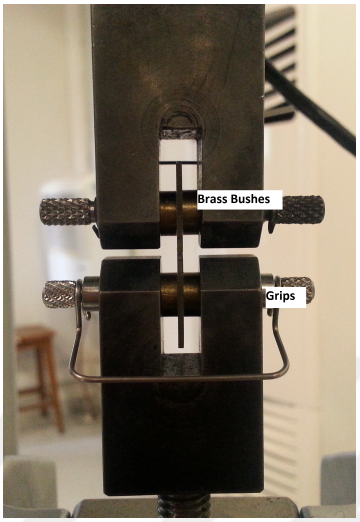


Figure 3.5. Compact Tension Specimen Grips With Brass Bushes.

Exact measurement of the precrack sizes were done using the Olympus 100AL optical microscopy. Even though all the fatigue precrack tests were done under the same conditions, different precrack sizes were obtained for each specimen. But still they are in the range of 0.45 W to 0.55 W, as defined by ASTM E399 standard.

After obtaining fatigue precracks, the specimen was painted with white matte spray paint and black speckles were sprayed to the surface with a black matte spray paint. These black speckles are used for the displacement calculations by the DIC software after the experiments. These speckles need to be as small as possible and have a non repetitive pattern. An appropriate pattern for calculations are presented in Figure 3.6.

Following the painting process of the DIC pattern, the specimens are ready to be tested. Next, specimens were located to the grips for testing. For locating of the specimen to the loading grips the brass bushes illustrated in Figure 3.5 were used again.

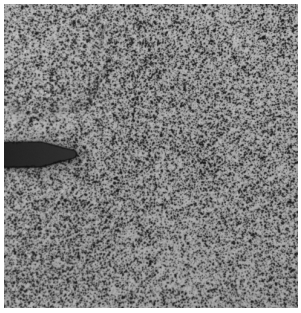


Figure 3.6. An Example DIC Pattern.

Fracture toughness tests were conducted under displacement control for the loading rates of the tensile tests of 0.1 mm/min, 0.5 mm/min, 1.5 mm/min and 2 mm/min. The previously obtained mechanical properties were used for the corresponding loading rates while writing the test method of the fracture toughness tests to the controlling computer software. Displacement control was done with a COD gauge which was placed on the knife edges on the compact tension specimen. Load - crack opening displacement (COD) data were recorded.

A light source was placed behind the camera in a way that an appropriate amount of light reflects on the pattern for a better exposure. Also the camera was placed to a proper distance from the specimen in accordance with the focus length of the lens, because the lens that was used does not have any optical or digital focus features. Before starting the test, an image of the undeformed specimen was captured using the high speed camera and deformed images were continued to be captured at every second until the end of the test upon fracture.

On the other hand, surface temperatures were measured simultaneously during the experiments from the opposite surface of the DIC pattern. To obtain high emissivity this surface was painted with a black matte spray paint. At the beginning of each test, surface temperatures were 30 $\pm 1^{\circ}$C. Surface temperature of the specimens were continued to be recorded during the test, but the camera in hand could not acquire the temperature change due to phase transformation around the crack tip, because the temperature change was too fast and this was beyond the camera's acquisition

capability.

3.4.3. Digital Image Correlation (DIC)

Digital image correlation (DIC) method is an effective way of obtaining the displacement data on the surface of a test specimen without contact. While other methods like video or dynamic extensiometers use the extension of the specimen measured between two points, with DIC method one can obtain the full field displacement data of the specimen surface.

For measurement of displacement a random , non-uniform pattern of black speckles is needed to be applied to the surface. This pattern deforms as the specimen under test deforms during loading-unloading. A high speed camera (CCD) is used to capture the images of this deformation. First an image before the test is captured to be used as the undeformed image. Then during the loading-unloading of the specimen images are continued to be captured. Since the pattern changes as the specimen is deformed, the differences between patterns of the deformed-undeformed images are calculated using a computer software with correlation of all the pixels of the undeformed image and the deformed image. With the calculated data, strain maps and full field displacement field can be obtained [39, 82].

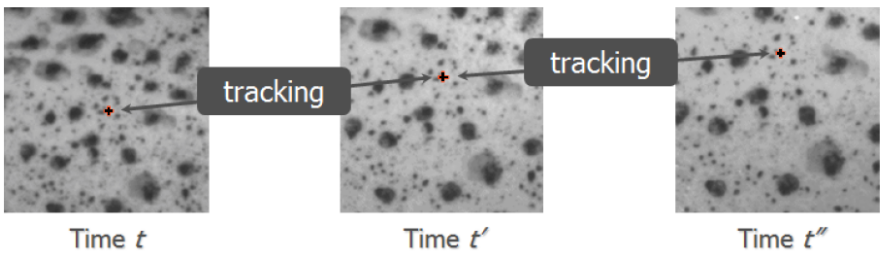


Figure 3.7. Tracking Procedure of a Particular Point Between the Undeformed Image and the Deformed Images [7].

This method is essentially consists of tracking a particular point at the reference image in the deformed image which best fits the correlation. This concept is illustrated

at Figure 3.7 above. Tracking of the point is made inside a predefined area around the reference point which is called a subset. This way it is easier to find the discrete point, because if a subset size is not defined, software might find an irrelevant point. More detailed description of the DIC technique can be found at [83, 84].

Digital Image Correlation is an advantageous technique in experimental mechanics due to it's capability of providing full field displacement and strain field data and does not require complicated tools to implement. For this reason DIC technique is widely used by researchers working on SMAs [26, 85–87].

DIC is a beneficial method for fracture mechanics as well, because accurate displacement data can be obtained without contact to the specimen and the displacement data can be used to calculate the fracture toughness of NiTi SMA. Since NiTi is not a linear elastic material, the linear elastic fracture mechanics theory does not fit to it very well. So it is assumed that calculating fracture toughness from DIC data give more accurate results. For it's benefits on calculation of fracture parameters, DIC technique will be used in this study.

As the first step of the analyses with WinDIC Menu 1.3 software, modes of the images captured need to be converted from P to L mode using a Python code. Next the converted undeformed and the deformed images were uploaded to the WinDIC software. Since DIC subsets need to be relatively small, subset size was chosen to be 23×23 pixels over a DIC grid with a grid spacing of 5 pixels [85]. An example grid is shown in Figure 3.8.

Optical resolution of the camera is 0.023256 mm/pixel. Hence the grid spacing corresponds to 0.116 mm and the area around the crack tip that was used for deriving the K_{Ic} was chosen as 11.6×11.6 mm.

WinDIC Menu 1.3 software gives the displacement field of each grid point that was defined. The curve fitting was done to the undifferentiated displacement data obtained from the WinDIC software with Equation 3.8 and fracture parameters were

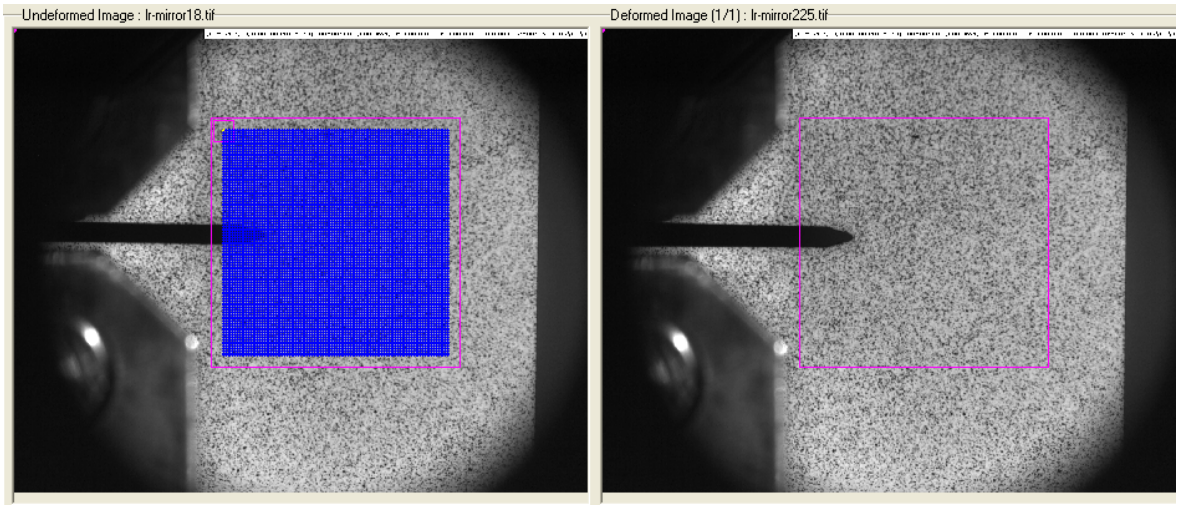


Figure 3.8. An Example Grid Set on Undeformed Image and It's Reflection on The Deformed Image at WinDIC Menu 1.3 Software.

calculated using a Matlab code for numerical implementation.

3.4.4. DIC Results

Fracture toughness tests were done under displacement control at different loading rates with a small preload applied at the beginning of the tests so that effect of the gaps between the specimen and the grips is eliminated for each test. For DIC analysis, first the image right before fracture needs to be determined. For this reason, P_Q the force value used for critical stress intensity factor (K_{Ic}) calculation needs to be known. According to ASTM E399 standard there are three types of load - displacement curves as illustrated at Figure 3.9.

P_Q is the load at the time right before fracture. Once P_Q is determined, the time of this load can be checked from the load time data. Then the image that was captured at this time is determined to be the deformed image for DIC analysis.

Using the method shown at Figure 3.9, P_Q is determined from whichever type is suitable with the load - displacement graphs obtained from the fracture tests for the

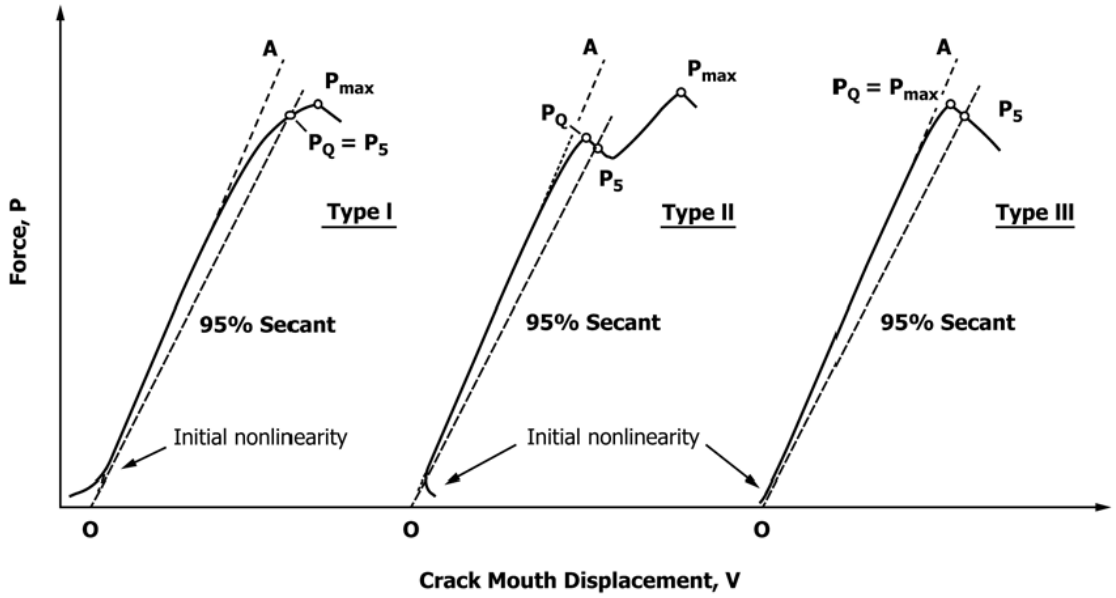


Figure 3.9. Principal Types of Force-Displacement (CMOD) Records [8].

material of the present study. The load - displacement graphs were plotted for NiTi SMA to decide on the type of the curves in Figure 3.10.

As it can be seen from these graphs, NiTi SMA's load - displacement graph is of Type III that $P_{max} = P_Q$, so the maximum load value will be used as P_Q for LEFM calculations and the DIC analyses. The obtained P_{max} and the corresponding crack opening displacement values are tabulated in Table 3.1.

Table 3.1. Maximum load and extension values obtained from fracture experiments at room temperature of 26 °C.

Loading Rate	P_{max} **(N)**	**Extension (mm)**
0.1 mm/min	461	0.3483
0.5 mm/min	481.2	0.3809
1.5 mm/min	499.4	0.3936
2 mm/min	513.4	0.4323

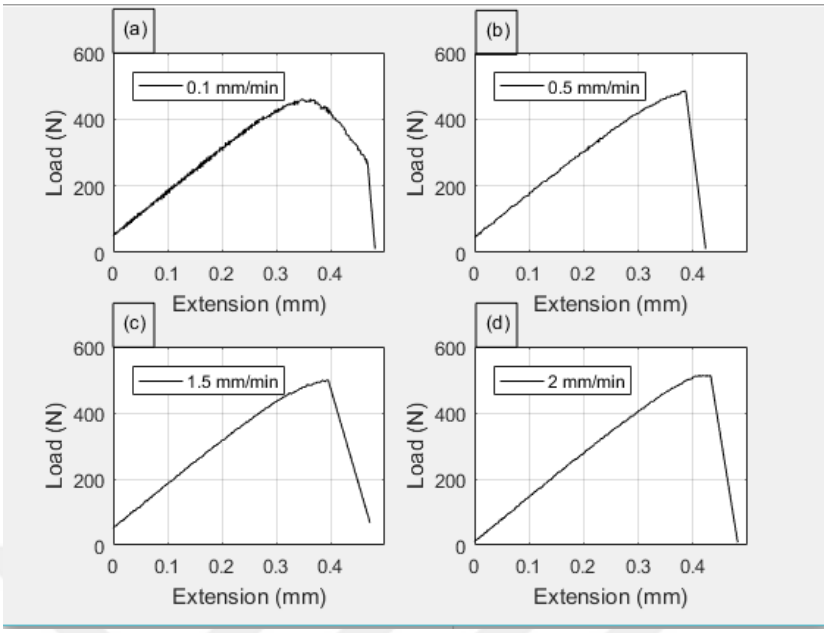


Figure 3.10. Load Displacement Graphs From Fracture Tests at Room Temperature of 26 °C For Loading Rates of (a) 0.1 mm/min, (b) 0.5 mm/min, (c) 1.5 mm/min, (d) 2 mm/min.

In Table 3.1 there is a clear trend of increasing at the maximum force and the extension values with increasing loading rates which can be seen clearly at the following Figure 3.11.

Overall, these results indicate that at higher loading rates, the specimen can resist to higher forces before fracture, which shows that the material toughness increases. A possible explanation for these results may be the different sizes of stress induced martensite transformation regions. Further investigations on this topic will be done in detail at Chapter 4.

The images that correspond to the force P_{max} were chosen as the deformed image for each test. Before uploading the images to the WinDIC Menu 1.3 software, a horizontal flipping needed to be done to obtain a positive coordinate system. Image flipping was implemented using a Python code. Next these modified images were uploaded to the software and the displacement fields were obtained.

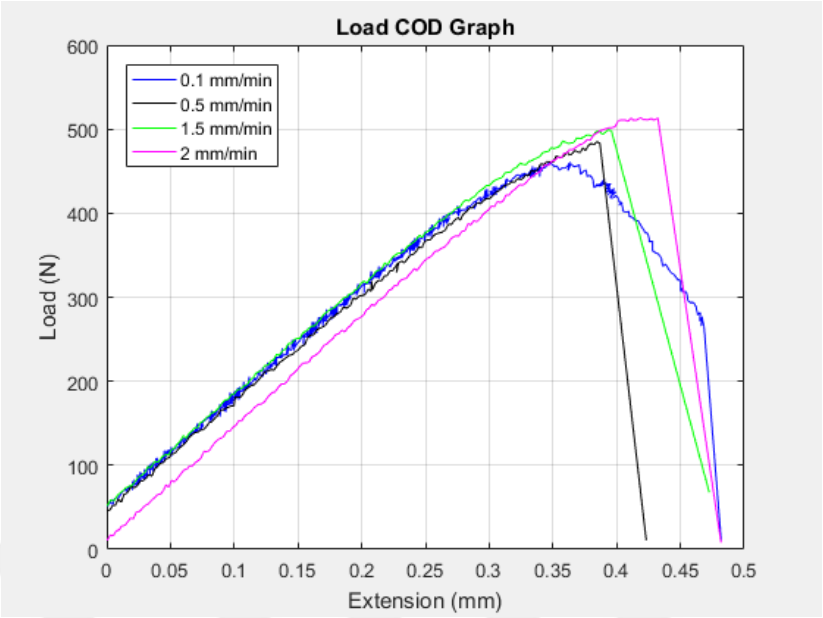


Figure 3.11. Load Displacement Graphs for NiTi From Fracture Tests at Room Temperature of 26 °C For Different Loading Rates.

First using the curve fitting method the unknown parameters at Equation 3.8 (K_I, K_{II}, T, A_1 and u_{0y}) were calculated. Then displacement contours obtained with DIC method and the displacement contours obtained with Equation 3.8 were plotted. The calculated parameters are tabulated at Table 3.2.

Here the r_{min} and r_{max} represent the boundary region of which the calculations are based upon. r_{min} and r_{max} are chosen so that r/a is inside the range of r_{min} and r_{max} where $r^2 = x^2 + y^2$ and a is the crack length. For all the test specimens crack length is different, but the values are close to each other so that the r_{min} and r_{max} values were chosen to be the same for all the tests.

These results at Table 3.2 suggest that the loading rate has a considerable effect on the fracture parameters of NiTi SMA that, with increasing loading rate, fracture toughness of the material K_I increases. These results match those observed in the earlier study of Jiang and Vecchio [70] who found an increase in the fracture toughness of NiTi between quasi-static and dynamic loading conditions. The inconsistent result

Table 3.2. Fracture parameters calculated with curve fitting of the displacement field obtained from DIC technique to Equation 3.8 for the tests conducted at room temperature of 26 °C at different loading rates with $r_{min} = 0.06$ and $r_{max} = 0.8$.

Loading Rate	K_I **(MPa**$\sqrt{m}$**)**	K_{II} **(MPa**$\sqrt{m}$**)**	**T (MPa)**	A_1	u_{0y}
0.1 mm/min	33.27	-0.6923	409.85	0.0018	-0.1173
0.5 mm/min	33.76	0.2912	436.13	-0.0004	-0.1700
1.5 mm/min	29.49	-0.3379	362.64	0.0026	-0.1009
2 mm/min	33.81	-0.1151	413.78	0.0046	-0.0984

for the experiment conducted at 1.5 mm/min loading rate, is guessed to have happened because of an experimental error, because the other results support that the stress intensity factor increases due to increasing loading rates.

As it can be seen from the data at Table 3.2 K_{II} values are found to be very small. This was already expected because the test specimen is under Mode I loading condition. To see the effect of the K_{II} parameter, next round of calculations with the Matlab code were done with taking out the K_{II} term from the Equation 3.8. The resulting parameters are presented at Table 3.3. As it can be seen from the table, the new set of parameters calculated did not show any significant difference for K_I, T, A_1 and u_{0y}. They were found to have almost exactly the same values.

After obtaining the unknown parameters K_I, K_{II}, T, A_1 and u_{0y}, the displacement contour plots can be plotted using the curve fitting of DIC displacement data with Equation 3.8. The numerical implementation of the parameters was done using a Matlab code. Omitting the K_{II} term did not have any effect on the displacement contours plotted with least squares fit. The resulting contour plots of both the DIC data and the least squares fit of Equation 3.8 are presented at Figures 3.12, 3.13, 3.14, 3.15 for loading rates of 0.1 mm/min, 0.5 mm/min, 1.5 mm/min, 2 mm/min, respectively.

Table 3.3. Fracture parameters calculated with least squares fitting of the displacement field obtained from DIC to Equation 3.8 for the tests conducted at room temperature of 26 °C at different loading rates after omitting the K_{II} term with $r_{min} = 0.06$ and $r_{max} = 0.8$.

Loading Rate	**a**	$\frac{a}{W}$	K_I **(MPa$\sqrt{m}$)**	**T (MPa)**	A_1	u_{0y}
0.1 mm/min	13.1	0.5	33.26	409.45	0.0019	-0.1172
0.5 mm/min	13.22	0.51	33.76	436.16	-0.0005	-0.1700
1.5 mm/min	12.93	0.5	29.49	362.69	0.0026	-0.1009
2 mm/min	12.82	0.49	33.81	413.78	0.0046	-0.0984

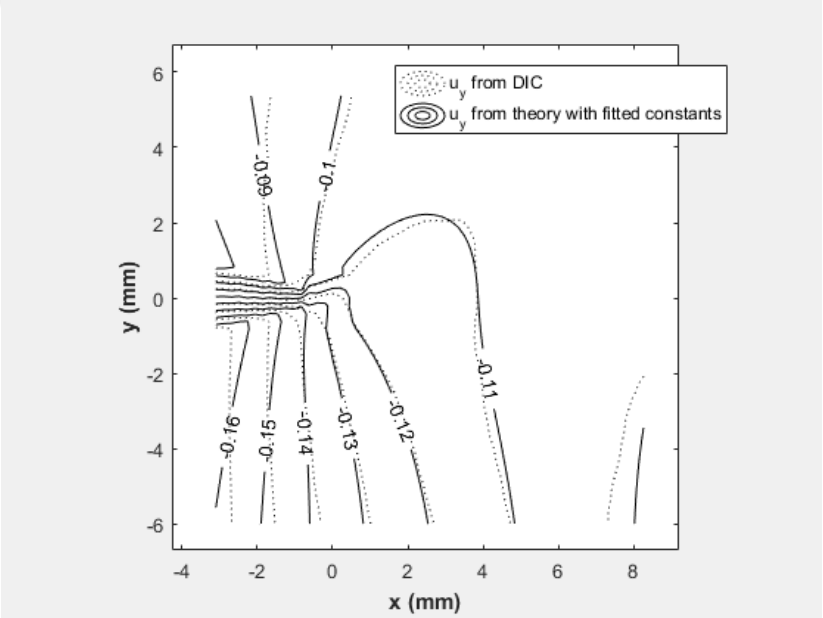


Figure 3.12. Displacement Contour Plot of the data From DIC Technique and Those Calculated Theoretically Using Equation 3.8 With Replacing the Obtained Constants For 0.1 mm/min Loading Rate.

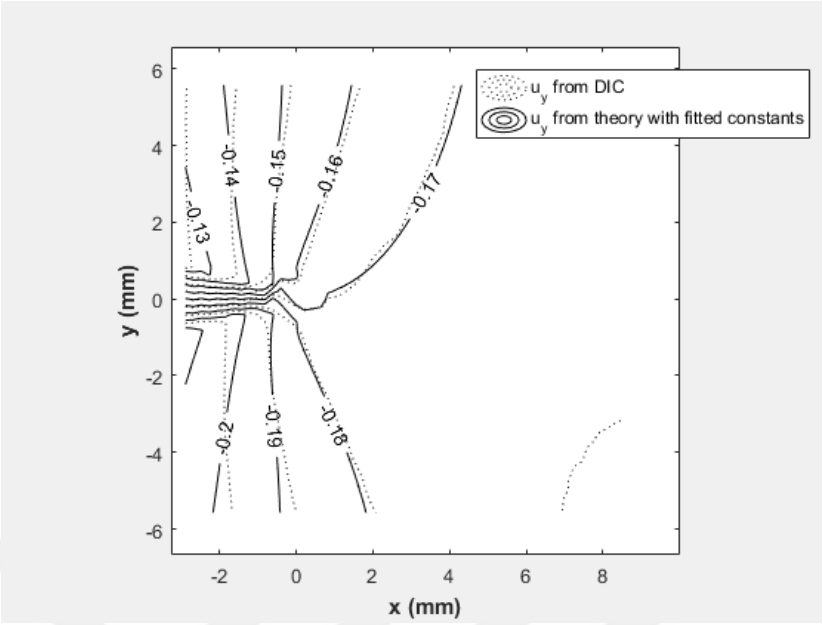


Figure 3.13. Displacement Contour Plot of the data From DIC Technique and Those Calculated Theoretically Using Equation 3.8 With Replacing the Obtained Constants For 0.5 mm/min Loading Rate.

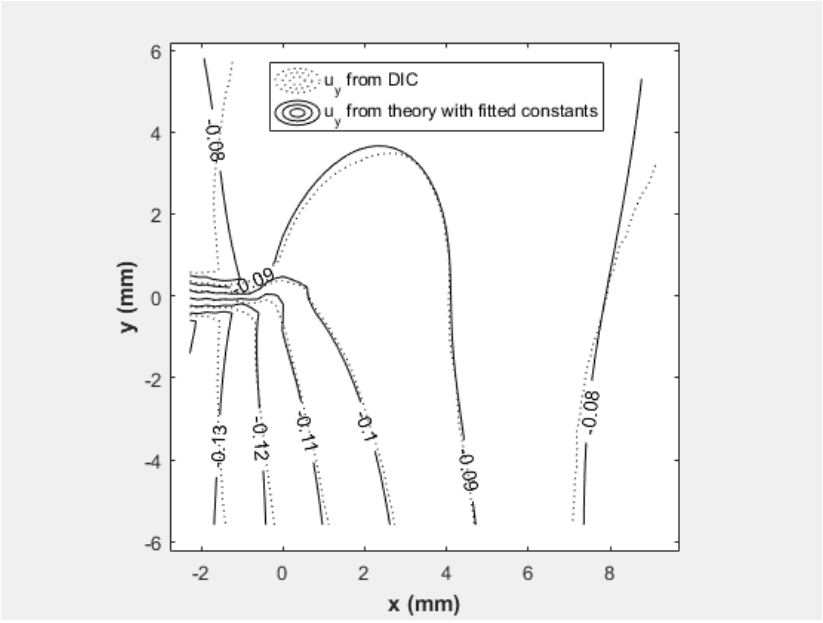


Figure 3.14. Displacement Contour Plot of the data From DIC Technique and Those Calculated Theoretically Using Equation 3.8 With Replacing the Obtained Constants For 1.5 mm/min Loading Rate.

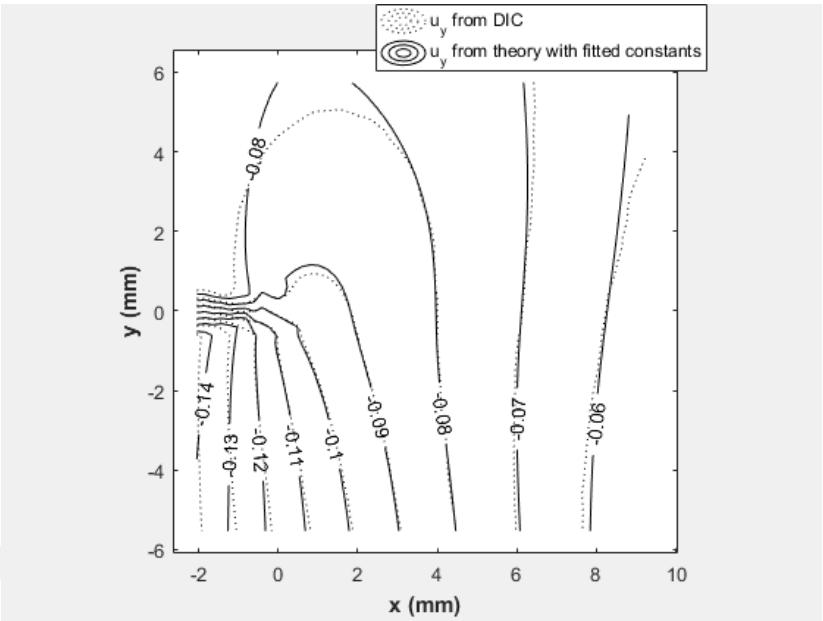


Figure 3.15. Displacement Contour Plot of the data From DIC Technique and Those Calculated Theoretically Using Equation 3.8 With Replacing the Obtained Constants For 2 mm/min Loading Rate.

Locating the coordinate system origin has a major importance for the stress intensity calculations from the DIC data. Because it was observed during the analyses that the calculated K_I value changes significantly upon changing the origin of the coordinate system. For accurate calculation of the stress intensity factor, the crack tip's corresponding x,y coordinates at the DIC data needs to be set as the origin. To locate the crack tip coordinates, rotation ω_{xy} and the strain component ϵ_{xx} is calculated from the DIC displacement data and the resulting contour plots were plotted. Apparently at the crack tip the ω_{xy} and ϵ_{xx} data changes from positive values to negative. Then this point is set as the origin [85].

An important assumption was made for stress intensity factor calculations using the DIC data. As clearly shown at Equation 3.8, E_{tip} needs to be used as the Young's modulus of the material at the tip of the crack. It is already known and accepted by researchers that upon loading, a NiTi SMA fracture specimen undergoes stress induced martensitic phase change at the crack tip. At the tip of the crack the material

is martensite and for the calculation of K_I, martensite Young's modulus needes to be used as E_{tip}. But DIC analyses give superfluous data at the tip of the crack so this region is filtered by defining an r_{min} value. It is already known that the martensite region is very small and it probably is filtered out with the rest of the superfluous data. For this reasons, use of austenite Young's modulus as E_{tip} gives more accurate results for the calculated fracture parameters [85].

3.5. Calculation of Critical Stress Intensity Factor (K_Q) Using ASTM E399

Linear elastic fracture mechanics can be applied to the structures that have small crack tip plastic zone [6]. If an assumption is made for NiTi structures to have a relatively small plastic zone, then LEFM analyses can be used to calculate the critical stress intensity factor K_{Ic} using the equations of ASTM E399 standard. The calculation of the stress intensity factor, K_Q as defined by the ASTM E399 standard, for an edge cracked specimen is as follows:

$$K_Q = \frac{P_Q}{\sqrt{BB_N}\sqrt{W}}.f\left(\frac{a}{W}\right) \tag{3.9}$$

where

$$f\left(\frac{a}{W}\right) = \frac{\left(2+\frac{a}{W}\right)\left[0.886+4.64\left(\frac{a}{W}\right)-13.32\left(\frac{a}{W}\right)^2+14.72\left(\frac{a}{W}\right)^3-5.6\left(\frac{a}{W}\right)^4\right]}{\left(1-\frac{a}{W}\right)^{\frac{3}{2}}} \tag{3.10}$$

P_Q is the force value that was determined to be $P_Q = P_{max}$ as explained in Section 3.3, a is the crack length, W is the specimen width, measured from the centerline of the loading holes to the specimen edge, and B is the specimen thickness [8]. For the specimen used in our experiments the value $B_N = B$, so the calculations were done accordingly.

The calculated K_Q and P_Q results with the dimensions of the specimens used for the experiments conducted at different loading rates are tabulated at Table 3.4.

Table 3.4. Calculated K_Q results with the dimensions of the specimens conducted at room temperature of 26 °C at different loading rates using Equation 3.9.

Loading Rate	**B (mm)**	**W (mm)**	**a (mm)**	$\frac{a}{W}$	P_Q **(N)**	K_Q **(MPa**$\sqrt{m}$**)**
0.1 mm/min	1	26	13.1	0.5	461	27.94
0.5 mm/min	1	26	13.22	0.51	481.2	29.6
1.5 mm/min	1	26	12.93	0.5	499.4	29.68
2 mm/min	1	26	12.82	0.49	513.4	30.11

The results at Table 3.4 shows that there is a slight increase in the critical stress intensity factors of the NiTi SMA, calculated using LEFM. Even if the resulting K_Q values are very close, still the results support that fracture toughness increases with increasing loading rates.

4. EVALUATION OF TRANSFORMATION REGION AROUND CRACK TIP

Upon loading a specimen with a crack, stress field around the crack tip raise up to very high values as LEFM suggests. In the case of SMA materials, this raise in the stress causes stress induced martensite transformation at the tip of the crack and this region continues to enlarge with increase in load [78]. In this chapter, the martensitic region and the transformation region that is the region both austenite and martensite phases are found to be together, are calculated first, using the data obtained with DIC technique, then with the analytical transformation function proposed by Hazar *et al.* [71].

4.1. Introduction

The normal stress σ_{yy} given by Equation 3.2 is for a linear elastic material. Irwin suggested that, if it is applied for the case of $\theta = 0$, the stresses given by this equation satisfy a yield criterion for the boundary between elastic and plastic regions. Yielding occurs when the uniaxial stress $\sigma_{yy} = \sigma_{YS}$ for plane stress conditions.

According to Irwin, substituting the uniaxial yield strength into Equation 3.2 with $\theta = 0$ and solving for r, a first-order estimate of the plastic zone size can be calculated as follows [6]:

$$r_y = \frac{1}{2\pi}\left(\frac{K_I}{\sigma_{YS}}\right)^2 \tag{4.1}$$

But this analysis is not exactly correct since it was based on an elastic crack tip solution. Equilibrium state of stresses needs to be satisfied when yielding occurs.

The elastic region in Figure 4.1 corresponds to the forces on an elastic material. But as the stress values can not go beyond the yield stress, these forces can not be

used for a elastic - plastic material. So as to fit these forces the plastic zone size needs to increase.

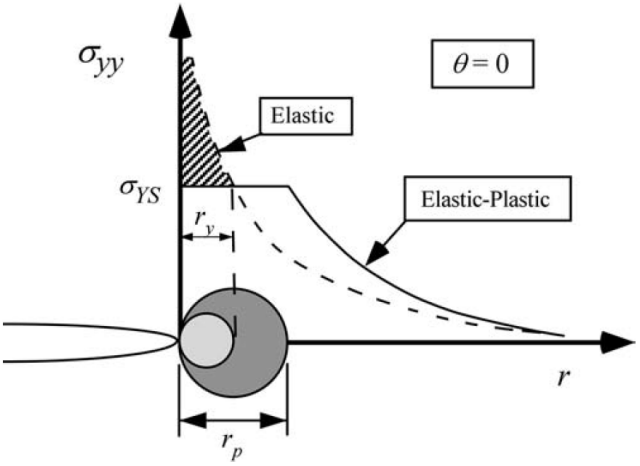


Figure 4.1. Representation of First Order (r_y) and Second Order (r_p) Estimates of Plastic Zone Sizes Proposed by Irwin [6].

A second-order estimate of the plastic zone can be calculated using a force balance equation as represented at Equation 4.2:

$$\sigma_{YS} r_p = \int_0^{r_y} \sigma_{yy} dr = \int_0^{r_y} \frac{K_I}{\sqrt{2\pi r}} dr \tag{4.2}$$

Finally solving for r_p;

$$r_p = \frac{1}{\pi} \left(\frac{K_I}{\sigma_{YS}} \right)^2 \tag{4.3}$$

Considerable number of researchers [4, 15, 88–90], used modified models of this method for SMAs to obtain an estimation of the phase transformation region occured around the crack tip.

Evaluation of the transformation region around the crack tip has substantial necessity for fracture toughness of NiTi SMAs, since critical stress intensity factor increases as a result of stress-induced martensitic (SIM) transformation. Although there

are studies on calculations and measurements of transformation regions around the crack tip, there is still a need for experiments to do comparison with the analytical calculations. In this study martensitic and the phase transformation region are estimated using DIC technique and with the analytical calculations.

4.2. Evaluation of Transformation Region

For evaluation of the transformation region, the displacement field data obtained from DIC were used to calculate the strain field (ϵ_{xx}, ϵ_{yy}, ϵ_{xy} for plane stress) on the test specimen surface using Matlab for numerical implementation. Then equivalent strain ϵ_{eq} was calculated taking the Poisson's ratio as $\nu = 0.5$ which gives better results for the process zone where the dominant stresses are the transformation stresses. Taking Poisson's ratio as $\nu = 0.33$ at this zone is not appropriate since it corresponds to the elastically deformed austenite region. Next the equivalent strain contours that correspond to the martensite transformation start strain (ϵ_{eq}^{MS}) and the martensite transformation finish strain (ϵ_{eq}^{MF}) were plotted. Haghgouyan *et al.* [85] proposed in their paper that the contour corresponds to ϵ^{MS} approximates the transformation zone outer boundary and ϵ^{MF} approximates the fully martensitic region zone boundary.

For analytical calculation of transformation zone, the equation which is presented by Hazar *et al.* [71] was used. Two separate calculations were done first using the K_Q value obtained from LEFM calculations and second using the K_I calculated from DIC.

4.2.1. Transformation Strains

Since the estimation of the transformation zone around the crack tip is based on the transformation strain contours on the specimen surface strain field, first the phase transformation strains are needed to be defined. The strain contour boundary which corresponds to the martensite start strain denotes the phase transformation region and the strain contour boundary which corresponds to the martensite finish strain denotes the fully martensitic region. These strain values were obtained from the stress - strain curves of the tensile tests conducted at room temperature of 26 °C presented in Figure

2.7. Forward transformation start and finish strains were found following the method proposed by Maletta and Furgiuele [3] which is used previously for determination of the transformation stresses as shown in Figure 2.5. Strain values are specified according to the corresponding transformation stress values. Martensite transformation start and finish strains that were used in this study for estimation of transformation zone using DIC technique are presented at Table 4.1.

Table 4.1. Martensite transformation start and finish strains used for transformation zone estimation using the equivalent strain contours obtained from DIC displacement data for loading rates of 0.1 mm/min, 0.5 mm/min, 1.5 mm/min and 2 mm/min.

Loading Rate	ϵ_{MS} (%)	ϵ_{MF} (%)
0.1 mm/min	0.78	6.14
0.5 mm/min	0.93	6.51
1.5 mm/min	0.89	6.67
2 mm/min	0.99	6.77

4.2.2. Estimation of Transformation Zone Using DIC

After the determination of the phase transformation strains, these strain values were implemented to Matlab code that plots the equivalent strain contours and the contours that correspond to the ϵ_{MS} and ϵ_{MF} values were plotted. However, the equivalent strain values calculated using strain field of the DIC displacement data does not give the fully martensitic region size which was supposed to be the contour that corresponds to the martensite phase transformation finish strain that is ϵ_{MF}. This is because the resolution of the measurement is not sufficient to obtain strain measurements higher than 6 % strain. The calculated maximum equivalent strain values have lower values. As a result, fully martensitic transformation region could not be measured. But the strain contours that correspond to ϵ_{MS} could be obtained, hence the phase transformation region where austenite and the martensite phases exist together could be measured. The results are represented at Table 4.2.

Table 4.2. Measured phase transformation region (PTR) (r_T) using the equivalent strain contours obtained from DIC displacement data for loading rates of 0.1 mm/min, 0.5 mm/min, 1.5 mm/min, 2 mm/min and the K_I values obtained from DIC least-squares fitting to Equation 3.8.

Loading Rate	K_I **(MPa**$\sqrt{m}$**)**	r_T **(mm)**
0.1 mm/min	33.26	0.6898
0.5 mm/min	33.76	0.6302
1.5 mm/min	29.49	0.4989
2 mm/min	33.81	0.4704

It is evident from the results at Table 4.2 that, increasing loading rate causes the stress intensity factor to increase which consequently effects the phase transformation region around the crack tip. Size of the phase transformation region significantly decreases due to increasing loading rate. Although the stress intensity factor value for loading rate of 1.5 mm/min is lower than the higher loading rate experiment 2 mm/min, phase transformation region around the crack tip is larger than the faster loading rate experiment's. This may be because the measured phase transformation region is outside of the zone that effects the fracture toughness. Therefore, even if the stress intensity factor has a lower value, phase transformation region still expanded as it was expected.

4.3. Analytical Calculation of Transformation Zone

Hazar *et al.* [71] proposed a function to analytically calculate the extent of the martensitic transformation region. They used the forward phase transformation function presented at Equation 4.4 introduced by Zaki and Moumni [91]:

$$F_\zeta = \left\{ E' \frac{\sigma_e^2}{3} + \frac{1}{2}\left(\frac{1}{3}E' + \nu'\right)\sigma_{ii}^2 - C(T) \right\} + \sigma_{ij}\varepsilon_{ij}^{ori}$$

$$-(\Gamma + b)\zeta - a(1-\zeta) - \left[(\alpha - \beta)\zeta + \frac{\beta}{2}\right]\left(\frac{2}{3}\varepsilon_{ij}^{ori}\varepsilon_{ij}^{ori}\right) \tag{4.4}$$

Here, in the case $F_\zeta = 0$, forward transformation occurs. In this equation, $\sigma_e = \sqrt{\frac{3}{2}\sigma_{ij}^d \sigma_{ij}^d}$ is the von Mises stress, σ_{ij} represents the Cauchy stress tensor, σ_{ij}^d is the deviatoric stress tensor, σ_{ii} is the trace of the Cauchy stress tensor and ζ is the martensite volume fraction. E' and ν' are shown with equations below:

$$E' = \frac{(1+\nu)(E_A - E_M)}{E_A E_M} \tag{4.5}$$

$$\nu' = \frac{\nu(E_M - E_A)}{E_M E_A} \tag{4.6}$$

Here, E_A is the Young's modulus of the austenite and E_M is the martensite Young's modulus, ν is the Poisson's ratio and it is the same for the each phase that $\nu_M = \nu_A = \nu$. The parameters a and b are defined as:

$$a = \frac{1}{2}\left[\left(\frac{1}{E_M} - \frac{1}{E_A}\right)\frac{\sigma_{MS}^2 - \sigma_{AF}^2}{2} + (\sigma_{MS} - \sigma_{AF})\varepsilon_0\right] \tag{4.7}$$

$$b = \frac{1}{2}\left[\left(\frac{1}{E_M} - \frac{1}{E_A}\right)\frac{\sigma_{MF}^2 - \sigma_{AS}^2}{2} + (\sigma_{MF} - \sigma_{AS})\varepsilon_0\right] \tag{4.8}$$

Here σ_{MS}, σ_{MF}, σ_{AS} and σ_{AF} denotes the phase transformation stresses of forward (martensite start - finish) and reverse (austenite start - finish) transformations and ε_0 is the equivalent transformation strain. $C(T)$ is the phase change heat density at

temperature T and is presented at Equation 4.9:

$$C(T) = \frac{1}{2}\left[\left(\frac{1}{E_M} - \frac{1}{E_A}\right)\frac{\sigma_{MS}^2 + \sigma_{AF}^2}{2} + (\sigma_{MS} - \sigma_{AF})\varepsilon_0 - \beta\varepsilon_0^2\right] \tag{4.9}$$

α is a parameter that controls the slope of the stress - strain curve representing the martensite orientation and β controls the martensite variants' orientation level. Last parameter ε_{ij}^{ori} is the strain that is resulted by orientation of martensite variants.

Finally, Γ is defined as follows:

$$\Gamma = \frac{1}{2}\left[\left(\frac{1}{E_M} - \frac{1}{E_A}\right)\frac{\sigma_{MF}^2 - \sigma_{MS}^2 + \sigma_{AS}^2 - \sigma_{AF}^2}{2}\right]$$

$$+\frac{1}{2}\left[(\sigma_{MF} - \sigma_{MS} + \sigma_{AS} - \sigma_{AF})\varepsilon_0 - 2(\alpha - \beta)\varepsilon_0^2\right] \tag{4.10}$$

By use of the asymptotic stress equations for the von Mises stress stress tensor is found as shown at Equation 4.11 for the plane stress case:

$$\sigma_e = \frac{K_I}{2\sqrt{\pi r}}\left[1 + cos\theta + \frac{3}{2}sin^2\theta\right]^{\frac{1}{2}} \tag{4.11}$$

Using the same method, σ_{ii} and $\varepsilon_{ij}^{ori}\sigma_{ij}$ are obtained as:

$$\sigma_{ii} = \frac{K_I}{2\sqrt{\pi r}}\left[1 + cos\theta\right]^{\frac{1}{2}} \tag{4.12}$$

$$\varepsilon_{ij}^{ori}\sigma_{ij} = \epsilon_0\frac{K_I}{2\sqrt{\pi r}}\left[1 + cos\theta + \frac{3}{2}sin^2\theta\right]^{\frac{1}{2}} \tag{4.13}$$

Inserting Equations 4.11, 4.12 and 4.13 into the Equation 4.4 and taking $F_\zeta = 0$:

$$E' \frac{K_I^2}{12\pi r_M} \left[1 + cos\theta + \frac{3}{2} sin^2\theta\right] + \frac{1}{2}\left(\frac{1}{3}E' + \nu'\right) \frac{K_I^2}{4\pi r_M}[1 + cos\theta]$$

$$-C(T) + \varepsilon_0 \frac{K_I}{2\sqrt{\pi r_M}} \sqrt{\left[1 + cos\theta + \frac{3}{2} sin^2\theta\right]} - (\Gamma + b)\zeta$$

$$-a(1-\zeta) - \left((\alpha - \beta)\zeta + \frac{\beta}{2}\right)\varepsilon_0^2 = 0 \qquad (4.14)$$

Solving this equation for r_M using $\zeta = 1$ and $\theta = 0$, the size of the martensitic region on $\theta = 0$ axis can be calculated.

Similarly, solving Equation 4.14 using $\zeta = 0$ and $\theta = 0$, gives the phase transformation region size on $\theta = 0$ axis. In the phase transformation region both martensite and austenite phases coexist.

Calculations were done using the material properties obtained from tension tests tabulated at Table 2.2 which represents the Young's modulus of austenite and martensite and Table 2.3 which represents the martensite start, martensite finish, austenite start and austenite finish stresses.

First round of calculations were done implementing the K_I values calculated from ASTM E399 Equation 3.9 which are tabulated at Table 3.4. The resulting martensitic region (r_M) and the phase transformation region (r_T) values on the $\theta = 0$ axis are represented at Table 4.3.

Next the same calculations were done implementing the K_I values calculated from DIC data least-squares fitted to Equation 3.8 which are tabulated at Table 3.2. The resulting martensitic region (r_M) and the phase transformation region (r_T) values on the $\theta = 0$ axis are represented at Table 4.4.

Table 4.3. Calculated martensitic region (r_M) for the case $\zeta = 1$ and the phase transformation region (r_T) for the case $\zeta = 0$ using Equation 4.14 for loading rates of 0.1 mm/min, 0.5 mm/min, 1.5 mm/min, 2 mm/min, with K_I calculated from ASTM E399 Equation 3.9, when $\theta = 0$.

Loading Rate	r_M **(mm)**	r_T **(mm)**
0.1 mm/min	0.5071	0.6873
0.5 mm/min	0.4627	0.6862
1.5 mm/min	0.3360	0.6584
2 mm/min	0.3084	0.6563

Table 4.4. Calculated martensitic region (r_M) for the case $\zeta = 1$ and the phase transformation region (r_T) for the case $\zeta = 0$ using Equation 4.14 for loading rates of 0.1 mm/min, 0.5 mm/min, 1.5 mm/min, 2 mm/min, with K_I calculated from DIC data least-squares fitted to Equation 3.8, when $\theta = 0$.

Loading Rate	r_M **(mm)**	r_T **(mm)**
0.1 mm/min	0.7186	0.9739
0.5 mm/min	0.6018	0.8926
1.5 mm/min	0.3317	0.65
2 mm/min	0.3889	0.8274

The results presented at Table 4.3 that gives the fully martensitic and the phase transformation regions calculated using Equation 4.14 have a decreasing trend as the loading rate increases. This is the result of the increasing fracture toughness. When the loading rate of a fracture specimen is high, it does not have enough time for phase transformation before it goes to fracture. Previous studies note that, the phase transformation reduces the crack tip stress intensity factor [13,17,26]. So in the case the phase transformation region is large, the SIF value decreases. Or it can be said that as the SIF value increases, the phase transformation region around the crack tip decreases.

The results of the present study supports this and shows that the increasing loading rate increases the crack tip stress intensity factor and as a result the fully martensite and the transformation zone sizes around the crack tip decrease. In addition, these analytically calculated phase transformation sizes are in good agreement with the experimentally measured phase transformation sizes obtained using the DIC technique.

Similarly, results presented at Table 4.4 were obtained from the calculations done using the stress intensity factor obtained from the DIC measurements. The inconsistency with the 1.5 mm/min experiment case is also observed for the phase transformation region size calculations as well. But taking aside this experiment's results, both fully martensite and the transformation zone sizes around the crack tip has a decreasing trend with increasing loading rate. Nevertheless, the transformation zone size values presented at Table 4.4 are higher than the experimentally measured phase transformation sizes obtained using the DIC technique and the calculations using the K_Q calculated from ASTM E399 Equation 3.9. But still, these results are in acceptable range with the preceding results of experiments and the analytical results.

5. COMPUTATIONAL EVALUATION OF TRANSFORMATION REGION AND FRACTURE PARAMETERS

5.1. Problem Statement

In this chapter, as an extension of the experimental and analytical work, for the sake of completeness, a finite element analysis using ABAQUS was performed. To implement the material properties of NiTi, ABAQUS's built-in user material subroutine proposed by Auricchio - Taylor - Lubliner was used. But this built-in model is rate independent, thus, it can not be used for a rate dependent problem. To implement the effect of different loading rates, a user material (UMAT) subroutine that is rate dependent is needed. For this reason the material properties were changed for each model using the material properties obtained from tensile tests conducted at different loading rates.

The compact tension specimen was modeled with the exact same fatigue precrack size used in each fracture test. Using symmetry, only the upper half of the specimen was modeled. The model used is presented at Figure 5.1.

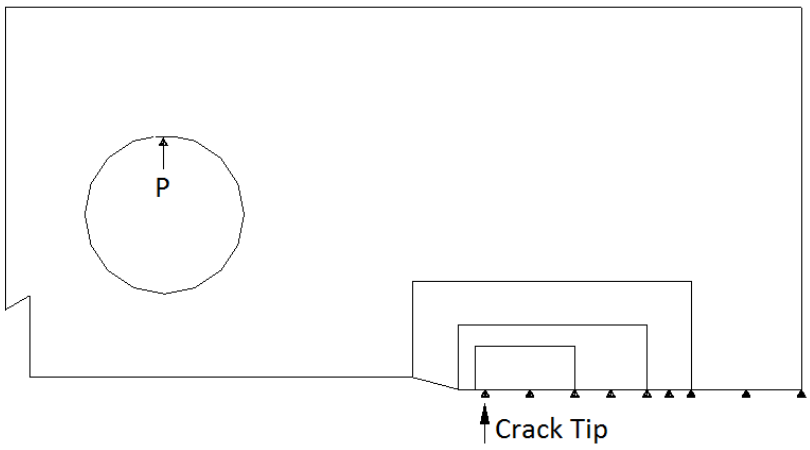


Figure 5.1. Geometry of the 2D Finite Element Model.

Because NiTi shows a pseudoelastic behavior, a very fine mesh is needed at the crack tip where the martensitic transformation occurs. For this reason, the model was divided into regions with different mesh sizes getting finer approaching the crack tip and reduced integration plane stress elements (CPS8R) were used. Figure 5.2 illustrates the geometry and the mesh of the half model.

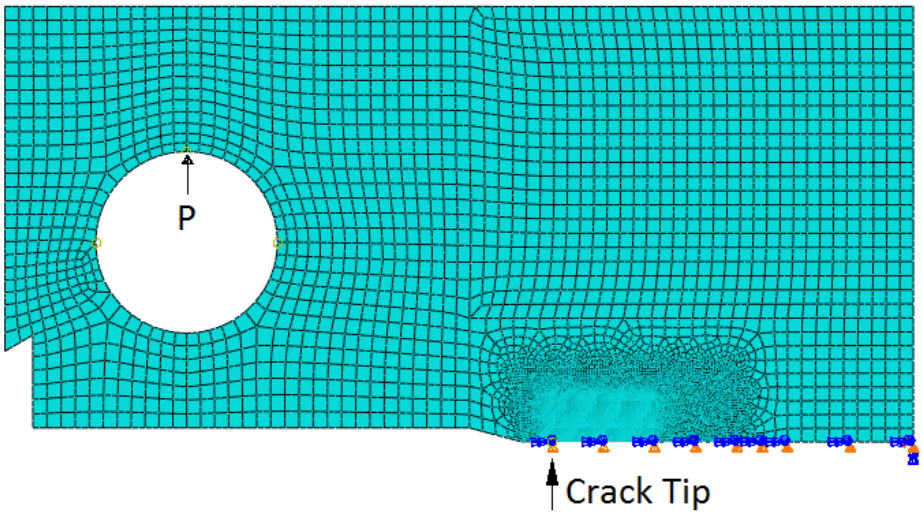


Figure 5.2. Mesh of the 2D Finite Element Model.

For the material properties required in calculations, for reasons explained in the previous chapter results obtained from tensile tests were implemented for each loading rate. Because the material properties of the models for different loading rates change, σ_{MS}, σ_{MF}, σ_{AS} and σ_{AF}, and E_A, E_M were obtained from tensile tests represented at Table 2.2 and Table 2.3. The loads applied were taken as the maximum load values of the fracture toughness tests as tabulated in Table 3.4. The reason behind the use of the maximum load was to reproduce the same conditions for K_Q critical stress intensity factors calculations. This maximum load, P_{max}, is applied to the pin hole at the pin contact point as in the experiments (shown in Figure 5.2). Four similar models with the same geometry and mesh were used.

The stress-strain and the stress-temperature curves of superelastic NiTiNOL designating the material parameters used in the built-in model of ABAQUS are plotted in Figure 5.3.

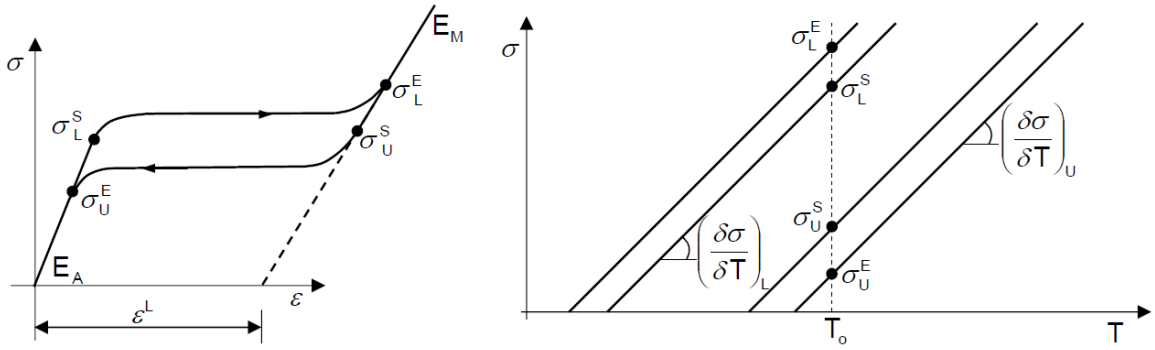


Figure 5.3. Stress - Strain and Stress - Temperature Graph of NiTiNOL of the Built-in Model [9].

The material properties used for modeling are tabulated at Table 5.1 for the loading rates that were used.

Table 5.1. Material properties implemented to the FE ABAQUS models for loading rates of 0.1 mm/min, 0.5 mm/min, 1.5 mm/min, 2 mm/min at room temperature of 26 °C.

	0.1 mm/min	**0.5 mm/min**	**1.5 mm/min**	**2 mm/min**
E_A **(GPa)**	62 ± 1	62 ± 1	62 ± 1	62 ± 1
E_M **(GPa)**	45 ± 1	45 ± 1	45 ± 1	45 ± 1
σ_L^S **(MPa)**	470	501	514	523
σ_L^E **(MPa)**	495	549	646	684
σ_U^S **(MPa)**	220	184	160	156
σ_U^E **(MPa)**	216	139	78	43
ε^L	0.06	0.06	0.06	0.06

5.2. Computational Tensile Tests

Preceding the fracture modelling of NiTi, tensile tests were modeled to see whether the material behaved as expected. For this purpose, the material properties presented

in Table 5.1 were implemented to a single element, and a maximum displacement was applied to obtain 8 % strain. After the FE analyses were completed, stress - strain diagrams were plotted. Figure 5.4 illustrates the stress - strain diagrams obtained from ABAQUS using the material properties of the experiments conducted at a room temperature of 26 °C for loading rates of 0.1 mm/min, 0.5 mm/min, 1.5 mm/min and 2 mm/min.

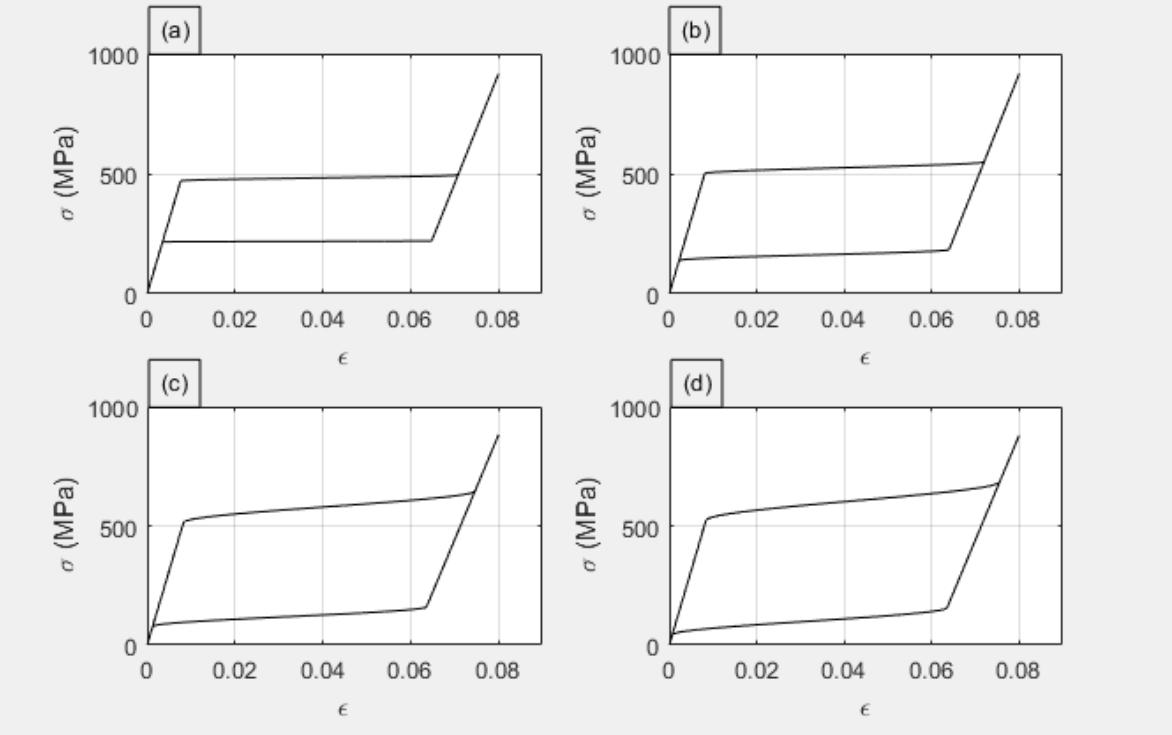


Figure 5.4. Stress-Strain Diagrams Obtained From FEA Using the Material Properties From Tensile Tests Conducted at Room Temperature of 26 °C For Loading Rates of (a) 0.1 mm/min, (b) 0.5 mm/min, (c) 1.5 mm/min, (d) 2 mm/min.

As clearly seen in Figures 5.4 a-d, the hysteresis area expands with increasing loading rate as in the case of experimental results. Curves were plotted together for clear observation at Figure 5.5.

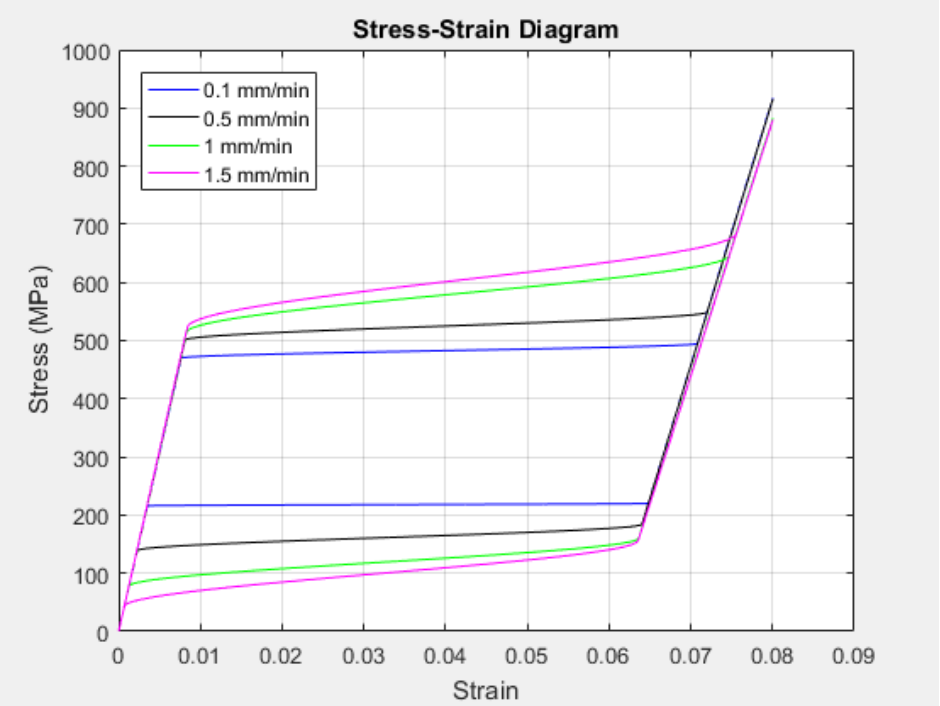


Figure 5.5. Stress-Strain Diagrams at Different Loading Rates.

It is clear from Figure 5.5 that FEA results are in good agreement with the experimentally obtained stress - strain curves. So one can expect that the FEA of fracture of NiTi specimen may give a good qualitative approximation to the experimental results. As a result, ABAQUS is used to simulate fracture tests with the built-in UMAT that models the superelastic effect.

5.3. Computational Fracture Tests

The FEA of the fracture specimen was performed and resulting martensitic volume fraction contours that ABAQUS calculates, were plotted. In Figures 5.6, 5.7, 5.8 and 5.9 the martensite volume fraction contours for loading rates of 0.1 mm/min, 0.5 mm/min, 1.5 mm/min and finally 2 mm/min, respectively. Here, the r_M and r_T denote the fully martensitic transformation zone size and the phase transformation region size are plotted, respectively.

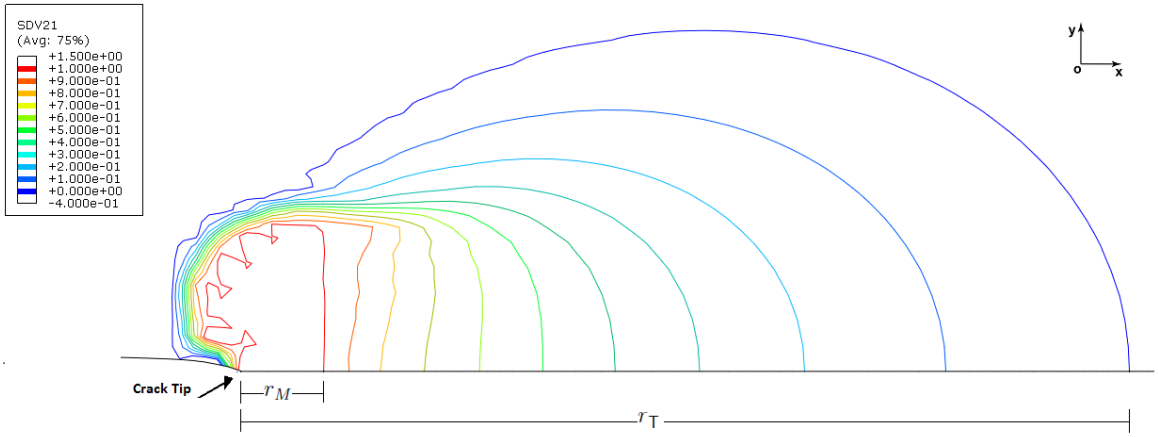


Figure 5.6. Martensite Volume Fraction Contours From FE For Loading Rate of 0.1 mm/min.

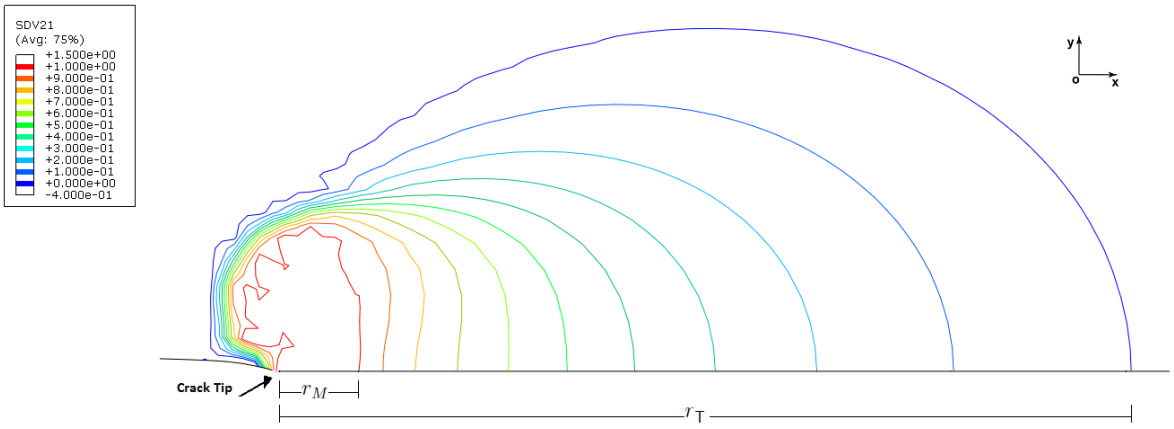


Figure 5.7. Martensite Volume Fraction Contours From FE For Loading Rate of 0.5 mm/min.

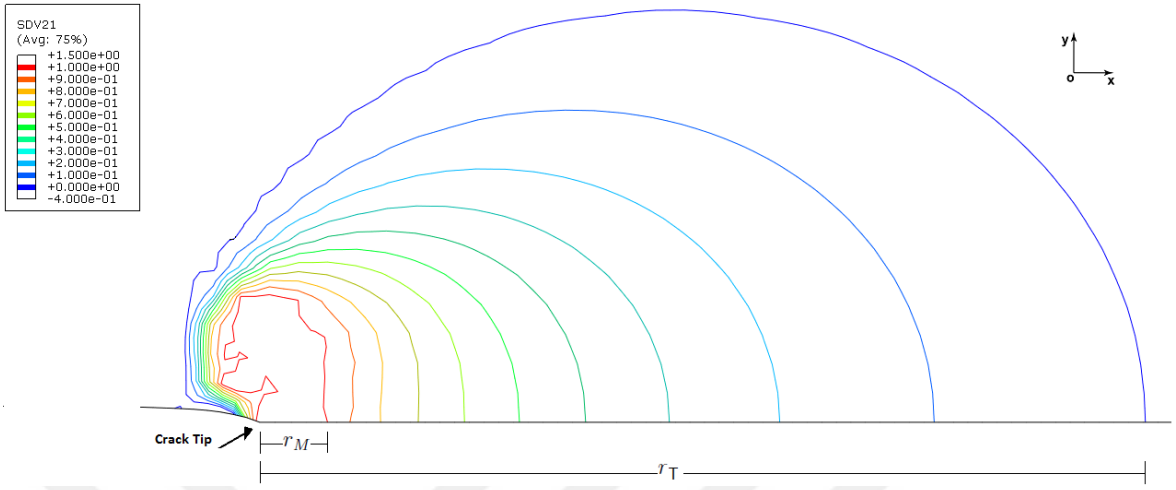


Figure 5.8. Martensite Volume Fraction Contours From FE For Loading Rate of 1.5 mm/min.

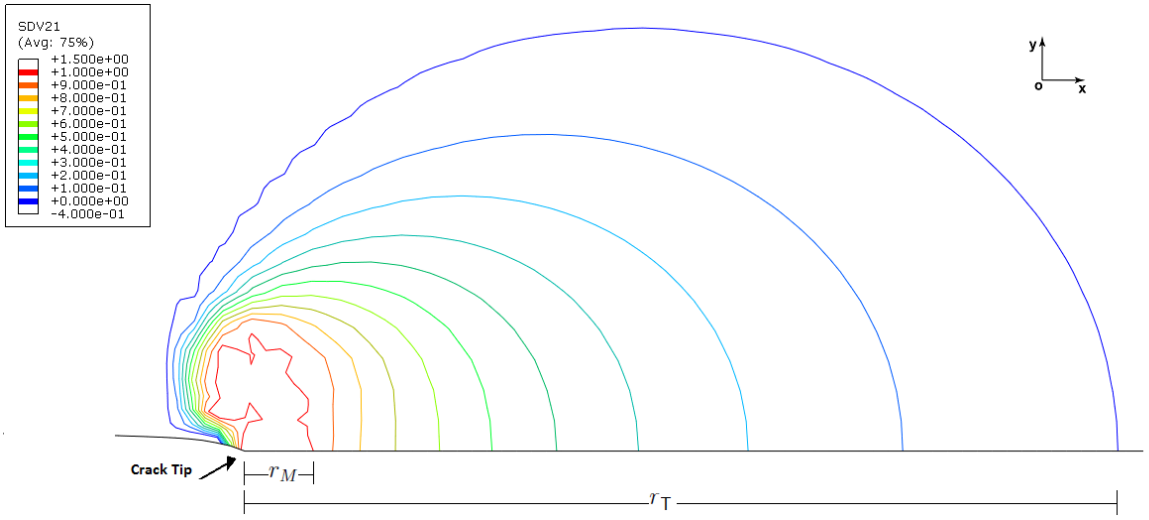


Figure 5.9. Martensite Volume Fraction Contours From FE For Loading Rate of 2 mm/min.

The figures show that martensitic volume fraction contour sizes decrease as the loading rate increases. In Table 5.2, full martensitic zone r_M and the total phase transformation zone, r_T are plotted. r_M is measured between the crack tip and the $\zeta = 1$ contour boundary and r_T is measured between the crack tip and the $\zeta = 0$ contour boundary on the x-axis when $\theta = 0$. The transformation zone extends from the crack tip to r_T.

Table 5.2. Martensitic region r_M and the phase transformation region, r_T for loading rates of 0.1 mm/min, 0.5 mm/min, 1.5 mm/min, 2 mm/min.

Loading Rate	r_M **(mm)**	r_T **(mm)**
0.1 mm/min	0.078	0.9
0.5 mm/min	0.075	0.86
1.5 mm/min	0.051	0.76
2 mm/min	0.055	0.74

As shown in Table 5.2, these results are in good agreement with the experimental results presented in Tables 4.2, 4.3 and 4.4. Only the r_M measured for the case of 1.5 mm/min was found to be smaller than that of the 2 mm/min loading rate case although it was expected to be larger. This unexpected difference at the 1.5 mm/min loading rate case might be a result of a modeling error in the mesh or an experimental error in the test. In any case, if we take aside the 1.5 mm/min model, the phase transformation region size decreases with increasing loading rate. Martensitic transformation size decreases as the loading rate increases, thus the forward transformation stresses increase. Similar results were obtained by Şimşek [92] who showed the effect of transformation stresses on the phase transformation region in her computational calculations.

The full martensitic zone sizes were found to be smaller than those of analytical calculations presented in Tables 4.3 and 4.4. This is believed to be due to the dependence of FE results on mesh size. Initially FEA were performed with a coarser

mesh that showed the dependence on the mesh size. The stress field was obtained to be lower than the transformation stresses that resulted in no full martensite transformation around the crack tip, and after using a finer mesh that the full martensite transformation zone could be obtained. So probably a finer mesh would give larger full martensite transformation region sizes. This gives a reasonable explanation for the full martensitic transformation zones around the crack tip to be smaller than the ones obtained from analytical calculations.

5.4. Computational Evaluation of Fracture Parameters

For validating the experimentally obtained stress intensity factor results, J contour integrals calculated with FE are used. As a result of transformation the integrals are contour dependent, and J-integral converges to a constant value, J_∞ at a contour outside of the phase transformation region. For a small scale transformation zone around the crack tip, it is assumed that the LEFM relation that relates J to K is applicable for calculating the stress intensity factor:

$$J_\infty = \frac{K^2}{E} \tag{5.1}$$

for plane stress, K is the stress intensity factor, and E is the Young's modulus of austenite. J contour integrals obtained from FE and the calculated K_I values tabulated below in Table 5.3:

Table 5.3. J-Integral values obtained from FEA and the corresponding K_I using the LEFM relation between them, Equation 5.1.

Loading Rate	J_∞ (kJ/m^2)	K_I $(MPa\sqrt{m})$
0.1 mm/min	13.35	28.67
0.5 mm/min	14.89	30.32
1.5 mm/min	14.72	30.23
2 mm/min	15.05	30.62

As it can be seen from the Table 5.3, these results are in good agreement with the experimental ones. The stress intensity factor calculated for the 1.5 mm/min loading rate is found to be smaller than that of the 0.5 mm/min loading rate which was also seen at the experimental results obtained using DIC. This difference at the 1.5 mm/min loading rate case might be the result of a modeling or an experimental error so that the calculated material properties obtained from the tests might not be the actual material properties. However, the stress intensity factors calculated behave as expected overall. It can still be said that the stress intensity factor increases with increasing loading rate.

Next, a curve was fitted to the full displacement field data obtained from the FEA as was done previously to DIC data and the unknown parameters in Equation 3.8 (K_I, K_{II}, T, A_1 and u_{0y}) were calculated. The calculated parameters are tabulated in Table 5.4.

Table 5.4. Fracture parameters calculated using the displacement field obtained from ABAQUS at different loading rates with $r_{min} = 0.05$ and $r_{max} = 0.295$.

Loading Rate	K_I **(MPa**$\sqrt{m}$**)**	K_{II} **(MPa**$\sqrt{m}$**)**	**T (MPa)**	A_1	u_{0y}
0.1 mm/min	33.12	9.04	328.21	0.0005	0.0027
0.5 mm/min	34.85	7.35	319.92	0.0003	0.0024
1.5 mm/min	35.03	6.4	328.75	0.0003	0.0019
2 mm/min	35.52	6.24	337.22	0.0003	0.0019

Here the r_{min} and r_{max} represent the boundary region of which the calculations are based upon. r_{min} and r_{max} are chosen so that r/a is inside the range of r_{min} and r_{max} where $r^2 = x^2 + y^2$ and a is the crack length. For all the test specimens crack length is different, but the values are close to each other so that the r_{min} and r_{max} values were chosen to be the same for all the tests.

The results shown in Table 5.4 indicate that the stress intensity factors have an increasing trend with increasing loading rate under Mode I loading. The findings further support the idea that the stress intensity factor increases with increasing loading

rate. SIF results are in good agreements with the SIFs obtained from the experiments. K_{II} values are rather very small when compared to K_I values. So new set of calculations were conducted omitting the K_{II} from Equation 3.8. Resulting fracture parameters are tabulated in Table 5.5; it can be seen that omitting the K_{II} did not have a significant effect on K_I values.

Table 5.5. Fracture parameters calculated from displacement data obtained from ABAQUS omitting the K_{II} with $r_{min} = 0.05$ and $r_{max} = 0.295$.

Loading Rate	**a**	$\frac{a}{W}$	K_I **(MPa**$\sqrt{m}$**)**	**T (MPa)**	A_1	u_{0y}
0.1 mm/min	13.1	0.5	34.43	291.71	-0.0006	0.0014
0.5 mm/min	13.22	0.51	35.69	285.78	-0.0006	0.0015
1.5 mm/min	12.93	0.5	36.14	310.1	-0.0004	0.0011
2 mm/min	12.82	0.49	36.68	320.01	-0.0004	0.0010

The SIFs calculated show an increasing trend with increasing loading rate. This time no inconsistency was observed in the K_I values for 1.5 mm/min loading rate. As it can be seen in Table 5.6, the SIF values obtained from DIC and LEFM $J-K$ relation are lower for 1.5 mm/min loading rate than the others. The results of the DIC and the LEFM $J-K$ relation are thought to be reflecting the experiments better. Because the displacement field obtained from ABAQUS is highly dependent on the mesh size, a finer mesh would probably give a better correlation. Also the built-in user material subroutine for NiTi does not reflect the material used exactly for the experiments and is an ideal model which causes inconsistencies with the experiments. So writing a UMAT that takes into account the rate effect and the material behavior might be useful to get better results. SIFs calculated using ASTM E399 show an increasing trend with increasing loading rate. But the ASTM E399 equation was proposed for the plane strain case and linearly elastic homogeneous materials. So the SIF values obtained from DIC are thought to be reflecting the fracture toughness of NiTi better. The ASTM E399 results were added to the table for comparison purposes because this method gives approximate results of the stress intensity factors.

Table 5.6. Comparison of K_Is.

	K_I (MPa$\sqrt{m}$)			
Method	$0.1\frac{mm}{min}$	$0.5\frac{mm}{min}$	$1.5\frac{mm}{min}$	$2\frac{mm}{min}$
ASTM E399	27.94	29.6	29.68	30.11
DIC Least-squares-fit	33.26	33.76	29.49	33.81
LEFM $J-K$ Relation	28.67	30.32	30.23	30.62
FE Least-squares-fit	34.43	35.69	36.14	36.68

After obtaining the unknown parameters K_I, K_{II}, T, A_1 and u_{0y}, the displacement contour plots were plotted using the least-square-fitting of ABAQUS displacement data to Equation 3.8. The numerical implementation of the parameters was done using the Matlab code used in the case of the fitting of the DIC data. The resulting displacement contour plots of both ABAQUS and Equation 3.8 are presented in Figures 5.10, 5.11, 5.12, 5.13 for loading rates of 0.1, 0.5, 1.5, 2 mm/min, respectively.

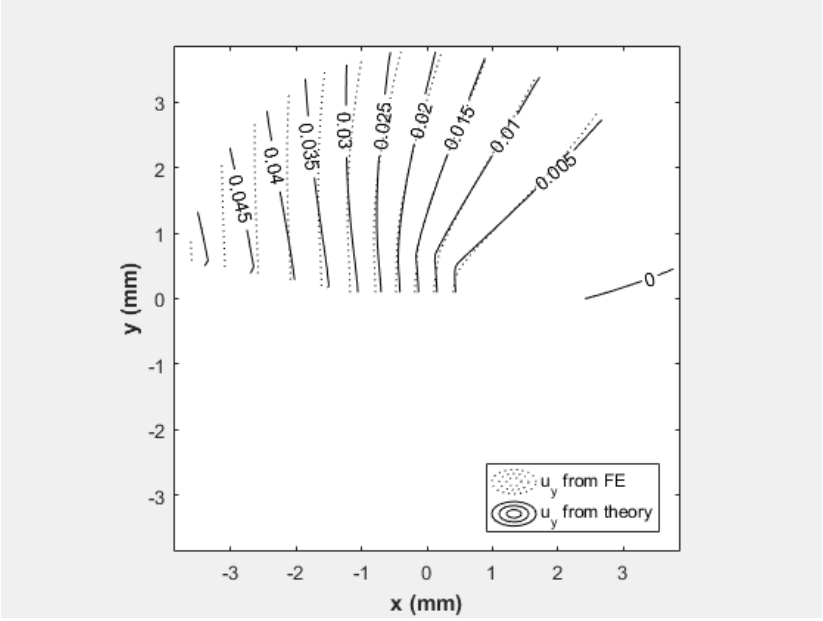


Figure 5.10. Displacement Contour Plots From ABAQUS and From Equation 3.8 For 0.1 mm/min Loading Rate.

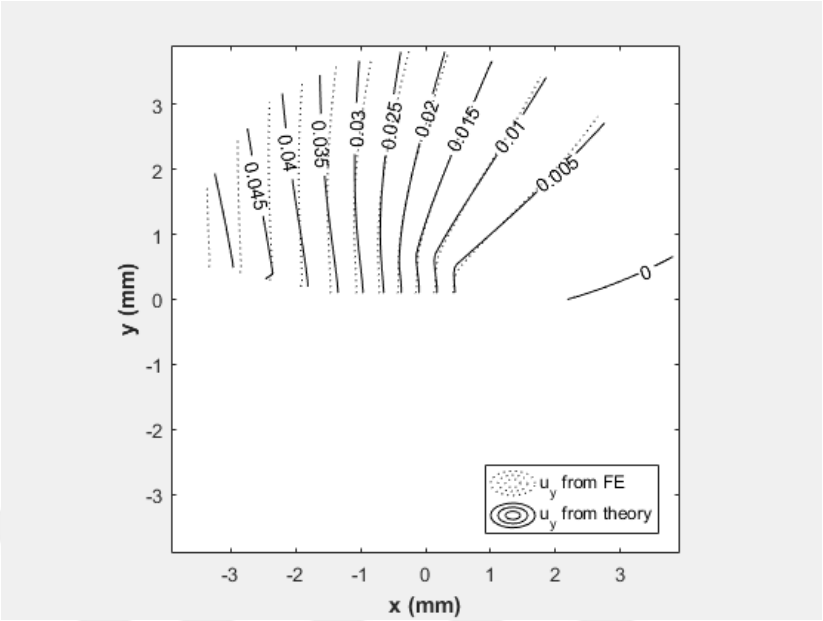


Figure 5.11. Displacement Contour Plots From ABAQUS and From Equation 3.8 For 0.5 mm/min Loading Rate.

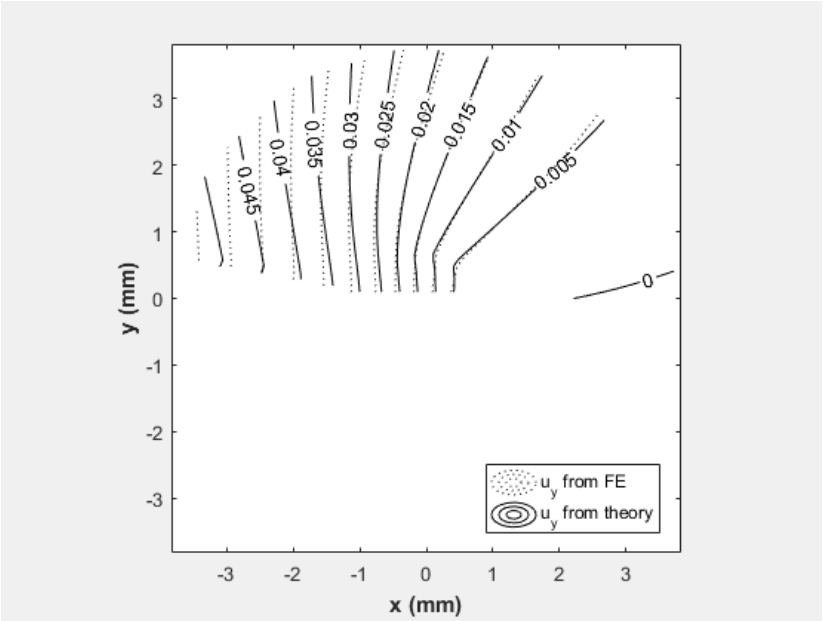


Figure 5.12. Displacement Contour Plots From ABAQUS and From Equation 3.8 For 1.5 mm/min Loading Rate.

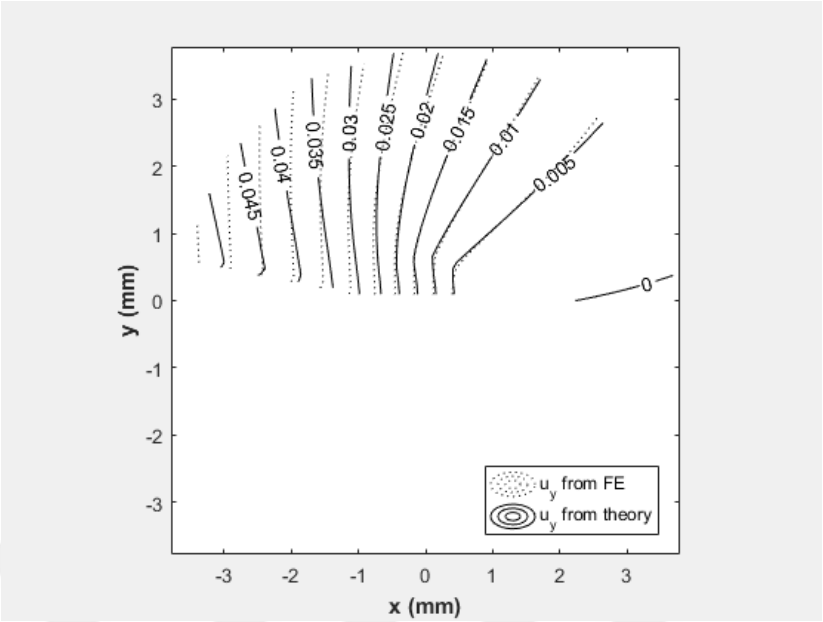


Figure 5.13. Displacement Contour Plots From ABAQUS and From Equation 3.8 For 2 mm/min Loading Rate.

The crack mouth opening displacement (CMOD) values were obtained from the FE models. CMOD values were measured from the knife edge of the CT specimen and the crack tip's vertical displacement from the initial state and the deformed state. The results are presented below in Table 5.7.

Table 5.7. Crack Mouth Opening Displacement (CMOD) obtained from the FE models of different loading rates.

Loading Rate	**CMOD (mm)**
0.1 mm/min	0.436
0.5 mm/min	0.4623
1.5 mm/min	0.4506
2 mm/min	0.4519

These results show that with increasing loading rates, the values of crack opening displacement increase. These results are in good agreement with the experimental

results that were tabulated in Table 3.1. These findings indicate that the fracture occurs later in higher loading rates than the slower ones. This is apparently related to the fully martensite transformation region size. It was found that with increasing loading rates the transformation zone sizes decrease and martensite phase is more brittle than the austenite phase. So it can be concluded that the larger the martensite phase the sooner the fracture occurs as a result of martensite's more brittle behavior. This time an inconsistency occurred with the loading rate case of 0.5 mm/min that the CMOD is larger than the other loading rate cases. This is thought to be due to a modeling error as mentioned before. A finer mesh and a UMAT subroutine that reflects the material property of the NiTi used would have probably given a better correlation with experimental results.

As mentioned before the built-in model used for the computational calculations is rate independent and does not take the temperature variation with transformation into account. Loading a NiTi cracked specimen results in martensitic transformation around the crack tip and due to this transformation a temperature increase occurs as a result of the thermomechanical coupling. Therefore the model used is needed to be a coupled model. For the computational calculations in this study, the material properties of the model were changed using the experimental results of the tensile tests. Although the results were in good agreement with the experimental results, this assumption can only give an idea on the results. Using the material properties obtained from tensile tests are not actually a good match to the solution of this coupled fracture problem. For accurate results a UMAT subroutine needs to be written that takes the thermomechanical coupling into account.

6. SUMMARY AND CONCLUSIONS

The main concern of this thesis was to investigate the effect of loading rate on fracture behavior of NiTi. For this purpose, at first DSC was performed to determine the phase transformation temperatures of NiTi. Determining the phase transformation stresses was critical, because an experiment conducted at a temperature below the A_f temperature could result in an improper measurement of material properties because the material may not be in austenitic phase at the beginning of the experiment. This subject is discussed in Section 2.2.3. Next, characterization of the material properties of NiTi was done through tensile tests using dog bone specimens. From the tensile tests, Young's moduli of martensite and austenite phases, then the forward (austenite to martensite) and reverse (martensite to austenite) phase transformation stresses and the upper plateau (UPS) and the lower plateau strengths (LPS) were obtained. The results of the experiments indicated that with increasing loading rate, the forward transformation stresses and the UPSs increase while the reverse transformation stresses and the LPSs decrease. For the last part of the material characterization, new tensile tests were conducted at different testing temperatures and transformation stresses were obtained. Using the transformation stresses and the temperature data, stress - temperature strips were plotted, and the Clausius - Clapeyron constants that govern the stress change at different temperatures were measured.

In Chapter 3, evaluation of fracture parameters for different loading rates were carried out using digital image correlation, DIC, which is an effective non contact method to obtain surface displacement fields of specimens tested. Compact tension (CT) specimens were painted on the surface with white matte spray paint and black speckles for displacement calculations with DIC. Images were captured during the test and the ones corresponding to maximum force were used to obtain the displacement field. The displacement data obtained from DIC were least-square fitted to the asymptotic near-tip opening displacement equation as proposed for example by Oral *et al.* [81], and stress intensity factor for Mode I, K_I and Mode II, K_{II}, T stress, rigid body displacement u_{0y} and rigid body rotation A_1 were calculated. For comparison

purposes, critical stress intensity factors were also calculated using LEFM following Equation 3.9, as defined by ASTM E399. The results were consistent with Jiang and Vecchio's study which has shown that stress intensity factors increase with increasing loading rate [70]. The critical stress intensity factors calculated using the equation defined by the ASTM E399 standard have an increasing trend, but one of the SIF values obtained from DIC data was inconsistent with the others; the value was found to be lower than the others. This inconsistency is thought to be a result of an experimental error because the other SIFs obtained show a distinct increase with increasing loading rate.

Following the tensile tests and fracture experiments, the phase transformation region around the crack tip was evaluated using DIC data and the analytical calculations using Equation 4.14 as proposed by Hazar *et al.* [71]. The transformation region was estimated using DIC with the equivalent strain contour maps obtained from the displacement field. The equivalent strain contours that correspond to martensitic transformation start and finish strains were plotted, and the region inside these contours were assumed to be the transformation zones. However, the transformation region that represents the fully martensitic zone could not be measured due to the limitations of the resolution. Analytical calculations supported the conclusion that the phase transformation region and the fully martensitic zone sizes decreases with increasing loading rate. However the inconsistency seen in the SIF calculation with DIC was also observed in the analytical transformation zone size calculations using K_I obtained from DIC, because Equation 4.14 has a strong dependency on the stress intensity factors.

In the last chapter, finite element analyses were performed using ABAQUS for further validation. In the model the exact dimensions and the material properties of the compact tension specimens were used to simulate fracture experiments. The resulting transformation region sizes were measured from the martensite volume fraction contours that correspond to $\zeta = 0$, and $\zeta = 1$, that are the boundaries of the phase transformation zone. Measured fully martensite regions are found to be smaller than the analytically calculated ones, and the problem encountered in the case of 1.5 mm/min loading rtae was observed here as well. The phase transformation zone sizes

were in good agreement with the experimental results, and they showed a decreasing trend with increasing loading rate. Finally, stress intensity factors were calculated using the J contour integral - stress intensity factor relation for the plane stress case. J contour integrals were obtained from the FEA and elasticity modulus of austenite were used for the calculations because the $J-$Integral value was taken from outside of the transformation region. Resulting stress intensity factors were found to be in good agreement with the experimental results even for the problematic loading case. This problem is thought to be an experimental error at the tensile test in which the material properties was obtained or at the fracture test that P_{max} was obtained. Aside from that, FEA results showed that the stress intensity factors increase with increasing loading rate.

Next, using the displacement field obtained from the FE models SIFs were calculated; they were found to be in good agreement with the previous calculations, and consistent with the claim that the stress intensity factors increase with increasing loading rates. There was not found any inconsistency with the results. The inconsistency found previously can be explained as follows: The SIF calculations were done using the displacement field obtained from ABAQUS which is highly dependent on the mesh. Initially FEA was performed with a coarser mesh that showed a dependence on the mesh size: the displacement field was obtained to be higher than the one obtained in the finer mesh case. So a finer mesh gives better SIF results when calculated from the displacement field when fit to Equation 3.8. The J contour integral that ABAQUS calculates characterizes the energy release rate associated with the crack. In this study the $J-$integral values were taken from outside the phase transformation zone where they were contour independent. The path independent $J-$integral does not depend on the mesh size [93]. Therefore, the SIF values calculated using the LEFM $J-K$ relation gives good agreement with the experimental results and was accepted to be the SIFs of the FEA.

Finally the Crack Mouth Opening Displacement (CMOD) values were obtained from the FE models. CMOD values were measured between the knife edge of the CT specimen and the crack tip's vertical displacement from the initial state and the

deformed state. The resulting CMOD values were consistent with the experimentally obtained CMOD measurements. But this time an inconsistency occurred with the 0.5 mm/min loading rate case because it has an unexpected value larger than the others. This inconsistency was thought to be a result of the mesh size. Still, except from this result, CMODs showed an increasing trend with increasing loading rates.

On the basis of the findings presented in this thesis, further studies are still required to validate the results. Due to the low resolution in DIC, the size of fully martensitic region could not be measured. For this purpose new experiments might be done using higher resolutions. Using a camera that can capture images with higher frequency, capturing the image that correspond to the exact time of fracture may be more accurate. Also, the full martensite region size can be captured. The temperature change as a result of phase transformation could not be measured with the thermal camera available. Accurate temperature distribution with a high speed camera could be measured and be used for calculations of the transformation stresses. Moreover, the effect of thermomechanical coupling that occurs as a result of the phase transformation could be modeled analytically and computationally to get a better validation of the experimental results.

REFERENCES

1. Lagoudas, D. C., *Shape memory alloys*, Springer, 2008.

2. Standard, A., "Standard Test Method for Transformation Temperature of Nickel-Titanium Alloys by Thermal Analysis", *ASTM Standard*, Vol. 5, pp. 1–4, 2004.

3. Maletta, C. and F. Furgiuele, *1D Phenomenological Modeling of Shape Memory and Pseudoelasticity in NiTi Alloys*, INTECH Open Access Publisher, 2012.

4. Falvo, A., F. Furgiuele, A. Leonardi and C. Maletta, "Stress-induced martensitic transformation in the crack tip region of a NiTi alloy", *Journal of materials engineering and performance*, Vol. 18, No. 5-6, pp. 679–685, 2009.

5. Tanaka, K., S. Kobayashi and Y. Sato, "Thermomechanics of transformation pseudoelasticity and shape memory effect in alloys", *International Journal of Plasticity*, Vol. 2, No. 1, pp. 59–72, 1986.

6. Anderson, T. L. and T. Anderson, *Fracture mechanics: fundamentals and applications*, CRC press, 2005.

7. Shafaghi, N., *Evaluation of fracture parameters of NiTi shape memory alloy using dijital image correlation*, Master's Thesis, Boğaziçi University, 2013.

8. Standard, A. *et al.*, "Standard Test Method for Linear-Elastic Plane-Strain Fracture Toughness KIc of Metallic Materials", *ASTM Standard*, 2012.

9. Abaqus, "UMAT and VUMAT routines for the simulation of Nitinol", *Abaqus Inc.*, Pawtucket, RI, 2008.

10. Ölander, A., "An electrochemical investigation of solid cadmium-gold alloys", *Journal of the American Chemical Society*, Vol. 54, No. 10, pp. 3819–3833, 1932.

11. Greninger, A. B. and V. G. Mooradian, "Strain transformation in metastable beta copper-zinc and beta copper-tin alloys", *American Institute of Mining and Metallurgical Engineers Technical Publication*, 1937.

12. Buehler, W. J., J. Gilfrich and R. Wiley, "Effect of low-temperature phase changes on the mechanical properties of alloys near composition TiNi", *Journal of applied physics*, Vol. 34, No. 5, pp. 1475–1477, 1963.

13. Stam, G. and E. van der Giessen, "Effect of reversible phase transformations on crack growth", *Mechanics of materials*, Vol. 21, No. 1, pp. 51–71, 1995.

14. Sun, Q., K. C. Hwang and S. Yu, "A micromechanics constitutive model of transformation plasticity with shear and dilatation effect", *Journal of the Mechanics and Physics of Solids*, Vol. 39, No. 4, pp. 507–524, 1991.

15. Birman, V., "On mode I fracture of shape memory alloy plates", *Smart materials and structures*, Vol. 7, No. 4, p. 433, 1998.

16. Tanaka, K. and Y. Sato, "Analysis of superplastic deformation during isothermal martensitic transformation", *Res Mech.*, Vol. 17, No. 3, pp. 241–252, 1986.

17. Yi, S. and S. Gao, "Fracture toughening mechanism of shape memory alloys due to martensite transformation", *International journal of solids and structures*, Vol. 37, No. 38, pp. 5315–5327, 2000.

18. Eshelby, J. D., "The determination of the elastic field of an ellipsoidal inclusion, and related problems", *Proceedings of the Royal Society of London A: Mathematical, Physical and Engineering Sciences*, Vol. 241, pp. 376–396, The Royal Society, 1957.

19. Sun, Q. P. and K. C. Hwang, "Micromechanics modelling for the constitutive behavior of polycrystalline shape memory alloys—I. Derivation of general relations", *Journal of the Mechanics and Physics of Solids*, Vol. 41, No. 1, pp. 1–17, 1993.

20. McKelvey, A. and R. Ritchie, "Fatigue-crack propagation in Nitinol, a shape-

memory and superelastic endovascular stent material", *Journal of Biomedical Materials Research*, Vol. 47, No. 3, pp. 301–308, 1999.

21. Yan, W., C. H. Wang, X. P. Zhang and Y.-W. Mai, "Effect of transformation volume contraction on the toughness of superelastic shape memory alloys", *Smart materials and structures*, Vol. 11, No. 6, p. 947, 2002.

22. McMeeking, R. and A. Evans, "Mechanics of Transformation-Toughening in Brittle Materials", *Journal of the American Ceramic Society*, Vol. 65, No. 5, pp. 242–246, 1982.

23. Hutchinson, J. W., "On steady quasi-static crack growth", *Harvard University Report DEAP S-8 (AFOSR-TR-74-1042)*, 1974.

24. Wang, G., "Effects of notch geometry on stress–strain distribution, martensite transformation and fracture behavior in shape memory alloy NiTi", *Materials Science and Engineering: A*, Vol. 434, No. 1, pp. 269–279, 2006.

25. Wang, X., B. Xu, Z. Yue and X. Tong, "Fracture behavior of the compact tension specimens in NiTi shape memory alloys", *Materials Science and Engineering: A*, Vol. 485, No. 1, pp. 14–19, 2008.

26. Daly, S., A. Miller, G. Ravichandran and K. Bhattacharya, "An experimental investigation of crack initiation in thin sheets of nitinol", *Acta Materialia*, Vol. 55, No. 18, pp. 6322–6330, 2007.

27. Robertson, S., A. Mehta, A. Pelton and R. Ritchie, "Evolution of crack-tip transformation zones in superelastic Nitinol subjected to in situ fatigue: A fracture mechanics and synchrotron X-ray microdiffraction analysis", *Acta Materialia*, Vol. 55, No. 18, pp. 6198–6207, 2007.

28. Gollerthan, S., D. Herberg, A. Baruj and G. Eggeler, "Compact tension testing of martensitic/pseudoplastic NiTi shape memory alloys", *Materials Science and*

Engineering: A, Vol. 481, pp. 156–159, 2008.

29. Freed, Y. and L. Banks-Sills, "Crack growth resistance of shape memory alloys by means of a cohesive zone model", *Journal of the Mechanics and Physics of Solids*, Vol. 55, No. 10, pp. 2157–2180, 2007.

30. Panoskaltsis, V., S. Bahuguna and D. Soldatos, "On the thermomechanical modeling of shape memory alloys", *International Journal of Non-Linear Mechanics*, Vol. 39, No. 5, pp. 709–722, 2004.

31. Lexcellent, C. and F. Thiebaud, "Determination of the phase transformation zone at a crack tip in a shape memory alloy exhibiting asymmetry between tension and compression", *Scripta Materialia*, Vol. 59, No. 3, pp. 321–323, 2008.

32. Raniecki, B. and C. Lexcellent, "Thermodynamics of isotropic pseudoelasticity in shape memory alloys", *European Journal of Mechanics-A/Solids*, Vol. 17, No. 2, pp. 185–205, 1998.

33. Maletta, C. and M. Young, "Stress-induced martensite in front of crack tips in NiTi shape memory alloys: modeling versus experiments", *Journal of materials engineering and performance*, Vol. 20, No. 4-5, pp. 597–604, 2011.

34. Maletta, C. and F. Furgiuele, "Analytical modeling of stress-induced martensitic transformation in the crack tip region of nickel–titanium alloys", *Acta Materialia*, Vol. 58, No. 1, pp. 92–101, 2010.

35. Gollerthan, S., M. Young, A. Baruj, J. Frenzel, W. W. Schmahl and G. Eggeler, "Fracture mechanics and microstructure in NiTi shape memory alloys", *Acta Materialia*, Vol. 57, No. 4, pp. 1015–1025, 2009.

36. Baxevanis, T. and D. Lagoudas, "A mode I fracture analysis of a center-cracked infinite shape memory alloy plate under plane stress", *International journal of fracture*, Vol. 175, No. 2, pp. 151–166, 2012.

37. Dugdale, D. S., "Yielding of steel sheets containing slits", *Journal of the Mechanics and Physics of Solids*, Vol. 8, No. 2, pp. 100–104, 1960.

38. Nemat-Nasser, S. and W.-G. Guo, "Superelastic and cyclic response of NiTi SMA at various strain rates and temperatures", *Mechanics of materials*, Vol. 38, No. 5, pp. 463–474, 2006.

39. Kim, K., *Effects of Crystallographic Texture and Applied Strain Rate on the Cyclic Behavior of Nickel-Titanium*, Ph.D. Thesis, University of Michigan, 2013.

40. Prahlad, H. and I. Chopra, "Development of a strain-rate dependent model for uniaxial loading of SMA wires", *Journal of Intelligent Material Systems and Structures*, Vol. 14, No. 7, pp. 429–442, 2003.

41. Brinson, L. C., "One-dimensional constitutive behavior of shape memory alloys: thermomechanical derivation with non-constant material functions and redefined martensite internal variable", *Journal of intelligent material systems and structures*, Vol. 4, No. 2, pp. 229–242, 1993.

42. Tobushi, H., Y. Shimeno, T. Hachisuka and K. Tanaka, "Influence of strain rate on superelastic properties of TiNi shape memory alloy", *Mechanics of Materials*, Vol. 30, No. 2, pp. 141–150, 1998.

43. Kim, S. and M. Cho, "A Strain Rate Effect of Ni–Ti Shape Memory Alloy Wire", *Japanese Journal of Applied Physics*, Vol. 49, No. 11R, p. 115801, 2010.

44. Pieczyska, E., S. Gadaj, W. Nowacki and H. Tobushi, "Phase-transformation fronts evolution for stress-and strain-controlled tension tests in TiNi shape memory alloy", *Experimental Mechanics*, Vol. 46, No. 4, pp. 531–542, 2006.

45. Kadkhodaei, M., R. Rajapakse, M. Mahzoon and M. Salimi, "Modeling of the cyclic thermomechanical response of SMA wires at different strain rates", *Smart Materials and Structures*, Vol. 16, No. 6, p. 2091, 2007.

46. Vitiello, A., G. Giorleo and R. E. Morace, "Analysis of thermomechanical behaviour of Nitinol wires with high strain rates", *Smart materials and structures*, Vol. 14, No. 1, p. 215, 2004.

47. Zhang, X., P. Feng, Y. He, T. Yu and Q. Sun, "Experimental study on rate dependence of macroscopic domain and stress hysteresis in NiTi shape memory alloy strips", *International Journal of Mechanical Sciences*, Vol. 52, No. 12, pp. 1660–1670, 2010.

48. Churchill, C., J. Shaw and M. Iadicola, "Tips and tricks for characterizing shape memory alloy wire: part 4–thermo-mechanical coupling", *Experimental Techniques*, Vol. 34, No. 2, pp. 63–80, 2010.

49. Roh, J.-H., "Thermomechanical Modeling of shape memory alloys with rate dependency on the pseudoelastic behavior", *Mathematical Problems in Engineering*, Vol. 2014, 2014.

50. Saletti, D., S. Pattofatto and H. Zhao, "Evolution of the martensitic transformation in shape memory alloys under high strain rates", *EPJ Web of Conferences*, Vol. 6, p. 29008, EDP Sciences, 2010.

51. Huang, H., D. Saletti, S. Pattofatto, F. Shi and H. Zhao, "Experimental observation of phase transformation front of SMA under impact loading", *ICF13*, 2013.

52. Imanol, F., Z. Javier, A. Laurentzi, C. Germán, A. Jon and U. Idoia, "Constitutive model taking into account the strain rate for uniaxial NiTi shape memory alloy under low velocity impact conditions", *Smart Materials and Structures*, Vol. 17, No. 6, p. 065033, 2008.

53. Auricchio, F., D. Fugazza and R. Desroches, "Rate-dependent thermo-mechanical modelling of superelastic shape-memory alloys for seismic applications", *Journal of Intelligent Material Systems and Structures*, Vol. 19, No. 1, pp. 47–61, 2008.

54. Zhu, S. and Y. Zhang, "A thermomechanical constitutive model for superelastic SMA wire with strain-rate dependence", *Smart Materials and Structures*, Vol. 16, No. 5, p. 1696, 2007.

55. Tanaka, K., "A thermomechanical sketch of shape memory effect: one-dimensional tensile behavior", *Res Mechanica*, 1986.

56. He, Y. and Q. Sun, "Frequency-dependent temperature evolution in NiTi shape memory alloy under cyclic loading", *Smart Materials and Structures*, Vol. 19, No. 11, p. 115014, 2010.

57. Yin, H., Y. He and Q. Sun, "Effect of deformation frequency on temperature and stress oscillations in cyclic phase transition of NiTi shape memory alloy", *Journal of the Mechanics and Physics of Solids*, Vol. 67, pp. 100–128, 2014.

58. Dolce, M. and D. Cardone, "Mechanical behaviour of shape memory alloys for seismic applications 2. Austenite NiTi wires subjected to tension", *International Journal of Mechanical Sciences*, Vol. 43, No. 11, pp. 2657–2677, 2001.

59. DesRoches, R., J. McCormick and M. Delemont, "Cyclic properties of superelastic shape memory alloy wires and bars", *Journal of Structural Engineering*, Vol. 130, No. 1, pp. 38–46, 2004.

60. Qiana, H., W. Ren, H. Chen, H. Guc and S. Zhang, "A 1D Rate-dependent Constitutive Model for Thermomechanical Behavior of Superelastic Shape Memory Alloys", *Proc. of SPIE Vol*, Vol. 7643, pp. 76430F–1, 2010.

61. Qian, H., H. Li, G. Song and W. Guo, "A constitutive model for superelastic shape memory alloys considering the influence of strain rate", *Mathematical Problems in Engineering*, Vol. 2013, 2013.

62. Araki, Y., N. Maekawa, T. Omori, Y. Sutou, R. Kainuma and K. Ishida, "Rate-dependent response of superelastic Cu–Al–Mn alloy rods to tensile cyclic loads",

Smart Materials and Structures, Vol. 21, No. 3, p. 032002, 2012.

63. Morin, C., Z. Moumni and W. Zaki, "A constitutive model for shape memory alloys accounting for thermomechanical coupling", *International Journal of Plasticity*, Vol. 27, No. 5, pp. 748–767, 2011.

64. Morin, C., Z. Moumni and W. Zaki, "Thermomechanical coupling in shape memory alloys under cyclic loadings: experimental analysis and constitutive modeling", *International Journal of Plasticity*, Vol. 27, No. 12, pp. 1959–1980, 2011.

65. Adharapurapu, R. R., F. Jiang, K. S. Vecchio and G. T. Gray, "Response of NiTi shape memory alloy at high strain rate: A systematic investigation of temperature effects on tension–compression asymmetry", *Acta Materialia*, Vol. 54, No. 17, pp. 4609–4620, 2006.

66. Nemat-Nasser, S. and J. Y. Choi, "Strain rate dependence of deformation mechanisms in a Ni–Ti–Cr shape-memory alloy", *Acta Materialia*, Vol. 53, No. 2, pp. 449–454, 2005.

67. Nemat-Nasser, S., J. Y. Choi, W.-G. Guo, J. B. Isaacs and M. Taya, "High strain-rate, small strain response of a NiTi shape-memory alloy", *Journal of engineering materials and technology*, Vol. 127, No. 1, pp. 83–89, 2005.

68. Nemat-Nasser, S., J.-Y. Choi, W.-G. Guo and J. B. Isaacs, "Very high strain-rate response of a NiTi shape-memory alloy", *Mechanics of materials*, Vol. 37, No. 2, pp. 287–298, 2005.

69. Ardakani, S. H., H. Ahmadian and S. Mohammadi, "Thermo-mechanically coupled fracture analysis of shape memory alloys using the extended finite element method", *Smart Materials and Structures*, Vol. 24, No. 4, p. 045031, 2015.

70. Jiang, F. and K. S. Vecchio, "Fracture of Nitinol under quasistatic and dynamic loading", *Metallurgical and Materials Transactions A*, Vol. 38, No. 12, pp. 2907–

2915, 2007.

71. Hazar, S., G. Anlas and Z. Moumni, "Evaluation of transformation region around crack tip in shape memory alloys", *International Journal of Fracture*, Vol. 197, No. 1, pp. 99–110, 2016.

72. Duerig, T. and K. Bhattacharya, "The influence of the R-phase on the superelastic behavior of NiTi", *Shape Memory and Superelasticity*, Vol. 1, No. 2, pp. 153–161, 2015.

73. Shaw, J. A. and S. Kyriakides, "Thermomechanical aspects of NiTi", *Journal of the Mechanics and Physics of Solids*, Vol. 43, No. 8, pp. 1243–1281, 1995.

74. Yang, S. and G. Dui, "Temperature analysis of one-dimensional NiTi shape memory alloys under different loading rates and boundary conditions", *International Journal of Solids and Structures*, Vol. 50, No. 20, pp. 3254–3265, 2013.

75. Koistinen, D. and R. Marburger, "A general equation prescribing the extent of the austenite-martensite transformation in pure iron-carbon alloys and plain carbon steels", *acta metallurgica*, Vol. 7, No. 1, pp. 59–60, 1959.

76. Wang, Z. and T. Inoue, "Analyses of temperature, structure and stress during quenching of steel with consideration for stress dependence of transformation kinetics", *J. Soc. Mater. Sci. Japan*, , No. 360, pp. 991–996, 1983.

77. Rice, J. and G. F. Rosengren, "Plane strain deformation near a crack tip in a power-law hardening material", *Journal of the Mechanics and Physics of Solids*, Vol. 16, No. 1, pp. 1–12, 1968.

78. Hazar, S., *Theoretical and numerical analysis of fracture of shape memory alloys*, Ph.D. Thesis, Boğaziçi University, 2014.

79. Williams, M., "On the stress distribtuion at the base of a stationary crack", *Journal Applied Mechanics*, Vol. 24, pp. 109–114, 1957.

80. Yi, S., S. Gao and L. Shen, "Fracture toughening mechanism of shape memory alloys under mixed-mode loading due to martensite transformation", *International journal of solids and structures*, Vol. 38, No. 24, pp. 4463–4476, 2001.

81. Oral, A., J. Lambros and G. Anlas, "Crack initiation in functionally graded materials under mixed mode loading: experiments and simulations", *Journal of Applied Mechanics*, Vol. 75, No. 5, p. 051110, 2008.

82. Student, R., R. Cintrón, R. Mentor and V. Saouma, "Strain measurements with the digital image correlation system Vic-2D", *System*, Vol. 106, p. 2D, 2008.

83. Sutton, M. A., J. J. Orteu and H. Schreier, *Image correlation for shape, motion and deformation measurements: basic concepts, theory and applications*, Springer Science and Business Media, 2009.

84. Daly, S. H., "Digital image correlation in experimental mechanics for aerospace materials and structures", *Encyclopedia of Aerospace Engineering*, 2010.

85. Haghgouyan, B., N. Shafaghi, C. C. Aydıner and G. Anlas, "Experimental and computational investigation of the effect of phase transformation on fracture parameters of an SMA", *Smart Materials and Structures*, Vol. 25, No. 7, p. 075010, 2016.

86. Saletti, D., S. Pattofatto and H. Zhao, "Measurement of phase transformation properties under moderate impact tensile loading in a NiTi alloy", *Mechanics of Materials*, Vol. 65, pp. 1–11, 2013.

87. Daly, S., G. Ravichandran and K. Bhattacharya, "Stress-induced martensitic phase transformation in thin sheets of Nitinol", *Acta Materialia*, Vol. 55, No. 10, pp. 3593–3600, 2007.

88. Maletta, C., "A novel fracture mechanics approach for shape memory alloys with trilinear stress-strain behavior", *International journal of fracture*, Vol. 177, No. 1,

pp. 39–51, 2012.

89. Maletta, C., E. Sgambitterra and F. Furgiuele, "Crack tip stress distribution and stress intensity factor in shape memory alloys", *Fatigue and Fracture of Engineering Materials and Structures*, Vol. 36, No. 9, pp. 903–912, 2013.

90. Xiong, F. and Y. Liu, "Effect of stress-induced martensitic transformation on the crack tip stress-intensity factor in Ni–Mn–Ga shape memory alloy", *Acta Materialia*, Vol. 55, No. 16, pp. 5621–5629, 2007.

91. Zaki, W. and Z. Moumni, "A three-dimensional model of the thermomechanical behavior of shape memory alloys", *Journal of the Mechanics and Physics of Solids*, Vol. 55, No. 11, pp. 2455–2490, 2007.

92. Şimşek, M., *Fracture mechanics analysis of shape memory alloys using finite elements*, Master's Thesis, Boğaziçi University, 2006.

93. Courtin, S., C. Gardin, G. Bezine and H. B. H. Hamouda, "Advantages of the J-integral approach for calculating stress intensity factors when using the commercial finite element software ABAQUS", *Engineering Fracture Mechanics*, Vol. 72, No. 14, pp. 2174–2185, 2005.